Title
Zombie Instability in Rotating, Stably-Stratified Shear Flows and in Protoplanetary Disks

Author
Pei, Suyang

Publication Date
2014

Peer reviewed|Thesis/dissertation

Zombie Instability in Rotating, Stably-Stratified Shear Flows and in Protoplanetary Disks

by

Suyang Pei

A dissertation submitted in partial satisfaction of the
requirements for the degree of
Doctor of Philosophy

in

Engineering – Mechanical Engineering

in the

Graduate Division

of the

University of California, Berkeley

Committee in charge:

Professor Philip S. Marcus, Chair
Professor Tarek I. Zohdi
Professor Mark T. Stacey

Spring 2014

Zombie Instability in Rotating, Stably-Stratified Shear Flows and in Protoplanetary Disks

Abstract

Zombie Instability in Rotating, Stably-Stratified Shear Flows and in Protoplanetary Disks

by

Suyang Pei

Doctor of Philosophy in Engineering – Mechanical Engineering

University of California, Berkeley

Professor Philip S. Marcus, Chair

One of the most important problems in astrophysics is how angular momentum is transported in protoplanetary disks (PPDs - disks containing gas and dust orbit around newly-forming protostars). Collisional viscosity is believed to be insufficient for angular momentum transport. Therefore, turbulence enhanced transport are proposed. In addition, long-lived coherent vortices are also speculated to exist in PPDs, which could play an important role in completing star formation and building planets. Without instabilities, turbulence and vortices cannot form. In weak magnetized PPDs, magneto-rotational instability (MRI) operates to generate turbulence. However, regions known as "dead zone", are cool and unionized to have MRI. This has led to intense theoretical and computational search for pure hydrodynamic instabilities.

A new hydrodynamic, finite amplitude instability has been discovered in linearly stable, rotating, stably-stratified, shear flows. The instability starts from a new family of critical layers - baroclinic critical layers. These critical layers, which are linear, neutrally stable eigenmodes in stratified shear flows, have singularity in their vertical velocities. Under the effect of rotation, these critical layers produce vortex layers. Vortex layers intensify by drawing energy from the background shear flows, and subsequently roll up to create new vortices, which in turn excite new critical layers. The process self-replicates until the whole domain is filled with large-volume, large amplitude vortices. Because this instability can occur in the dead zones of protoplanetary disks we refer it as zombie instability and these new class of vortices that self-replicate as zombie vortices. High resolution numerical simulations show this instability can be triggered by a variety of weak perturbations including small volume compact single vortex, a pair of vortices and noise. The threshold of the instability is determined by the Rossby number or vorticity of the initial perturbations. Energy analysis based on the zonal non-zonal decomposition of the energy shows energy that supplies the instability is extracted from the zonal flows. Vortex is responsible for the energy extraction process. Zombie instability saturates when all the space are taken by zombie vortices. The separation distance between zombie vortices is approximately the distance from critical layers with lowest stream-wise wave number to the perturbations. The flows at late time are

determined only by the background parameters not their initial perturbations. Zombie instability is also discussed in a broader picture to show the dead zones of PPDs are not dead. Our numerical simulation suggest although zombie instability is a finite-amplitude instability, due to the large Reynolds number of the disk flows, it is effectively a linear instability. How zombie instability might lead to sufficient angular momentum transport is also discussed. Finally, we speculate there might not be a laminar Keplerian disks at all. The disk flows are essentially turbulent from the collapsing of gas cloud, with one possibilities being turbulent flows filled with zombie vortices. A newly developed semi-analytic method for flows with strong background shear is introduced to be an alternative to widely used shearing sheet method in the astrophysical community. The semi-analytic method is used for simulating internal inertial-gravity waves in rotating, stratified flows with and without shear. The method can also be generalized to systems with linear forcing terms.

To my family

Contents

List of Figures

Acknowledgments

First and foremost, I would like to thank Philip Marcus, my Ph.D. advisor. Phil is very sharp in research and kind in life. His passion, energy and devotion always inspire me a lot. I learned a lot from him including Fluid Mechanics, Computation, Maths, Astrophysics and more importantly how to approach a complex problem. I also learned teaching and presentation skill from him. It is honor to have him as my Ph.D. advisor. Besides, I am truly appreciate his understanding, concerns and support for my family issue. I had a wonderful time at Berkeley in the Computational Fluid Dynamics (CFD) Lab working with Phil.

Much appreciation and special thanks go to Chung-Hsiang Jiang. Being a senior lab mate, I learned lots of computing skills from him. He always provides insightful comments and suggestions. Being a good friend, I enjoy exchanging opinions with him on different topics. He is very thoughtful and helps me a lot, especially during the time when I am not in Berkeley. Working with Chung-Hsiang made my Ph.D. more fruitful and joyful.

One of the motivations of the current research is from an open problem raised by Joe Barranco, who is a previous graduate student in our lab. I would like to thank him for his kind help for guiding me at the very beginning of my research and his suggestions and comments later on.

Pedram and I came to Phil's group at the same time. During the first years, we had several courses and learned spectral methods together as well as prepared our first DFD talk. He is always eager to help and share his opinions. I enjoy the time we worked together.

I would like to thank Caleb Levy for helping me run many simulations on NASA cluster before my account was reactivated. He was very patient and really help me a lot on my simulations.

I would like to thank friends that work together, Daniel Lecoanet, Meng Wang, Sa Huck, Mani Mahdinia, Aaron Wienkers ...

I would like to thank my thesis committee member: Prof. Tarek Zohdi and Prof. Mark Stacey for their time and support.

Finally, thanks to my parents, my parents in law, my lovely daughter and my wife for their emotional support.

Chapter 1

Introdution

One of the most important problems in astrophysics is how mass and angular momentum are transported in the protoplanetary disks (PPDs), which are disks containing gas and dust orbit around newly-forming protostars. Because PPDs are differentially rotating, viscous torquing could transport angular momentum. However, viscosity from molecular collisions appears to be inefficient. To model the structure and dynamics of the disks, Shakura and Sunyaev [Shakura and Sunyaev 1973] proposed a disk model including turbulence enhanced transport, and so introduced a turbulent or "eddy" viscosity, but left the source of the turbulence to be an open question.

3D coherent vortices are also speculated to play an important role in the late stage of star formations and earliest stages of plant formations in PPDs. In cool, neutral protoplanetary disks, vortices might transport angular momentum radially outward such that mass can continue accretion on to the protostars. Besides, anticyclonic vortices can accumulate dust and grains in their centers, which help form kilometer-size planetesimals, the building bloks to form planets [Barranco and Marcus 2005; 2000]. It has been observed atmosphere of the gas giants are filled with large long-lived vortices, most famous example being the Great Red Spot in Jovian atmosphere. The three important characteristics of the Jovian atmosphere are rotation, shear and stratification, which all exist in PPDs. Therefore, it is proposed PPDs also contain long-lived vortices [Adams and Watkins 1995; Barge and Sommeria 1995; Barranco and Marcus 2005; Tanga et al. 1996].

However, without instabilities, turbulence and long-lived coherent vortices cannot form. This has led to intense theoretical and computational studies. The Keplerian flows of the disks are linearly stable to infinitely small perturbations with respect to Rayleigh's criterion for centrifugal stability; i.e., the absolute value of angular momentum increases with increasing radius [Rayleigh, Lord 1916]. In weakly magnetized accretion disks, the magneto-rotational instability (MRI) [Balbus and Hawley 1991], first proposed by Velikhov [Velikhov 1959] and Chandrasekhar [Chandrasekhar 1960], is believed to be the source of turbulence generation and angular momentum transport in the non self-gravitating disks. The onset of MRI requires an negative radial gradient of angular velocity, which states Keplerian flows is always linearly unstable to MRI. The growth rate of its most unstable mode is order of the

orbital period. MRI turbulence could provide angular momentum transfer rate close to the theoretically requirement [King et al. 2007]. However, there exists relative cool and nearly neutral disk regions around protostars which lack sufficient ionization for the gas to couple to the magnetic fields. These regions are sandwiched by thin surface layers above and below, which have been ionized by cosmic rays or stellar radiation [Gammie 1996]. They are stable to MRI and therefore known as "dead zone". It is now generally accepted the existence of the dead zone theoretically [Bai and Goodman 2009; Turner, Carballido, et al. 2010; Turner and Drake 2009], and there has been increasingly interests in the dynamics within the dead zone [Armitage 2011]. However, Angular momentum must be transported through dead zone in order for protostars to complete their formation. There has been substantial efforts to search for purely hydrodynamic instabilities.

Because Keplerian flows have very high Reynolds number ($Re \sim 10^{13}$), it has been widely hoped the Keplerian flows are unstable to finite-amplitude perturbations [Dubrulle 1993; Dubrulle et al. 2005a; Hersant et al. 2005; D. Richard and Zahn 1999] by analogy with other *unstratified* linearly-stable shear flows, such as channel flow and pipe flow [Chagelishvili et al. 2003]. However, no self-sustained turbulences have been reported for Keplerian flows by numerical simulations [Balbus, Hawley, and Stone 1996; Hawley et al. 1999; Johnson and Gammie 2005b; Shen et al. 2006]. This could be due to the lack of resolution in simulations [Lesur and Longaretti 2005]. Experimental studies of *vertically unstratified* Taylor-Couette flows produce controversial measurements of angular momentum transport [Ji et al. 2006; Paoletti and Lathrop 2011; van Gils et al. 2011] and their results are still in debate [Balbus 2011; Paoletti, van Gils, et al. 2012; Schartman et al. 2012]. The disagreement in their results is mainly due to the presence of Ekman pumping from the top and bottom lid. To date, people tend to believe the unstratified Keplerian flows are also nonlinearly stable although there are no definite proofs of that.

The disks can be linearly unstable globally due to the Rossby wave instability (RWI) and produce large coherent vortices called Rossby vortices. RWI was first studied by Lovelace group in 2D disks both analytically and numerically [Li, Colgate, et al. 2001; Li, Finn, et al. 2000; Lovelace et al. 1999]. It can be seen as an equivalent of the Kelvin-Helmholtz instability in the context of a differentially rotating disk. Vortices form at the inflexion point of the flow, with Rossby waves and spiral density waves propagating outward. The criterion for this instability is an extremum in the generalized potential vorticity (vortensity) of the equilibrium flow. Certain quantities that has extremum such as surface density, pressure and density can trigger the instability. 3D hydrodynamic and resistive magnetohydrodynamical simulations of RWI are performed at the boundary of dead zone to study the structure and evolution of the Rossby vortices formed. [Lyra and Mac Low 2012; Meheut 2013; Meheut et al. 2010; 2008; Meheut, Meliani, et al. 2012; Meheut, Yu, et al. 2012; S. Richard and Barge 2013; S. Richard, Barge, and Le Dizès 2013]. Vortices formed in 3D have strong vertical convective rolls and do not migrate. It is expected that a density bump can be naturally generated at the boundaries of dead zone due to the different mass accretion rate on each side of its boundary, which triggers the RWI to form vortices on both side of dead zone boundary [Varnière and Tagger 2006]. To sustain vortices, the initial bump needs to

be continuously regenerated, which is likely unphysical.

Another instability that exists in unmagnetized non-barotropic disks creating large coherent vortices is baroclinic instability. It was first observed by [Klahr and Bodenheimer 2003] in the global simulations of disks with an outward decreasing entropy profile. Further investigations by [Klahr 2004; Petersen, Julien, et al. 2007; Petersen, Stewart, et al. 2007] using 2D global simulations and [Lesur and Papaloizou 2010] using both 2D and 3D local simulations confirmed it is a nonlinear (subcritical) instability supported by the baroclinic generation of vorticity that could occurred in disks with a linearly stable entropy gradient. The instability is also known as the subcritical baroclinic instability (SBI). It could be triggered by finite amplitude temperature or vorticity perturbations. However, SBI is very subtle. First, for it to operate, the thermal state of the background disk must be Schwarzschild unstable (convective instability criteria without shear), but Solberg-Hoïland stable (convective instability criteria with shear) to avoid linear instability to axisymmetric perturbations. Second, for SBI to be self-sustained a proper selected time scale for the thermal relaxation process is required. It can neither be too slow, which will make the flow around the vortex almost adiabatic therefore kills the baroclinic vorticity generation; nor too fast, which will reduce the effect of buoyancy. These two conditions together result in self-sustained vortices. Lyra and Klahr [Lyra and Klahr 2011] performed 3D fully-compressible magneto-hydrodynamic (MHD) simulations and found the baroclinic instability is important only when magnetic fields are too weakly coupled to the gas(i.e. in the dead zones). They do not survive when MRI is active. Recently, a detailed parameter study has been done for this instability [Raettig et al. 2013].

Turbulence could also be driven by convection. Radially convective instablity has been studied both linearly and nonlinearly with 2D simulations, showing slightly inward angular momentum transport [Johnson and Gammie 2005a; 2006]. In terms of vertical convection, while early 3D numerical simulations of convective instability have consistently yielded inward angular momentum transport[Cabot 1996; Stone and Balbus 1996]. Recent high-resolution incompressible simulations of disk convection show outward transport of angular momentum, that under reasonable disk conditions might yield a angular momentum transport that is not very small [Lesur and Ogilvie 2010]. It appears the early inward angular momentum transport is due to an invalid analytic approximation used. However, this convection transports heat vertically rather than angular momentum radially. Moreover, the mechanism to sustain the unstable stratification is missing in the simulations.

In recent studies, the importance of vertical stable stratification has been considered. It is an important characteristics in the disk flows yet was not considered in most previous studies. The reasons might be the following. First, PPDs are thin in vertical directions. In many studies, 2D models with surface density (density integration over vertical directions) are used. Second, the computational resource is limited to perform full 3D simulations at early times. Third, there might be a common belief that if flows with constant density fluid are stable, then vertical stable stratification should make them even more stable. However, this is not true. Vertical stratification, even it is stable, could bring new degrees of freedom to the systems that may lead new instabilities.[Barranco and Marcus 2005; Marcus, Pei,

et al. 2013; Tevzadze, Chagelishvili, and Zahn 2008]

An example of this is strato-rotational instability (SRI) [Molemaker et al. 2001; Yavneh et al. 2001]. It shows Couette-Taylor flows in a stratified fluid may become unstable even if the Rayleigh criterion for stability was satisfied, i.e., in the corresponding stable regime of constant density fluid flow. Moreover, the most unstable modes of this instability are non-axisymmetric, contrary to the classical Taylor vortices of the centrifugal instability. In the small gap limit, SRI is due to the resonance of boundary trapped modes. The theoretical analysis has then been continued in an astrophysical context [Shalybkov and Rüdiger 2005a; b] and extended to the stability of accretion disk Keplerian flows [Dubrulle et al. 2005b]. It has been confirmed by experimental analysis [Le Bars and Le Gal 2007]. However, since the unstable modes of the instability results from the resonance of boundary trapped modes, SRI needs the presence of close boundaries. When the gap width extends to infinity, SRI transforms into a radiative instability [Le Dizés and Billant 2009]. And it is found the decreasing stratification stabilizes the flows [Le Dizés and Riedinger 2010]. However, the most unstable modes are localized near the inner boundary. The boundary conditions required by these instabilities are not physical in unbounded disk flows.

The linear evolution of vertically stratified Keplerian flows has been studied extensively [Salhi and Cambon 2010; Salhi, Lehner, et al. 2013; Tevzadze, Chagelishvili, and Zahn 2008; Tevzadze, Chagelishvili, Zahn, et al. 2003; Volponi 2010]. The transient amplification of the leading vortex modes via shearing are studied, which can then generate spiral-density waves by linear mode coupling. However, they didn't provide any positive nonlinear feedback mechanism for the density spiral wave to regenerate the leading vortex modes. In addition, the fully nonlinear evolution of vertically stratified Keplerian shear flows were studied by several groups [Fleming and Stone 2003; Fromang and Papaloizou 2006; Oishi and Mac Low 2009]. These simulations include a magnetic filed with a large magnetic resistivity near the disk mid-plane to represent the dead zone region. It is found MRI is present far from the mid-plane and stable dead zone forms near the midplane.

Barranco and Marcus [Barranco and Marcus 2005] performed the first 3D simulation to study vortex dynamics and formations in a vertically stably-stratified disk with an isothermal background which corresponds to a linear Brunt-Väisälä frequency. Spectral method is used to obtain high spacial resolution. In the vertical direction, the size of the computational domain either extends to 4 pressure scale height or maps to infinity. They found vortices at the disk midplanes are not stable. More interestingly, new off-midplane vortices spontaneously formed. In one of their simulations, which the vertical domain was mapped to infinity and the Brunt-Väisälä frequency has a maximum due to gravity turning over to zero close to infinity, a third vortex was created in between the two formerly created off-midplane vortices. To understand the formation of the those off mid-plane vortices motivates the current research.

A new pure hydrodynamic, finite-amplitude instability has been discovered in linearly stable, rotating, stably-stratified, shear flows. The instability starts from a new family of critical layers, which we called baroclinic critical layers because it requires vertical stable stratification. These critical layers, which are linear, neutrally stable eigenmodes in stratified

shear flows, have singularity in their vertical velocities. Under the effect of rotation, these critical layers produce vortex layers. Vortex layers intensify by drawing energy from the background shear flows, and subsequently roll up to create new vortices, which in turn excite new critical layers. The process self-replicates until the whole domain is filled with large-volume, large amplitude vortices. High resolution numerical simulations show this instability can be triggered by a variety of weak perturbations. The threshold of the instability is determined by the Rossby number or vorticity of the initial perturbations. This instability is not subtle; it requires no special tuning or unphysical initial condition and boundary conditions. It is the cause of the formation of the off-midplane vortices [Barranco and Marcus 2005] mentioned above. Because this instability can occur in the dead zones of PPDs, we refer it as zombie instability and those large volume and Rossby number vortices that self-replicate as zombie vortices. In this dissertation, We discuss in details of zombie instability and its application in the dead zone by performing high resolution simulations of 3D rotating, stratified shear flows for either Boussinesq (salt water) or anelastic (ideal gas) fluid.

Chapter 2 discusses numerical methods used. In the numerical simulations with intense shear such as the flows in protoplanetary disks, the computation challenge comes from the advection by shear velocity terms, which constrain the maximum timestep allowed to use. To remove this constraint, two different methods are used in our simulations. One is the shear sheet method, which is commonly used in the astrophysical community to study the local property of the protoplanetary disk. The details of this method and its problems are briefly reviewed. We developed another method to evolve the problematic terms semi-analytically in time. The idea of the method is first illustrated by the 2D Euler equation with background shear. It is then generalized to 3D systems that describe salt water (Boussinesq equations) or ideal gas (anelastic equations) with rotation, stratification and sponge layers near boundaries. Unlike the shearing sheet method, the semi-analytic method doesn't introduce any artificial frequencies to the system. Therefore it is preferred in the simulations of the inertial-internal gravity waves under the effect of the background shear. Preliminary results of these waves are showed to verify the code.

Chapter 3, which partly appears in [Marcus, Pei, et al. 2013] and [Marcus, Jiang, et al. 2013], presents the details of zombie instability in rotating, vertically stably-stratified, shear flows with Boussinesq fluid. The finite-amplitude stability starts from a new class of linear neutrally stable eigenmodes in stratified shear flows, which we called baroclinic critical layer. These critical layers have singularity in vertical velocities and densities. Our high resolution numerical simulations show small localized perturbations can easily excite baroclinic critical layers, which produce vortex layers under the effect of rotation. Vortex layers growth by drawing energy from the background shear flow, and subsequently roll up and create new vortices. The new vortices then excite new critical layers, and the processes of critical layers excitation, vortex layer growth, roll-up and new vortices creation self-replicate until the whole computational domain are filled up with vortices. The instability is illustrated with initial perturbations in the form of a single compact vortex, a compact wave generator, a pair of vortex and random noise with Kolmogorov spectrum. It is showed the exponential

growth of the instability is due to the space filling of zombie vortices self-replication. Energy analysis based on the zonal non-zonal decomposition of kinetic energy shows energy that supplies the instability is extracted from the zonal flows. Vortex is responsible for the energy extraction process. Instability saturates when the all the space are taken by zombie vortices. The separation distance between zombie vortices is approximately the distance from critical layers with lowest stream-wise wave number to the perturbations. The flows at late time are determined only by the background parameters not their initial perturbations. This instability is expected to happen in the "dead zone" of a protoplanetary disk to fill it with large-amplitude zombie vortices. It may also be observable in the lab experiments of stratified Couette-Taylor flows. The reasons why this instability is not seen previously are discussed at the end.

Chapter 4 describes the zombie instability to the astrophysical community in a broader picture. Random noises with small Mach number are well-accepted as the proper initial conditions to perturbed the laminar Keplerian flows. Simulation results are presented with initial noises using the anelastic as well as fully-compressible equations for idea gas, which is more relevant to the "dead zone" of the protoplanetary disk. Comparison to a classical study of hydrodynamic instability of the disk reveals the importance of vertical stable stratification, which is ignored in most of the previous studies. The instability is proved by numerical simulations with both our spectral code and astrophysical ATHENA code [Gardiner and Stone 2008; Stone, Gardiner, et al. 2008]. The space filling factors of the zombie vortices are discussed. A scaling relation between Mach number and Rossby number is derived for the fully developed turbulence flow filled with zombie vortices. Based on the scaling we proposed for fully-compressible flows, zombie vortices have large amount of solenoidal component of kinetic energy as showed in our anelastic simulations. Due to the equi-partition of kinetic energy of the fully-compressible turbulence, the dilatational component of kinetic energy is also expect to be large, which contains acoustic waves. Acoustic waves have good correlations between density and velocities that could efficiently transfer angular momentum outward. The initial noises in the simulations are characterized by energy, the length of the inertial range and type of the spectrum. Noises with certain types of spectrum have its velocity and vorticity resides at different scales. This property is used to answer the importance question: what is the criteria for the instability. It is proved by numerical simulations, Rossby number of initial noises sets the threshold of the instability. By analogy of turbulent pipe flows, we are skeptical that there may not be a state of laminar disk at all. The disk flows are essentially turbulence from the last stage of cloud collapse. One possibility could be turbulent flows created by zombie instability.

Chapter 2

An Semi-analytic Method for Simulating Shearing, Rotating, Stratified Flows

2.1 Introduction

Motivated by studying vortex dynamics in flows of protoplanetary disks (gas flows around newly forming stars), whose characteristic features are rotation, vertical stratification and intense background shear, an 3D spectral code has been developed [Barranco and Marcus 2006]. Vortices within protoplanetary disks (PPDs) are most likely to be subsonic because for supersonic vortices, sound waves and shocks radiated would rapidly dissipate their kinetic energy leaving them to be subsonic. Anelastic approximation [P. R Bannon 1996], which filters out the acoustic modes, has been re-derived with a modification to include a background shear for flows within a isothermal PPD, i.e., a disk with constant background temperature [Barranco and Marcus 2006; Barranco, Marcus, and Umurhan 2000]. It is believed long-live coherent vortices and turbulence eddies have size smaller than a vertical pressure scale height. To obtain high resolution, simulations are performed in a local region of PPD (domain size is or order of vertical scale height) with spectral methods.

In the simulations, computational variables are expanded in Fourier series in the horizontal, i.e., stream-wise and cross-stream directions. The background shear velocity is unidirectional in the stream-wise direction and linearly depends on the cross-stream coordinate. This makes the equations non-autonomous in the cross-stream direction, therefore periodic boundary conditions cannot be directly applied in this direction. In addition, imposing background shear brings new computational challenge. Because of intense background shear, the advection by shear terms, if computed explicitly, could only adopt a very small timestep for time integration to avoid numerical instability due to large Courant number. To overcome these difficulties, a shearing sheet method is used by transforming the equations into quasi-Lagrangian coordinates that advect with the background shear [Barranco and Marcus

2006; Goldreich and Lynden-Bell 1965; Marcus and Press 1977; Rogallo 1981]. Shearing sheet methods are widely used in local simulations of PPDs. However, one problem of the shearing sheet method is the computational grid is sheared with the background flow and will become greatly distorted in time. Periodically, it is necessary to re-map the shearing coordinate system back onto the original undistorted grid (details in [Barranco and Marcus 2006]), which introduces an artificial temporal forcing. The forcing could cause parametric instability that creates unphysical waves and other flow features.

An alternative method is proposed to accurately study the inertial-internal gravity waves behavior under the effect of background shear. Instead of a linear shear, a periodicized "sawtooth" background shear is used together with a sponge layers close to the boundaries. This periodicized shear profile allows to impose periodic boundary conditions directly in cross-stream direction. To evolve flows with background shear, a semi-analytic method is developed to compute the advection by shear terms implicitly in the mixed Fourier and Physical space. This method could use comparable timestep as the shearing sheet method but will not introduce any artificial frequencies to the system. It is also generalized to include rotation and arbitrary form of vertical stratifications. In section 2, governing equations are written down; In section 3, semi-analytic method is constructed for the 2D Euler equations with background shear and then generalized to 3D Boussinesq equations with rotation, vertical stratification and background shear; In section 4, the developed semi-analytic method is tested and verified by various numerical simulations; Section 5 is conclusion.

2.2 Boussinesq Equations for Shearing, Rotating, Vertically Stratified Flows

The simplest model which involves all the important physics of flows in PPD is the rotating, vertically stratified plane Couette flow with Boussinesq fluid, which is considered the canonical test to study the PPD stability [Marcus, Pei, et al. 2013]. The flow rotates with an angular velocity $\Omega \equiv f/2$, where f is the Coriolis parameter. In a rotating frame about the vertical axis z, the equations of motion for total velocity $\boldsymbol{v}$ are:

$$\boldsymbol{\nabla} \cdot \boldsymbol{v} = 0, \tag{2.1}$$

$$\frac{\partial \boldsymbol{v}}{\partial t} = -(\boldsymbol{v} \cdot \boldsymbol{\nabla})\boldsymbol{v} - \frac{\boldsymbol{\nabla} p}{\rho_o} + \boldsymbol{v} \times f\hat{\boldsymbol{z}} - \frac{\rho - \rho_o}{\rho_o} g\hat{\boldsymbol{z}}, \tag{2.2}$$

$$\frac{\partial \rho}{\partial t} = -(\boldsymbol{v} \cdot \boldsymbol{\nabla})\rho, \tag{2.3}$$

where p is the pressure, ρ is the total density of the flow and ρ_o is a constant reference density. g is gravity, which is a constant. Coordinates with "hats" are unit vectors.

The flow has an unperturbed density $\bar{\rho}(z) = \rho_o(1 - \bar{N}^2 z/g)$, where $\bar{N} \equiv \sqrt{-g(\,\mathrm{d}\bar{\rho}/\,\mathrm{d}z)/\rho_o}$ is the unperturbed Brunt-Väisälä frequency, which is constant in the simplest case to involve

vertical stable stratification. The unperturbed velocity of plane Couette flow is $\bar{\boldsymbol{v}} = \bar{V}(y)\hat{\boldsymbol{x}}$, where $\bar{V}$ is the uni-directional shear velocity, and x, y are the stream-wise and cross-stream coordinates. The total velocity can be written as $\boldsymbol{v} = \bar{V}(y)\hat{\boldsymbol{x}} + \boldsymbol{v'}$, where $\boldsymbol{v'} = (v'_x, v'_y, v'_z)$ is the perturbed velocity to $\bar{V}(y)\hat{\boldsymbol{x}}$. Replacing $\boldsymbol{v}$ with $\bar{V}(y)$ and $\boldsymbol{v'}$, equations (2.1)–(2.3) can be re-written as:

$$\boldsymbol{\nabla} \cdot \boldsymbol{v'} = 0. \tag{2.4}$$

$$\frac{\partial \boldsymbol{v'}}{\partial t} = -\bar{V}\frac{\partial \boldsymbol{v'}}{\partial x} - (\boldsymbol{v'} \cdot \boldsymbol{\nabla})\boldsymbol{v'} - v'_y \frac{\mathrm{d}\bar{V}}{\mathrm{d}y}\hat{\boldsymbol{x}} - \frac{\boldsymbol{\nabla}\tilde{p}}{\rho_o} + \boldsymbol{v'} \times f\hat{\boldsymbol{z}} - \frac{\tilde{\rho}}{\rho_o} g\hat{\boldsymbol{z}}, \tag{2.5}$$

$$\frac{\partial \tilde{\rho}}{\partial t} = -\bar{V}\frac{\partial \tilde{\rho}}{\partial x} - (\boldsymbol{v'} \cdot \boldsymbol{\nabla})\tilde{\rho} + \rho_o \frac{\bar{N}^2}{g} v'_z, \tag{2.6}$$

where $\tilde{p}$ and $\tilde{\rho}$ are the pressure and density deviation from the unperturbed field.

The flows described here can have a shear velocity that is an arbitrary function in y. It is also not necessary for the gravity and Brunt-Väisälä frequencies to be constant, i.e., both are linear in the isothermal PPD. The semi-analytic method developed in following sections is general. It can be used for Boussinesq as well as anelastic equations with arbitrary $\bar{V}(y)$ and $\bar{N}(z)$.

2.3 Semi-analytic method with periodicized shear and sponge layers

The computational challenge comes from the advection by shear velocity terms which are the first terms in equations (2.5) & (2.6) in the form of $\bar{V}\frac{\partial}{\partial x}$. In the shearing sheet method, shear velocity is a linear function $\bar{V}(y) = -\sigma y$, with $\sigma = -3/2\Omega$ being the Keplerian shear. In semi-analytic method, it is replaced the with a periodicized "sawtooth" velocity that is periodic in y and almost everywhere equal to the true Keplerian velocity except near the turning point of the "sawtooth", which is close to the boundary of cross-stream direction. In the region near turning point, and only in that region, sponge layers in terms of boundary damping are introduced to prevent instability forming near the turning point of the shear velocity as well as remove the unphysical "reflection" of the outgoing waves back into the computational domain. The periodicized "sawtooth" shear and damping function are showed in Figure 2.1. The sawtooth velocity is the same as linear shear velocity in the interior region except near cross-stream boundary it turns over to zero to become periodic in y. The damping function $S(y)$ is 0 in the interior and gradually become -1 close the cross-stream boundaries. Therefore the damping is only effective near the cross-stream boundaries. Both the sawtooth shear and damping velocity are smoothed in the Fourier space by setting Fourier coefficients of the highest 1/3 wave numbers to be zero. We have tested the code by using many different cross-stream domain size L_y and found that the periodicity of $\bar{V}(y)$ and the

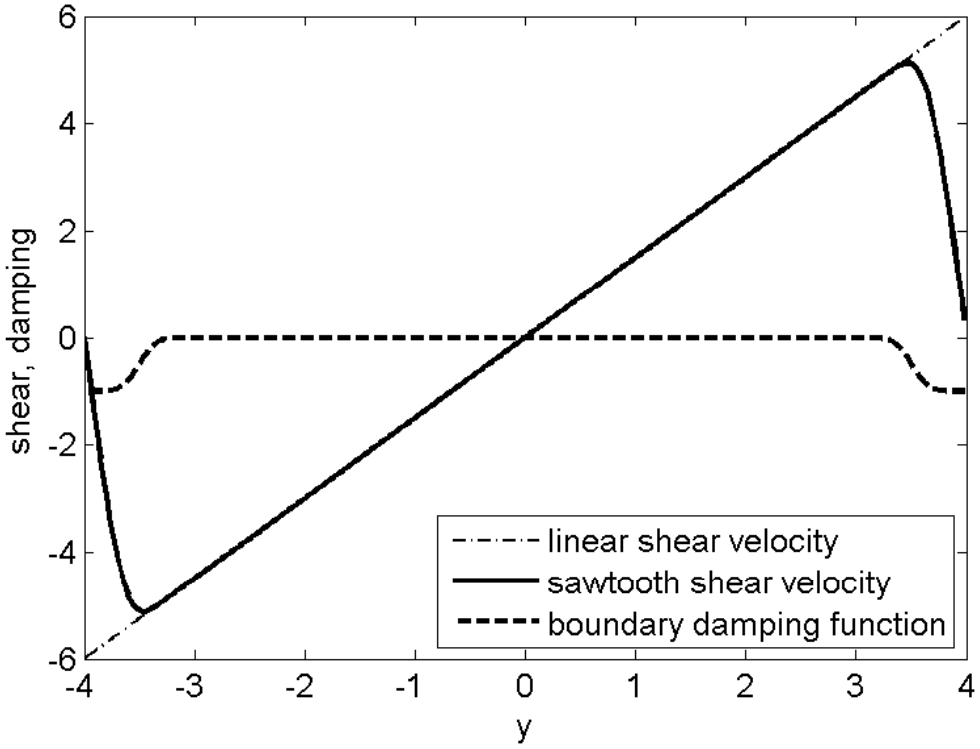

Figure 2.1: Periodicized sawtooth shear velocity and damping function in cross-stream direction. Dot dash line: linear shear velocity ($-\sigma y$, used in shearing sheet approximation); Solid line: periodicized shear velocity; Dash line: damping function.

damping near y boundary do not affect our results if L_y is sufficiently large. Semi-analytic methods ware used to treat rotation, stratification in previous studies [Barranco and Marcus 2006]. Here it is developed to evolve $\bar{V}\partial/\partial x$ terms implicitly in time and discussed in a more generalized way with details.

2D Euler System with Background Shear

To better illustrate the idea, we first consider the 2D Euler equations with periodicized background shear flow and damping near y boundaries

$$\boldsymbol{\nabla}\cdot\boldsymbol{v}=0, \tag{2.7}$$

$$\frac{\partial \boldsymbol{v}}{\partial t}=-\bar{V}(y)\frac{\partial \boldsymbol{v}}{\partial x}-\boldsymbol{v}\cdot\boldsymbol{\nabla}\boldsymbol{v}-v_y\frac{\mathrm{d}\bar{\boldsymbol{V}}}{\mathrm{d}y}-\boldsymbol{\nabla}p-S(y)\frac{\boldsymbol{v}}{\tau}, \tag{2.8}$$

where $\bar{\boldsymbol{V}}\equiv\bar{V}(y)\hat{\boldsymbol{x}}$ is the periodicized "sawtooth" shear. $S(y)$ is the damping function. τ is the damping time scale which is a constant. Note because we expand variables in stream-wise direction by Fourier series, we have $\partial/\partial x=\mathrm{i}k_x$ in the Fourier space, where $k_x\equiv 2\pi m/L_x$

is the stream-wise wave number, m being a positive integer. In Fourier space the nonlinear terms $\bar{V}(y)\partial/\partial x$ become linear. This motivates us to transform equation (2.8) to Fourier space in stream-wise direction

$$\frac{\partial \hat{\boldsymbol{v}}}{\partial t} = \xi \hat{\boldsymbol{v}} + \hat{\boldsymbol{a}} - \boldsymbol{\nabla}\hat{p}. \tag{2.9}$$

Variables with "hat" are in mixed space whose stream-wise direction is in Fourier space and cross-stream direction is in Physical space. $\hat{\boldsymbol{a}} \equiv -\widehat{\boldsymbol{v}\cdot\boldsymbol{\nabla}\boldsymbol{v}} - v_y\widehat{\frac{\mathrm{d}\bar{\boldsymbol{V}}}{\mathrm{d}y}}$ includes all the nonlinear terms. The coefficient in front of the linear terms is

$$\xi \equiv -\mathrm{i}k_x\bar{V}(y) + S(y)/\tau, \tag{2.10}$$

which is a function of y. Without loss of generality, the system of equation (2.9) can be described by a simple ordinary differential equation:

$$\frac{\mathrm{d}\phi}{\mathrm{d}t} = \xi\phi + r, \tag{2.11}$$

where r is the forcing constant. The exact solution for equation (2.11) is

$$\phi(t) = \mathrm{e}^{\xi t}\phi_0 + \frac{\mathrm{e}^{\xi t} - 1}{\xi} r. \tag{2.12}$$

equation (2.12) can be used as a template for deriving the semi-analytic scheme to evolve equation (2.9) in time numerically. Note the forcing term in equation (2.9) are not constant in time but corresponding to the nonlinear terms and pressure gradient terms. We treat the nonlinear terms with Adams-Bashforth scheme, the pressure gradient terms with Crank-Nicholson scheme to obtain a 2nd-order accurate scheme in time

$$\hat{\boldsymbol{v}}^{N+1} = \mathrm{e}^{\xi\Delta t}\hat{\boldsymbol{v}}^{N} + \frac{\mathrm{e}^{\xi\Delta t} - 1}{\xi}(\frac{3}{2}\hat{\boldsymbol{a}}^{N} - \frac{1}{2}\hat{\boldsymbol{a}}^{N-1}) - \frac{\mathrm{e}^{\xi\Delta t} - 1}{\xi}(\frac{1}{2}\boldsymbol{\nabla}\hat{p}^{N} + \frac{1}{2}\boldsymbol{\nabla}\hat{p}^{N+1}). \tag{2.13}$$

This is not the only choice. There are other semi-analytic schemes to evolve equation (2.9) in time. For instance, replacing $(\mathrm{e}^{\xi\Delta t} - 1)/\xi$ with $\mathrm{e}^{(\xi\Delta t/2)}\Delta t$ results in a new semi-analytic scheme which is also 2nd-order accurate in time

$$\hat{\boldsymbol{v}}^{N+1} = \mathrm{e}^{\xi\Delta t}\hat{\boldsymbol{v}}^{N} + \mathrm{e}^{\xi\frac{\Delta t}{2}}\Delta t(\frac{3}{2}\hat{\boldsymbol{a}}^{N} - \frac{1}{2}\hat{\boldsymbol{a}}^{N-1}) - \mathrm{e}^{\xi\frac{\Delta t}{2}}\Delta t(\frac{1}{2}\boldsymbol{\nabla}\hat{p}^{N} + \frac{1}{2}\boldsymbol{\nabla}\hat{p}^{N+1}). \tag{2.14}$$

However, since equation (2.13) is constructed based on the exact solution, it has the smallest truncation error. It can be showed analytically the truncation error of equation (2.13) is proportional to $\xi\frac{\Delta t^3}{6}$ while for equation (2.14) it is proportional to $\xi^2\frac{\Delta t^3}{6}$.

In practical, there are many other concerns when choosing numerical integration schemes. In above Euler system, in order to make velocities at time t^{N+1} satisfy the continuity equation (2.7), we need to take divergence on equation (2.13) to compute pressure at time t^{N+1} by solving a Poisson equation to obtain $\hat{p}^{N+1}$, and then update velocity to $\hat{\boldsymbol{v}}^{N+1}$. In the

case where ξ is a constant, $e^{(\xi\Delta t/2)}\Delta t$ can be taken out of the divergence operator, and the original Poisson operator remains. So the semi-analytic scheme in equation (2.13) works fine. However, in the case where the flow has a background shear, from equation (2.10), ξ will be a function of y, which makes the Poisson operator complicated. In addition, in next section we will generalize the semi-analytic scheme to three dimensional system. Brunt-Väisälä frequency and vertical boundary damping (necessary for a triply periodic code), which are generally functions of z, will be included. This makes the Poisson operator too complicated to solve the pressure with a fast solver. Instead, full matrix multiplication has to be used. This will slow down our simulations dramatically, which makes no sense to use semi-analytic scheme any more. Therefore, we want to modify the pressure gradient part in the semi-analytic scheme of equations (2.13) & (2.14) to avoid changing the Poisson operator but still keep it 2nd-order accurate in time.

We keep the coefficient in front of $\boldsymbol{\nabla}\hat{p}^{N+1}$ to be constant $\Delta t/2$ so that the Poisson operator is preserved, but modify the coefficient in front of $\boldsymbol{\nabla}\hat{p}^{N}$. To simplify notations, we define $\hat{\boldsymbol{\Pi}} \equiv \frac{\Delta t}{2}\boldsymbol{\nabla}\hat{p}$. Based on our numerical tests, we found the following scheme stable and allow us to use a comparable timestep as shearing sheet method

$$\hat{\boldsymbol{v}}^{N+1} = e^{\xi\Delta t}(\hat{\boldsymbol{v}}^{N} - \hat{\boldsymbol{\Pi}}^{N}) + \frac{e^{\xi\Delta t}-1}{\xi}(\frac{3}{2}\hat{\boldsymbol{a}}^{N} - \frac{1}{2}\hat{\boldsymbol{a}}^{N-1}) - \hat{\boldsymbol{\Pi}}^{N+1}, \tag{2.15}$$

where $\hat{\boldsymbol{\Pi}}^{N}$ and $\hat{\boldsymbol{v}}^{N}$ are combined together because they have the same coefficients. It can be proved this scheme is 2nd-order accurate in time. However, the price we paid to modified the pressure gradient term is now the truncation error of equation (2.15) becomes proportional to $\xi^2\frac{\Delta t^3}{6}$. We can also modified the scheme with equation (2.14) as

$$\hat{\boldsymbol{v}}^{N+1} = e^{\xi\Delta t}(\hat{\boldsymbol{v}}^{N} - \hat{\boldsymbol{\Pi}}^{N}) + e^{\xi\frac{\Delta t}{2}}\Delta t(\frac{3}{2}\hat{\boldsymbol{a}}^{N} - \frac{1}{2}\hat{\boldsymbol{a}}^{N-1}) - \hat{\boldsymbol{\Pi}}^{N+1}. \tag{2.16}$$

The truncation error of equation (2.16) is still $\propto \xi^2\frac{\Delta t^3}{6}$. Now, this scheme is comparable to scheme with equation (2.15) in terms of accuracy. This has been verified in Figure 2.2 for a generalized ξ in a three-dimensional problem.

In 2D Euler equations, the horizontal components of velocity do not couple. The simple system has two separate scalar equations that have the same one-dimensional eigenvalue ξ. The procedures to construct a semi-analytic scheme can be generalized to 3D problems with more physics involved such as rotation, stratification, viscosity and so on.

3D Boussinesq System with Rotation, Stratification and Background Shear

For a 3D system that describes flows in a PPD, we can reduce it to a similar system like equation (2.9) by solving an eigenvalue problem of the linear operator, from which the same procedures can be taken to construct the semi-analytic scheme. Here we take the Boussinesq flow system described by equations (2.5)–(2.6) as an example. Besides the background shear flow, the system also has constant rotation around vertical axis and stable density

stratification along the vertical direction. The horizontal components of velocity couple together by Coriolis force, resulting in inertial oscillation with the Coriolis frequency $\omega_f \equiv \sqrt{f(f - \mathrm{d}\bar{V}/\mathrm{d}y)}$, where $f \equiv 2\Omega$ is the Coriolis parameter with Ω being the constant angular velocity of the rotating system. Here the inertial frequency is modified by the background shear flow. The vertical component of velocity and density couple together by buoyancy force, resulting in buoyant oscillation with Brunt-Väisälä frequency $\bar{N}$. To be general we can make $\bar{N}$ an arbitrary real function of z. We also put sponge layers in forms of damping function $S(y)/\tau$ near y boundaries.

Boussinesq equations (2.5)–(2.6) can be written into a matrix form

$$\frac{\partial \hat{\boldsymbol{u}}}{\partial t} = \boldsymbol{L}\hat{\boldsymbol{u}} + \hat{\boldsymbol{q}} - \hat{\boldsymbol{p}}, \tag{2.17}$$

where

$$\hat{\boldsymbol{u}} = \begin{pmatrix} \hat{v'}_x \\ \hat{v'}_y \\ \hat{v'}_z \\ \hat{\tilde{\rho}} \end{pmatrix}, \qquad \hat{\boldsymbol{q}} = \begin{pmatrix} -\widehat{(\boldsymbol{v'}\cdot\boldsymbol{\nabla})v'_x} \\ -\widehat{(\boldsymbol{v'}\cdot\boldsymbol{\nabla})v'_y} \\ -\widehat{(\boldsymbol{v'}\cdot\boldsymbol{\nabla})v'_z} \\ -\widehat{(\boldsymbol{v'}\cdot\boldsymbol{\nabla})\tilde{\rho}} \end{pmatrix}, \qquad \hat{\boldsymbol{p}} = \begin{pmatrix} \partial\hat{\tilde{p}}/\partial x \\ \partial\hat{\tilde{p}}/\partial y \\ \partial\hat{\tilde{p}}/\partial z \\ 0 \end{pmatrix}, \tag{2.18}$$

$\boldsymbol{L}$ is the linear operator matrix,

$$\boldsymbol{L} = \begin{pmatrix} -\mathrm{i}k_x\bar{V} - S/\tau & f - \mathrm{d}\bar{V}/\mathrm{d}y & 0 & 0 \\ -f & -\mathrm{i}k_x\bar{V} - S/\tau & 0 & 0 \\ 0 & 0 & -\mathrm{i}k_x\bar{V} - S/\tau & -g \\ 0 & 0 & \bar{N}^2/g & -\mathrm{i}k_x\bar{V} - S/\tau \end{pmatrix}, \tag{2.19}$$

which is a block diagonal matrix because the Coriolis force couples the horizontal components of velocity and buoyancy force couples the vertical velocity and the density. It can be diagonalized as $\boldsymbol{L} = \boldsymbol{S}\boldsymbol{D}\boldsymbol{S}^{-1}$, $\boldsymbol{D}$ is the eigenvalue matrix

$$\boldsymbol{D} = \begin{pmatrix} -\mathrm{i}k_x\bar{V} - S/\tau + \mathrm{i}\omega_f & 0 & 0 & 0 \\ 0 & -\mathrm{i}k_x\bar{V} - S/\tau - \mathrm{i}\omega_f & 0 & 0 \\ 0 & 0 & -\mathrm{i}k_x\bar{V} - S/\tau + \mathrm{i}\bar{N} & 0 \\ 0 & 0 & 0 & -\mathrm{i}k_x\bar{V} - S/\tau - \mathrm{i}\bar{N} \end{pmatrix}, \tag{2.20}$$

$\boldsymbol{S}$ is the eigenvector matrix whose columns are the corresponding eigenvectors

$$\boldsymbol{S} = \begin{pmatrix} \sqrt{f - \mathrm{d}\bar{V}/\mathrm{d}y} & \sqrt{f - \mathrm{d}\bar{V}/\mathrm{d}y} & 0 & 0 \\ \mathrm{i}\sqrt{f} & -\mathrm{i}\sqrt{f} & 0 & 0 \\ 0 & 0 & \mathrm{i}g & -\mathrm{i}g \\ 0 & 0 & \bar{N} & \bar{N} \end{pmatrix}, \tag{2.21}$$

Left multiply equation (2.17) by $\boldsymbol{S}^{-1}$ resulting in

$$\frac{\partial \hat{\boldsymbol{w}}}{\partial t} = \boldsymbol{D}\hat{\boldsymbol{w}} + \hat{\boldsymbol{a}} - \hat{\boldsymbol{b}}, \tag{2.22}$$

where $\hat{\boldsymbol{w}} = \boldsymbol{S}^{-1}\hat{\boldsymbol{u}}$, $\hat{\boldsymbol{a}} = \boldsymbol{S}^{-1}\hat{\boldsymbol{p}}$, $\hat{\boldsymbol{b}} = \boldsymbol{S}^{-1}\hat{\boldsymbol{q}}$. Now the new system with equation (2.22) decoupled as four scalar equations for components of $\hat{\boldsymbol{w}}$. The problem reduces to the model problem described by equation (2.9). We construct the same semi-analytic scheme for time integration of $\hat{\boldsymbol{w}}$. Then we go back to the primary variables system by left multiplying $\boldsymbol{S}$ to the discretized system.

To make the scheme 2nd-order accurate, we treat nonlinear advection terms by Adams-Bashforth scheme

$$\hat{\boldsymbol{\mathcal{P}}} \equiv \frac{3}{2}(\widehat{\boldsymbol{v}\cdot\boldsymbol{\nabla}\boldsymbol{v}})^N - \frac{1}{2}(\widehat{\boldsymbol{v}\cdot\boldsymbol{\nabla}\boldsymbol{v}})^{N-1}, \tag{2.23}$$

$$\hat{\mathcal{Q}} \equiv \frac{3}{2}(\widehat{\boldsymbol{v}\cdot\boldsymbol{\nabla}\tilde{\rho}})^N - \frac{1}{2}(\widehat{\boldsymbol{v}\cdot\boldsymbol{\nabla}\tilde{\rho}})^{N-1}. \tag{2.24}$$

Define $\hat{\boldsymbol{\Pi}} \equiv \frac{\Delta t}{2}\boldsymbol{\nabla}\hat{p}$ as in previous section. The semi-analytic scheme written in primary variables is

$$\hat{v}_x^{N+1} = c_1(\hat{v}_x^N - \hat{\Pi}_x^N) + c_2\hat{\mathcal{P}}_x + c_3\alpha_1(\hat{v}_y^N - \hat{\Pi}_y^N) + c_4\alpha_1\hat{\mathcal{P}}_y - \hat{\Pi}_x^{N+1}, \tag{2.25}$$

$$\hat{v}_y^{N+1} = c_1(\hat{v}_y^N - \hat{\Pi}_y^N) + c_2\hat{\mathcal{P}}_y - c_3\alpha_2(\hat{v}_x^N - \hat{\Pi}_x^N) - c_4\alpha_2\hat{\mathcal{P}}_x - \hat{\Pi}_y^{N+1}, \tag{2.26}$$

$$\hat{v}_z^{N+1} = d_1(\hat{v}_z^N - \hat{\Pi}_z^N) + d_2\hat{\mathcal{P}}_z - d_3\beta_1\hat{\tilde{\rho}}^N - d_4\beta_1\hat{\mathcal{Q}} - \hat{\Pi}_z^{N+1}, \tag{2.27}$$

$$\hat{\tilde{\rho}}^{N+1} = d_1\hat{\tilde{\rho}}^N + d_2\hat{\mathcal{Q}} + d_3\beta_2(\hat{v}_z^N - \hat{\Pi}_z^N) + d_4\beta_2\hat{\mathcal{P}}_z, \tag{2.28}$$

where the coefficients are defined as

$$\lambda \equiv -\mathrm{i}k_x\bar{V} - S/\tau, \tag{2.29}$$

$$\alpha_1 \equiv f - \mathrm{d}\bar{V}/\,\mathrm{d}y, \qquad \alpha_2 \equiv f, \qquad \omega_f \equiv \sqrt{\alpha_1\alpha_2}, \tag{2.30}$$

$$c_1 \equiv \mathrm{e}^{\lambda\Delta t}\cos(\omega_f\Delta t), \tag{2.31}$$

$$c_2 \equiv \frac{1}{\lambda^2 + {\omega_f}^2}[\lambda(\mathrm{e}^{\lambda\Delta t}\cos(\omega_f\Delta t) - 1) + \omega_f\mathrm{e}^{\lambda\Delta t}\sin(\omega_f\Delta t)], \tag{2.32}$$

$$c_3 \equiv \mathrm{e}^{\lambda\Delta t}\frac{\sin(\omega_f\Delta t)}{\omega_f\Delta t}\Delta t, \tag{2.33}$$

$$c_4 \equiv \frac{1}{\lambda^2 + {\omega_f}^2}[\lambda\mathrm{e}^{\lambda\Delta t}\frac{\sin(\omega_f\Delta t)}{\omega_f\Delta t}\Delta t + 1 - \mathrm{e}^{\lambda\Delta t}\cos(\omega_f\Delta t)], \tag{2.34}$$

$$\beta_1 \equiv g, \qquad \beta_2 \equiv \frac{\bar{N}^2}{g}, \tag{2.35}$$

$$d_1 \equiv \mathrm{e}^{\lambda\Delta t}\cos(\bar{N}\Delta t), \tag{2.36}$$

$$d_2 \equiv \frac{1}{\lambda^2 + \bar{N}^2}[\lambda(\mathrm{e}^{\lambda\Delta t}\cos(\bar{N}\Delta t) - 1) + \bar{N}\mathrm{e}^{\lambda\Delta t}\sin(\bar{N}\Delta t)], \tag{2.37}$$

$$d_3 \equiv \mathrm{e}^{\lambda\Delta t}\frac{\sin(\bar{N}\Delta t)}{\bar{N}\Delta t}\Delta t, \tag{2.38}$$

$$d_4 \equiv \frac{1}{\lambda^2 + \bar{N}^2}[\lambda\mathrm{e}^{\lambda\Delta t}\frac{\sin(\bar{N}\Delta t)}{\bar{N}\Delta t}\Delta t + 1 - \mathrm{e}^{\lambda\Delta t}\cos(\bar{N}\Delta t)]. \tag{2.39}$$

This scheme is an analog to equation (2.15). We call it **scheme1**. The other scheme based on equation (2.16) has all the same coefficent defined as in **scheme1**, except

$$c_2 \equiv \mathrm{e}^{\lambda\frac{\Delta t}{2}}\cos(\omega_f\frac{\Delta t}{2})\Delta t, \tag{2.40}$$

$$c_4 \equiv \mathrm{e}^{\lambda\frac{\Delta t}{2}}\frac{\sin(\omega_f\frac{\Delta t}{2})}{\omega_f\frac{\Delta t}{2}}\frac{\Delta t^2}{2}, \tag{2.41}$$

$$d_2 \equiv \mathrm{e}^{\lambda\frac{\Delta t}{2}}\cos(\bar{N}\frac{\Delta t}{2})\Delta t, \tag{2.42}$$

$$d_4 \equiv \mathrm{e}^{\lambda\frac{\Delta t}{2}}\frac{\sin(\bar{N}\frac{\Delta t}{2})}{\bar{N}\frac{\Delta t}{2}}\frac{\Delta t^2}{2}. \tag{2.43}$$

and we refer this as **scheme2**

In **scheme1** the term $1/(\lambda^2+{\omega_f}^2)$ in equations (2.32) & (2.34) and the term $1/(\lambda^2+{\omega_{\bar{N}}}^2)$ in equations (2.37) & (2.39) become zero at cross-stream location $y*$, where $\bar{V}(y*) = \pm\frac{\omega_f}{k_x}$ and $\bar{V}(y*) = \pm\frac{\omega_{\bar{N}}}{k_x}$ respectively. In this case, we can go back to equation (2.15), it shows

$$\lim_{\xi\to 0}\frac{\mathrm{e}^{\xi\Delta t}-1}{\xi} \to \Delta t \tag{2.44}$$

This indicates the semi-analytic scheme reduces to Adams-Bashforth scheme at these locations. Similar schemes can be also derived for the anelastic equations. To solve equations (2.25)–(2.28), a fractional step method is used. In advection step, all the right-hand-side terms are computed except for $\hat{\mathbf{\Pi}}^{N+1}$ terms. In pressure step followed, Poisson equation is solved with a fast solver to get $\hat{\mathbf{\Pi}}^{N+1}$. Finally, all variables are updated to $N+1$ step. It is showed below both **scheme1** and **scheme2** are 2nd-order accurate in time. Details of the fast solver for Poisson equation refers to [Barranco and Marcus 2006].

2.4 Numerical Tests

It can be proved analytically both semi-analytic schemes are 2nd-order accurate in time. This is also seen in our numerical test shown in Figure 2.2. As indicated by analytic analysis, these two schemes should have errors at the same order of magnitude. This is shown in the plots that the errors of the two schemes almost lie on top of each other. In addition, both semi-analytic schemes have errors nearly an order of magnitude smaller than the explicit treatment of Coriolis and buoyancy terms.

A series of simulations has been done to test the parallel performance of the code, showed in Figure 2.3. In these simulations we use **scheme1** with 384 Fourier modes in the horizontal directions and 256 Chebyshev modes in the vertical direction, which are the typical number of modes used in our simulations of zombie instability. Power law (Time $\propto$ Nproc^{-p}) is used to fit the data to show how the total computing time scale with number of processors. $p \approx 1$

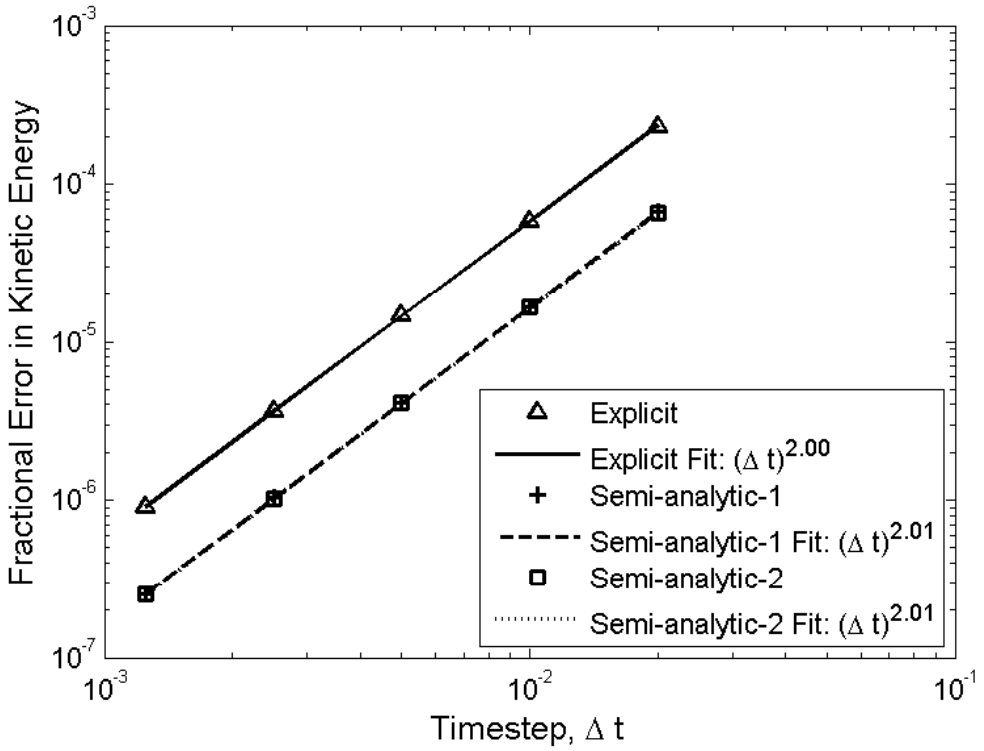

Figure 2.2: Fractional error in perturbation kinetic energy of different time evolution schemes for Boussinesq equations. Explicit: semi-analytic method only on the advection by shear part, Adams-Bashforth scheme on Coriolis and buoyancy terms. Semi-analytic-1: semi-analytic **scheme1**. Semi-analytic-2: semi-analytic **scheme2**. Solid line: power-law fit of the explicit scheme with exponent 2.00; dash line: power-law fit of semi-analytic **scheme-1** with exponent 2.01; dash line: power-law fit of semi-analytic **scheme-1** with exponent 2.01. (covered under dash line.)

is the ideal performance.The slope here is $p = 1.12$, showing good parallel performance of the code.

To compare semi-analytic method and shearing sheet method, we performed anelastic simulation of a single vortex initialized at the midplane in an isothermal PPD. The vortex will be unstable to an anti-symmetric eigenmode which exponentially grows from the roundoff errors [Barranco and Marcus 2005]. Once this mode becomes dominant, it can be easily seen by plotting the anti-symmetric part of the maximum absolute value of vertical vorticity, showed in Figure 2.4. The semi-analytic method is able to predict the same growth rate as the shearing sheet method, which corresponds to an e-folding time of 3.8 orbit period. The difference between this result and the one reported in [Barranco and Marcus 2006] is here we use a larger cross-stream domain size (4 times larger) to reduce the effects from periodic images in the cross-stream direction.

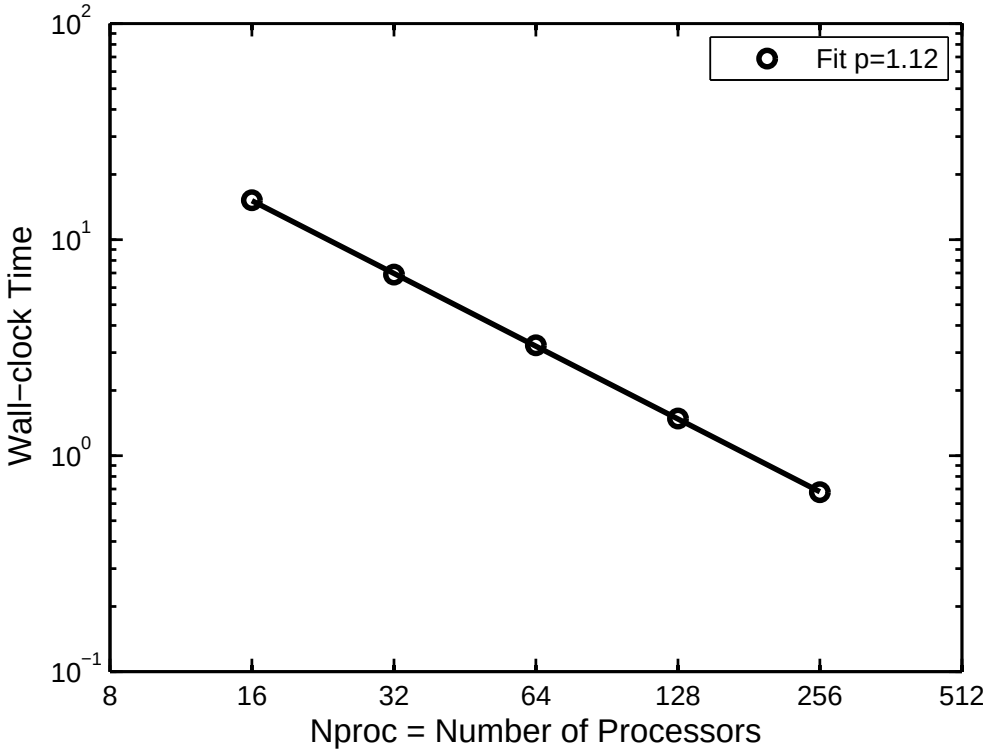

Figure 2.3: Wall-clock time to compute one timestep using 16, 32, 64, 128 and 256 processors on XSEDE cluster Stampede . The circle are the data points; the solid line are power-law fits; the number above is the best-fit exponent.

The semi-analytic method developed is good for simulating inertial-internal gravity waves without introducing artificial time scales. We test it by simulating these waves that are present in rating, stratified flows. To generate waves, we use a numerical wave generator, which is a spatially compact source oscillating in time imposed to the momentum equations (see Appendix).

Consider the waves in the flows without background shear, i.e., $\bar{V}(y) = 0$. Internal inertial-gravity waves are neutrally stable (neither grow nor decay) eigenmodes of the systems. They have dispersion relation:

$$s^2 = \bar{N}^2(\sin\theta)^2 + f^2(\cos\theta)^2, \tag{2.45}$$

where s is the eigenvalue (or frequency) of the mode, θ is the angle of the group velocity of the wave with respect to the horizontal plane. From equation (2.45), it shows waves can only exist when their frequencies satisfy the following solvability conditions of θ:

$$|f| < |s| < \bar{N} \qquad or \qquad \bar{N} < |s| < |f|, \tag{2.46}$$

where the left-side relation is for internal waves and the right-side relation is for inertial waves. Waves coming from a compact source (i.e., a wave generator) form wave packets or

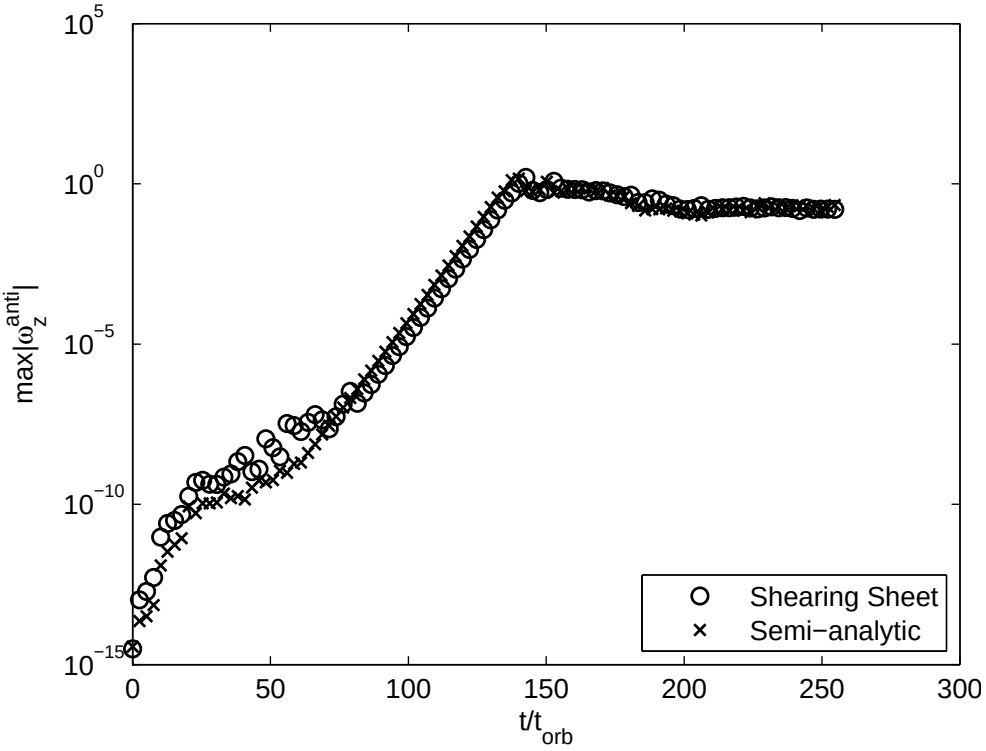

Figure 2.4: Comparison between shearing sheet method and semi-analytic method on the growth rate of anti-symmetric unstable linear eigenmode associated with a vortex initialized in an isothermal disk simulation. The unstable eigenmode is described by the maximum absolute value of the antisymmetric part of the vorticity associated with the vortex. Circle: shearing sheet method with cross-stream and vertical boundary damping. Cross: semi-analytic method with cross-stream and vertical boundary damping.

"beams" which consist multiple wavenumber components. The beams propagate with their group velocity emanating from the source. For a constant $\bar{N}$, those beams are straight and appear as a St Andrews cross pattern with its angle given by

$$(\tan\theta)^2 = (s^2 - f^2)/(N^2 - s^2), \tag{2.47}$$

where s is the forcing frequency of the wave source. In 3D, the beams have a conical shape. Figure 2.5 shows simulation results of internal gravity wave with $|f| < |s| < \bar{N}$ with $\bar{V}(y) = 0$. The numerical wave path matches the analytic one very well. Without using semi-analytic method, only 1/8 of the current timestep is allowed.

In an isothermal PPD, $\bar{N}$ is zero at disk midplane and linearly increases away from midplane. First, consider the linear stratified flow without background shear, i.e., $\bar{N} = \alpha z$ and $\bar{V}(y) = 0$. Under the condition that the length scale of the background stratification is much larger than the wave length (i.e., waves propagate in a slowly varying medium), locally

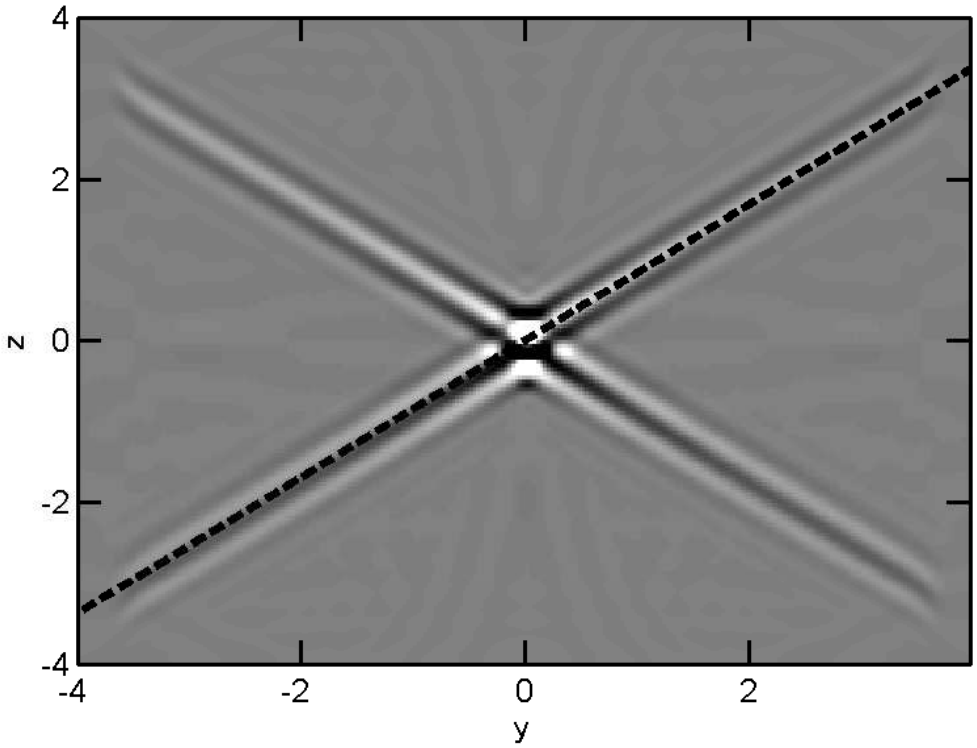

Figure 2.5: Numerical simulation of internal gravity wave in a non-shear flow with constant Brunt-Väisälä frequency. Contour plot: vertical vorticity ω_z in $y-z$ plane at $x = 0$, showing St Andrew's cross pattern. The colormap range is from -0.2 to 0.2, with black being negative (anticyclonic) vorticity and white being positive (cyclonic) vorticity. Black dash line: analytic solution of the wave path angle (only showing one branch). The background parameters of the simulation are $\bar{V}(y) = 0$, $f = 2\Omega$, $\bar{N} = 4\Omega$. The wave generator is placed at $(0, 0, 0)$ with a frequency $s = 3\Omega$ and magnitude $A = 3.75 \times 10^{-4}(\Omega^2 L_x)$.

we can treat $\bar{N}(z)$ as a constant by using the WKB theory. Therefore, the analytic wave path equation (2.47) can be modified as

$$(\tan\theta)^2 = (s^2 - f^2)/(N(z)^2 - s^2). \tag{2.48}$$

Instead of a straight line for constant $\bar{N}$, now the wave path becomes a curve. In addition, because of $\bar{N} = \alpha z$, if the forcing frequency of the wave generator has $|s| < |f|$, waves can only propagate in the region that satisfy $|s| > |\bar{N}(z)|$ according to equation (2.46). At the critical level where $|s| = |N(z)|$, waves cannot propagate any further and will reflect back. Figure 2.6 shows simulations of internal waves with $\bar{N} = (z/\sqrt{2.5})\Omega$, $\bar{V}(y) = 0$, $f = 2\Omega$. The wave generator locates at (0,0,-1) with a forcing frequency $s = 1.5\Omega$. The upper black dash line at $y = 0$ shows one branch of the internal wave propagates upward. When it reaches the critical level $N(z) = s$, it reflects and continue to propagate downward. The lower black dash

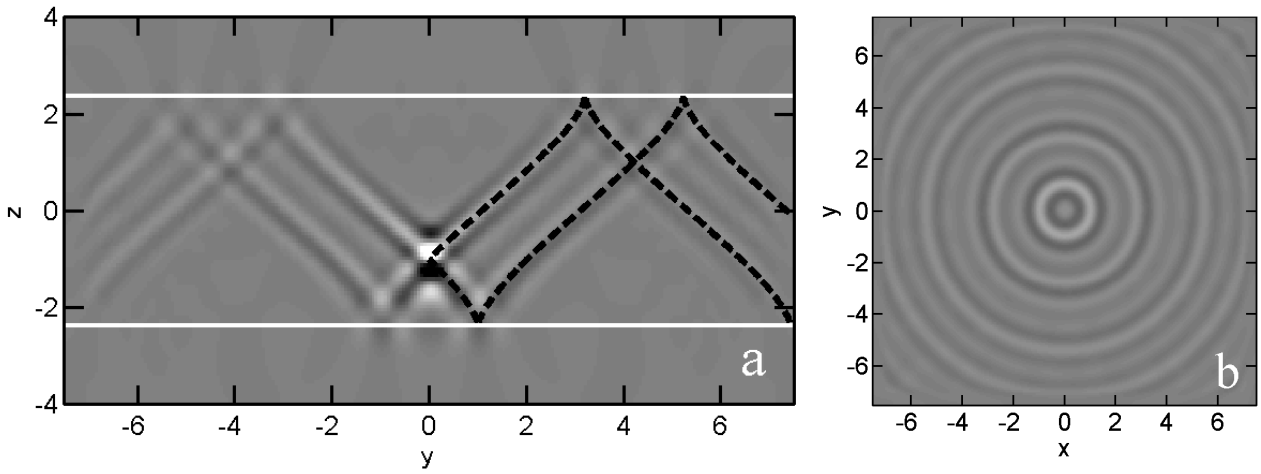

Figure 2.6: Numerical simulation of inertial gravity waves in a non-shear flow with linear Brunt-Väisälä frequency $\bar{N}(z) = \alpha z$. Contour plot: vertical vorticity ω_z in a) $y - z$ domain at $x = 0$; b) $x - y$ plane at $z = 0$. The colormap range is from -0.2 to 0.2, with black being negative (anticyclonic) vorticity and white being positive (cyclonic) vorticity. White solid line: the critical level where internal wave can not propagate and reflect back. The height corresponds to $\bar{N} = \pm s$. Black dash line: analytic solution of the wave path angle (only showing right branches). The background parameters of the simulation are $\bar{V}(y) = 0$, $f = 2\Omega$, $\bar{N} = (z/\sqrt{2.5})\Omega$. The wave generator locates at $(0, 0, -1)$, with a frequency $s = 1.5\Omega$ and magnitude $A = 9.375 \times 10^{-5}(\Omega^2 L_x)$. In x-y plane, the waves show concentric circles.

line at $y = 0$ shows another branch first propagates downward, then it reflects at the critical level $N(z) = -s$ and reverses its propagation direction. When it reaches the top critical height, it reflects again. The numerical results match well with the analytic angle. In $x - y$ plane at x=0, waves shows pattern of concentric circles. The most inner circle corresponds to the wave branches propagate upward from the wave generator, while the other circles are the reflected waves. In 3D they still have conical shapes.

Further, consider the inertial gravity waves in linear stratified flows with background shear, i.e., periodicized sawtooth shear as showed in Figure 2.1. With shear, the governing equations are no longer autonomous in y, except for $k_x = 0$ mode. Hence, analytic form of dispersion relation can only be obtained for waves with $k_x = 0$ mode:

$$s^2 = \bar{N}(z)^2(\sin\theta)^2 + f(f - \frac{\mathrm{d}\bar{V}}{\mathrm{d}y})(\cos\theta)^2, \tag{2.49}$$

where the Coriolis' frequency is modified by background shear. The propagation angle of $k_x = 0$ waves is:

$$(\tan\theta)^2 = [s^2 - f(f - \frac{\mathrm{d}\bar{V}}{\mathrm{d}y})]/(N(z)^2 - s^2). \tag{2.50}$$

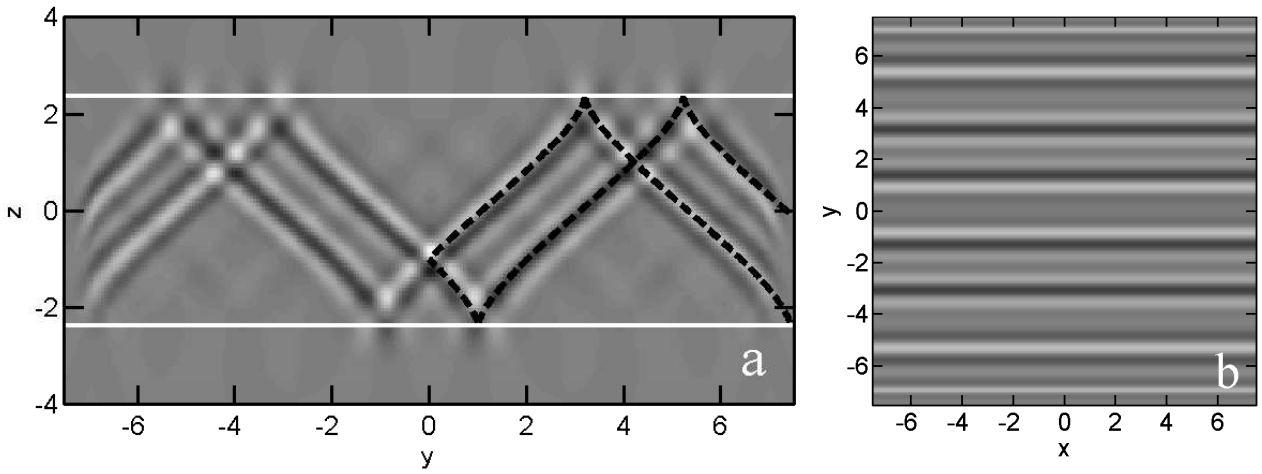

Figure 2.7: Numerical simulation of $k_x = 0$ inertial gravity waves in a shear flow with linear Brunt-Väisälä frequency $\bar{N}(z) = \alpha z$. Contour plot: vertical vorticity ω_z in a) $y - z$ domain at $x = 0$; b) $x - y$ plane at $z = 0$. The colormap range is from -0.2 to 0.2, with black being negative (anticyclonic) vorticity and white being positive (cyclonic) vorticity. White solid line: the critical level where internal wave can not propagate and reflect back. The height corresponds to $\bar{N} = \pm s$. Black dash line: analytic solution of the wave path angle (only showing right branches). The background parameters of the simulation are sawtooth type shear shown with its value of constant shear part being -3Ω, $f = 4\Omega$, $\bar{N} = (z/\sqrt{2.5})\Omega$. The wave generator only excites $k_x = 0$ waves. It is at $(0, 0, -1)$ with a frequency $s = 1.5\Omega$ and magnitude $A = 3.75 \times 10^{-4}(\Omega^2 L_x)$. In x-y plane, the waves are uniform in x direction showing $k_x = 0$ mode.

This is tested with numerical simulation shown in Figure 2.7. Unlike the previous simulations, which excites a range of wave numbers in each direction, here waves with a range of wave numbers in y and z but only $k_x = 0$ are excited. It can be seen in Figure 2.7b, the waves has uniform structure in x direction. In Figure 2.7a, it shows the same path as in Figure 2.6a. This is because $f(f - \mathrm{d}\bar{V}/\,\mathrm{d}y)$ in Figure 2.7 has the same value as f in Figure 2.6, therefore they have the same propagation angles. The numerical computed angles agree well with the analytic ones. The wave beams in Figure 2.7a contain multiple k_y and k_z modes but only a single $k_x = 0$ mode, while the wave beams in Figure 2.6a contain multiple k_x, k_y and k_z as shown in Figure 2.7b and Figure 2.6b.

2.5 Conclusion

The flows in the protoplanetary disks have three important features: rotation, vertical stable stratification and intense background shear. In numerical simulations of these flows, the advection by background shear terms constrain the maximum timestep allowed. In astrophysical community, shearing sheet method is commonly used to avoid computing these terms explicitly by transforming the equation to a Lagrange coordinate system advected with shear. To be numerically stable, shearing sheet method has to map the sheared grid back to the Cartesian grid, and so introduces a rezone time scale. This could cause parametric instability and other unphysical features, especially not good for simulations of internal inertial-gravity waves within the system.

A semi-analytic method is proposed. It evolves the advection by background shear terms semi-analytically in the mixed Fourier-Physical-Physical space. It can use a comparable timestep as the shearing sheet method. The method is first developed for a 2D Euler system with background shear, where the ideal scheme has been derived and modified by the practical concerns. It is then generalized to the 3D rotating, vertically stably-stratified Boussinesq flows with intense background shear by solving the eigenvalue problem of the linear operator. Periodicized sawtooth shear profile is used to directly impose the periodic boundary conditions in the cross-stream direction. The whole method is 2nd-order accurate in time and could use a comparable timestep as the shearing sheet method without introducing any artificial time scales to the system. Numerical tests show it works well in simulating internal inertial-gravity waves with or without background shear. It is also used in our anelastic simulations of PPD flows. Further, it can be generalized to any linear forcing terms.

Chapter 3

zombie instability and self-replicating zombie vortices in Stably Stratified Rotating Shear Flows

3.1 Introduction

For a protostar to accrete gas from its protoplanetary disk (PPD) and form a star, the PPD must be unstable and transport angular momentum outward [Balbus and Hawley 1998]. This has led to efforts to find instabilities in PPDs and other rotating flows that satisfy Rayleigh's criterion for centrifugal stability, i.e., the absolute value of angular momentum increases with increasing radius [Rayleigh, Lord 1916]. Numerical studies [Balbus, Hawley, and Stone 1996; Shen et al. 2006] of PPDs and experimental studies [Ji et al. 2006] of rotating flows where the velocity obeys Rayleigh's criterion confirm the stability of these flows (although there is recent controversy [Avila 2012; Paoletti, van Gils, et al. 2012; Schartman et al. 2012]). In a PPD where the gas is sufficiently ionized to couple to magnetic fields, the magneto-rotational instability (MRI) [Balbus and Hawley 1998] operates. However, large regions of PPDs, known as *d*ead zones, are too cool and un-ionized to have MRI. Other instabilities [Le Bars and Le Gal 2007; Lovelace et al. 1999] could de-stabilize a PPD, but they require unrealistic boundaries or continually-forced perturbations. Thus, star formation remains problematic.

Here we report a new type of finite-amplitude instability that occurs in neutrally-stable rotating flows that would also satisfy Rayleigh's stability criterion if their densities were constant (which was assumed in Rayleigh's analysis Rayleigh, Lord 1916). These flows include plane and circular Couette flows, which are used to model flows in PPDs. In this study, we examine rotating plane Couette flow, which is the canonical test for PPD stability. In previous studies using ideal gases [Balbus and Hawley 1998; Balbus, Hawley, and Stone 1996; Shen et al. 2006], these plane Couette flow PPD models were stable, but they were all initialized with no vertical density gradient and no vertical gravity g. In contrast, here

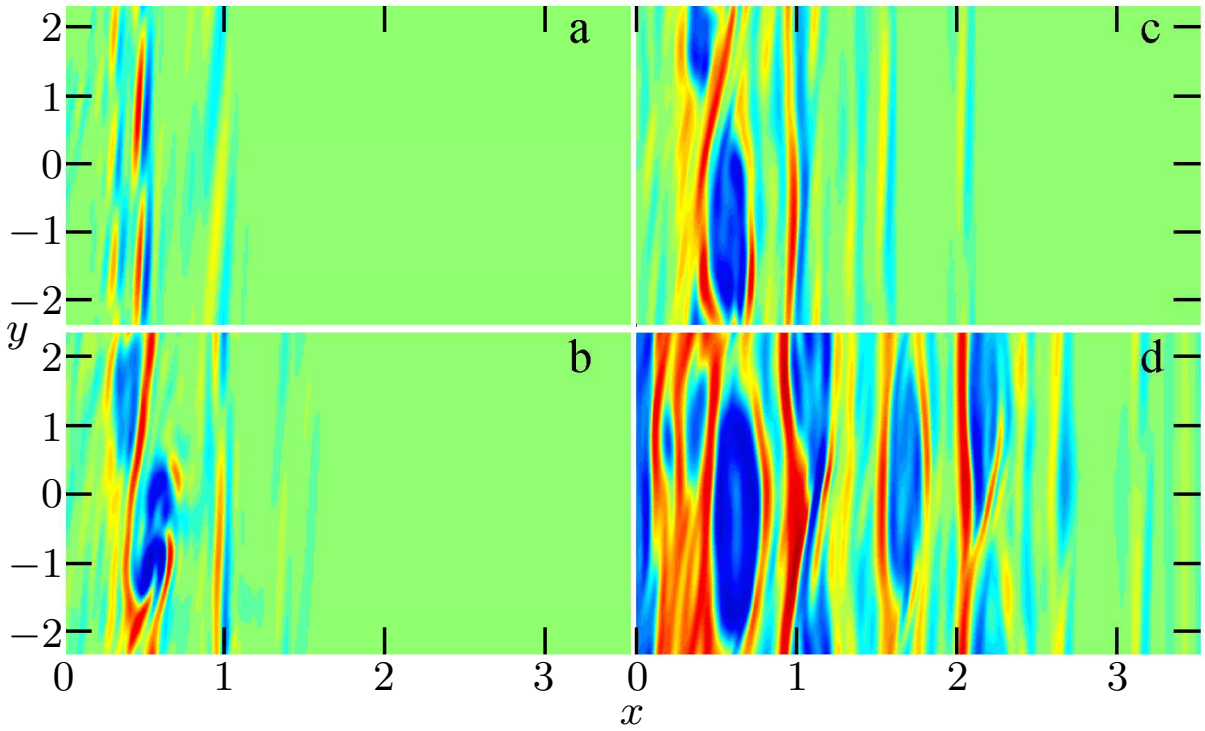

Figure 3.1: $Ro \equiv \omega_z/f$ of the anticyclonic (blue) vortices and cyclonic (red) vortex layers in the x-y plane. The initial perturbing vortex at the origin is above the plane shown here ($z = -0.404$). The first generation zombie vortices form at at $|x| \leq 1$, and sweep outward in x. The Rossby number Ro of these vortices is $\sim$ -0.2. (The color is reddest at $\omega_z/f = 0.2$, e.g., near $x = 1/3$ at the bottom of panel d; bluest at $\omega_z/f = -0.2$, e.g., near $x = 0.6$ in panel d; and green at $\omega_z/f = 0$). $f/\bar{N} = 1$ and $\sigma/f = -3/4$. The x-y domain is $|x| \leq 4.7124$; $|y| \leq 2.3562$, and is larger than shown. a) $t = 64/\bar{N}$. b) $t = 256/\bar{N}$. c) $t = 576/\bar{N}$. d) $t = 2240/\bar{N}$.

we include a stably-stratified initial density ρ with $g \neq 0$ (as in a PPD). Previously, we observed, but did not understand, a new finite-amplitude instability in a PPD with an ideal gas and $g \neq 0$ [Barranco and Marcus 2005; Marcus, Jiang, et al. 2013], so to simplify the analysis, here we consider a Boussinesq fluid with constant g. The 3D vortices found here are unique: a vortex that grows from a single, small-volume, initial perturbation triggers a 1^{st}-generation of vortices nearby. This 1^{st}-generation of vortices grows and triggers a 2^{nd}-generation. The triggering of subsequent generations continues *a*d infinitum. The vortices do not advect in the cross-stream direction, but the front dividing the vortex-populated fluid from the unperturbed fluid does. (Figure 3.1 and Figure 3.2) Because the vortices grow large and spawn new generations that march across the domain of a *d*ead zone, we refer to vortices that *s*elf-replicate to fill the domain as *z*ombie vortices.

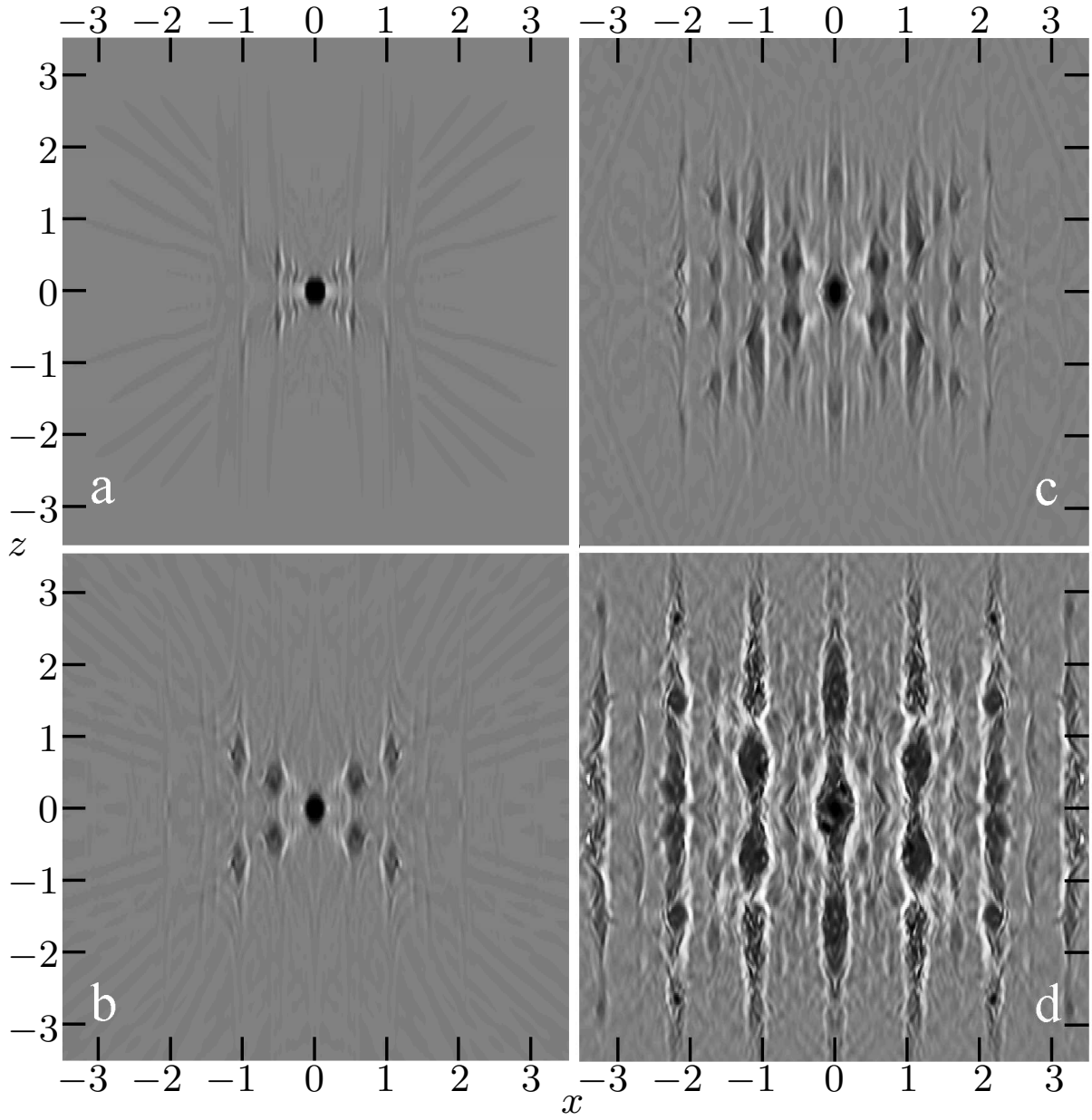

Figure 3.2: Zombie vortices sweep outward from the perturbing vortex at the origin in the x–z plane (at $y = 0$). Anticyclonic ω_z is black (darkest is $\omega/f = -0.2$) and cyclonic is white (lightest is $\omega/f = 0.2$). This is the same flow as in Fig. 1. The domain has $|x| \leq 4.7124$; $|z| \leq 4.7124$, and is larger than shown. a) $t = 128/\bar{N}$. Critical layers with $s = 0$ and $|m| = 1$, 2, and 3 are visible. Diagonal lines are $k_y = 0$ internal inertia-gravity waves with shear, not critical layers. b) $t = 480/\bar{N}$. 1^{st}-generation vortices near $|x| = 1$ and 1/2 have rolled-up from critical layers with $s = 0$ and $|m| = 1$ and 2, respectively. c) $t = 1632/\bar{N}$. 2^{nd}-generation $|m| = 1$ vortices near $|x| = 0$ and 2 were spawned from the 1^{st} generation vortices near $|x| = 1$. Another 2^{nd}-generation of $|m| = 1$ vortices is near $|x| \simeq 1/2$ and 3/2, which were spawned by the 1^{st} generation near $|x| = 1/2$. d) $t = 3072/\bar{N}$. 1^{st}, 2^{nd} and 3^{rd} generation vortices.

The simplest flow that is linearly stable, in which zombie vortices occur is a vertically stably-stratified Boussinesq fluid in an unbounded plane Couette flow. The unperturbed velocity of plane Couette flow observed in a frame with angular velocity $\Omega\hat{\mathbf{z}} \equiv f/2\hat{\mathbf{z}}$ is

$$\bar{\mathbf{v}} = \bar{V}(x)\hat{\mathbf{y}}, \tag{3.1}$$

with

$$\bar{V}(x) \equiv \sigma x, \tag{3.2}$$

where σ is the uniform shear, and x and y are the cross-stream and stream-wise coordinates. "Hatted" quantities are unit vectors. The unperturbed density is

$$\bar{\rho}(z) = \rho_0(1 - \bar{N}^2 z/g), \tag{3.3}$$

where ρ_0 is constant.

$$\bar{N} \equiv \sqrt{-g(d\bar{\rho}/dz)/\rho_0}, \tag{3.4}$$

is the initial unperturbed Brunt-Väisälä frequency. In the rotating frame, the governing equations are

$$\begin{aligned}
\nabla \cdot \mathbf{v} &= 0, && (3.5)\\
\partial \mathbf{v}/\partial t &= -(\mathbf{v}\cdot\nabla)\mathbf{v} - \frac{\nabla \Pi}{\rho_0} + f\mathbf{v}\times\hat{\mathbf{z}} - \frac{(\rho-\rho_0)g}{\rho_0}\hat{\mathbf{z}} && (3.6)\\
\partial \rho/\partial t &= -(\mathbf{v}\cdot\nabla)\rho. && (3.7)\\
& && (3.8)
\end{aligned}$$

where Π is the pressure head.

3.2 Critical Layers

When equations (3.5)–(3.7)) are linearized about $\bar{V}(x)$ and $\bar{\rho}(z)$, the eigenmodes are proportional to $e^{i(k_y y + k_z z - st)}$. When the initial density $\bar{\rho}$ is stably-stratified or constant plane Couette flow is neutrally linearly stable (i.e., s is real, and eigenmodes neither grow nor decay).

The eigen-equation for the eigenmodes of equations (3.5)–(3.7) is a generalization of Rayleigh's equation [Drazin and Reid 1981a] and is a 2^{nd}-order o.d.e. The coefficient of the highest-derivative term is

$$[\bar{V}(x) - s/k_y]\{[\bar{V}(x) - s/k_y]^2 - (\bar{N}/k_y)^2\}. \tag{3.9}$$

It is well known that the eigenmodes of an o.d.e. are singular at locations x^* where the coefficient of the highest-derivative term of the eigen-equation becomes zero. At x^*, the eigenmodes form *c*ritical layers [Drazin and Reid 1981a].

For fluids with constant density ($N \equiv 0$), critical layers have $\bar{V}(x^*)$ equal to the phase speed s/k_y of the eigenmode. We refer to these as *b*arotropic critical layers. These are the classical critical layers and have been well-studied [Maslowe 1986]. Eigenmodes with barotropic critical layers have singularities in the stream-wise components of their velocities, but not their other components.

For $\bar{N} \neq 0$, equation (3.9) shows that there are eigenmodes with barotropic critical layers, but they are not of interest to us because our computations show that they are difficult to excite and never form vortices. However, there is another class of eigenmodes with critical layers; they have

$$\bar{V}(x^*) - s/k_y \pm \bar{N}/k_y = 0, \tag{3.10}$$

and we call them *b*aroclinic critical layers. Weak baroclinic critical layers were shown to exist in non-rotating, stratified flows [Boulanger et al. 2007], but we believe that this is the first study of these layers in flows with f, N and $|\sigma|$ of the same order (as near the mid-plane of a PPD). From this point on, we use non-dimensional units with the units of time $1/\bar{N}$ and length $|(L\bar{N})/(2\pi\sigma)|$, where L is the periodicity length in y. Thus, k_y in equation (3.10) is $2\pi m/L$, where m is an integer. Baroclinic critical layers have $k_y \neq 0$, and equation (3.10) shows that they are at:

$$x^* = -(s \pm 1)/m. \tag{3.11}$$

Equations (3.5)–(3.7) and their boundary conditions are invariant under translations in y and z, and also under translation in x by δ when accompanied by a stream-wise boost in velocity of $\sigma\delta$. The latter symmetry is *s*hift-and-boost symmetry, c.f., [Goldreich and Lynden-Bell 1965; Marcus and Press 1977] and is the basis of the *s*hearing sheet boundary conditions [Balbus and Hawley 1998; Barranco and Marcus 2006]. Due to the shift-and-boost symmetry, the origin of the x-axis is not unique, so equation (3.14) has the following meaning: x^* is the cross-stream distance between a perturbation and the location of the baroclinic critical layer that it excites.

Eigenmodes with baroclinic critical layers are neutrally stable (i.e., s is real) and have singularities are in the vertical z components of their velocities and densities.To show their singularities , we solve the eigenvalue problem of linearized equations (3.5)–(3.7) in a 3D box that is periodic in y and z directions with box size L. The eigenfunction $\mathbf{g}(x)$ is expanded in Chebyshev series in x direction. The boundary conditions are $v_x' = 0$ at $x = \pm L_x/2$. We consider a linear shear velocity with $\bar{V}(x) = \sigma x$, where $\sigma = -3/2\Omega$ is constant and corresponding to the Keplerian shear. We set $\bar{N}/f = 1$ for the background vertical stratification. Under these parameters, we obtain x^* of baroclinic critical layers from equation (**??**):

$$x^* = \frac{(s \pm \bar{N})L}{2\pi|\sigma|m}, \tag{3.12}$$

where the vertical wave number is $k_z \equiv 2\pi q/L$ with q being an integer. Figure 3.3 shows the singularity in v_z and $\tilde{\rho}$ of an eigenmode with $m = 1$, $q = 1$ and corresponding to an eigenvalue $s = 0$. According to equation (3.12), their singularity is expected to be seen at $x^* = \pm 1$ shown in Figure 3.3*ab*.

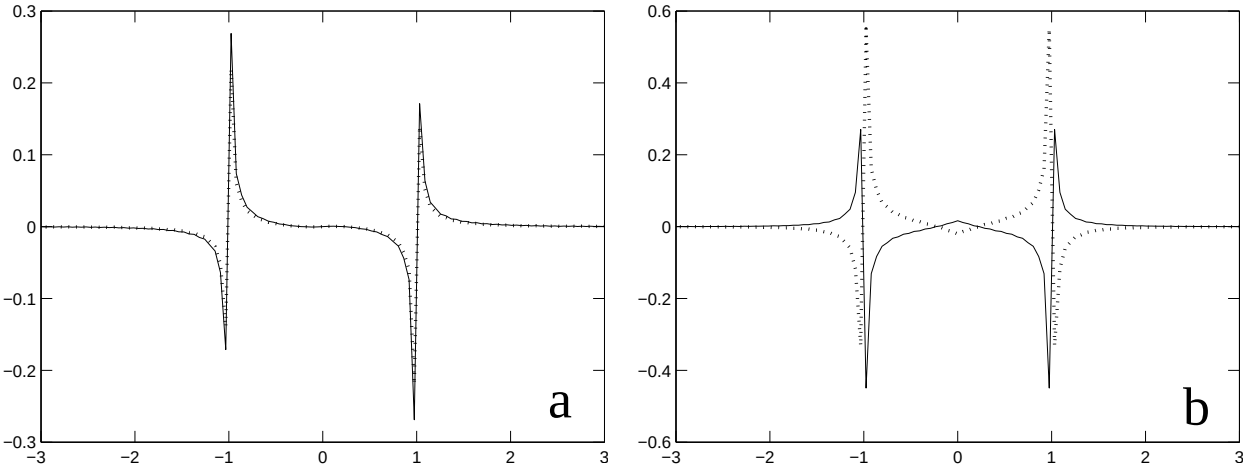

Figure 3.3: Plot of a) v_z' and b) $\tilde{\rho}$ of a baroclinic critical layer eigenmode along cross-stream direction. The horizontal axis is x. Solid line: real part of the eigenmode; dash line: imaginary part of the eigenmode.

Baroclinic critical layers are easily excited by small disturbances in our numerical simulations. They create large-amplitude vortex layers at the critical layers. The z-component of the curl of equation (3.6) gives

$$\partial\omega_z/\partial t = -(\mathbf{v}\cdot\nabla)\omega_z + (\boldsymbol{\omega}\cdot\nabla)v_z + (f+\sigma)(\partial v_z/\partial z), \tag{3.13}$$

where $\boldsymbol{\omega}$ is the relative vorticity with respect to the equilibrium flow, i.e., $\boldsymbol{\omega} \equiv \nabla\times(\mathbf{v} - \bar{V}(x)\,\hat{\mathbf{y}})$. equation (3.13) shows that the generalized Coriolis term $(f+\sigma)(\partial v_z/\partial z)$ is a source term for ω_z. Within the baroclinic critical layer, the z-component of the velocity is nearly anti-symmetric about x^*; on one side of the layer $v_z \to \infty$, and on the other side $v_z \to -\infty$; thus, the Coriolis term in equation (3.13) creates a large-magnitude vortex layer centered at x^* made up of dipolar segments with one side having cyclonic vorticity ($\omega_z f > 0$) and the other with anti-cyclonic vorticity ($\omega_z f > 0$) (c.f., Figure 3.1a). In contrast, barotropic critical layers do not form vortex layers; although their eigenmodes' v_y is singular, v_z is finite everywhere.

3.3 Numerical Simulation

To be relevant to the flows in PPDs, we only consider the case with $\sigma/f = -3/4$ and $0.5 \le \bar{N}/f \le 1$. Note that PPDs have anticyclonic shear and are periodic in their streamwise, or azimuthal, direction like the Couette flow studied here. To verify our computations, flows were computed with two independent codes. One code used shearing sheet method Barranco and Marcus 2006, which is commonly used in astrophysics community. The other used semi-analytic method with a periodicized sawtooth shear (described in Chapter 2) and

enforced an outward-going wave condition by putting sponge layers near x boundaries. These two codes produced similar results.

Many types of perturbations create zombie vortices. Most relevant to PPDs is a Kolmogorov spectrum of noise where the velocity and Rossby number $Ro \equiv \omega_z/f$ of the initial eddies scale respectively as $l^{1/3}$ and $l^{-2/3}$, where l is the eddy diameter. The smallest eddies have the largest vorticity and Ro. In our calculations, regardless of how small we make the amplitude of the initial Kolmogorov spectrum, if the spatial resolution is sufficient, the smallest eddies will have a sufficiently large Ro to trigger the instability and create zombie vortices. The details of simulations with initial Kolmogorov noise are discussed in next chapter. Here we focus on the formation and self-replication of the zombie vortices by perturbing the flows with a single vortex and a vortex pair.

3.4 Single Vortex Perturbation

Consider the flow in Figure 3.1 and Figure 3.1, which is initialized with a single anticyclone at the origin. It has $Ro = -0.31$ and volume $\sim 10^{-4}$ of the domain. It is embedded in the unperturbed flow $\bar{V}(x)$ and $\bar{\rho}(z)$. The velocity perturbation due to the initial vortex is significant only near the origin and is small, $\sim 10^{-2}\sigma L_x$, where L_x is the domain size in x. (Velocity perturbations in PPD studies are considered small when they are less than $\sim 0.1\sigma L_x$ [Balbus, Hawley, and Stone 1996].) Our initial vortex is in quasi-equilibrium as in [Barranco and Marcus 2005] such that equations (3.5) & (3.6), but not equation (3.7), are in steady equilibrium. The initial density perturbation is confined to the initial vortex. Equation (3.7) allows ρ and $N(x, y, z, t)$ to change. Figure 3.1 shows ω_z in an x–y plane. The perturbing vortex is nearly steady, so it excites critical layers with frequencies $s = 0$. Thus, equation (3.14) shows that the critical layers are at $|x^*| = 1/|m|$ with no critical layers at $|x| > 1$. Figure 3.1a shows vortex layers at these critical layers: ω_z appears at $x = 1/|m|$ as $|m|$ segments of dipolar stripes aligned in the stream-wise y direction for $|m| = 1$, 2 and 3. A Fourier analysis shows that the stripes have $s = 0$. We previously showed [Marcus 1993; 1990] that in shear flows with $f\sigma < 0$, cyclonic vortex layers aligned in the stream-wise direction are stable, whereas anticyclonic layers are unstable, roll-up into discrete anticyclones, and merge to form one large anticyclone. This behavior is seen in Figure 3.1b. The anticyclonic vorticity at $x = 1/3$ has rolled up and merged into a single anticyclone (near $y = 1.5$). The anticyclonic vorticity at $x = 1/2$ has rolled up into an anticyclone near $y = -0.5$. In contrast, the cyclonic ω_z near $x = 1/2$ has formed a continuous, meandering filament. At later times (Figure 3.1c), the anticyclones near $x = 1/3$ (and near $y = 2$) and near $x = 1/2$ (and near $y = -1$) have become larger. Figure 3.1c and Figure 3.1d show critical layers and vortices at $|x| > 1$, which cannot be created by perturbations at the origin. The layers at $|x| > 1$ are due to the self-replication of 1^{st}-generation vortices at $|x| \leq 1$. A vortex at *a*ny location will excite critical layers in a manner exactly like the original perturbing vortex due to the *s*hift-and-boost symmetry (and will have $s = 0$ when viewed in the frame moving with the perturbing vortex). Figure 1(c) shows 2^{nd}-generation critical layers at $x = 4/3$, $3/2$,

2, and 2/3 all with $|m| = 1$ and excited by 1^{st}-generation vortices at $x = 1/3$, $1/2$, 1, and $-1/3$, respectively. Figure 3.1d shows 3^{rd}-generation critical layers at $2 < x \leq 3$, and 4^{th}-generation critical layers forming at $x > 3$. At later times the vortices from $|m| = 1$ critical layers dominate (Figure 3.1d). At very late times, the vortices have cross-stream diameters of order unity. (See below.) Within each zombie vortex the density mixes so that it is in accord with its near hydrostatic and geo-cyclostrophic equilibrium (c.f., [Hassanzadeh et al. 2012]). However, there is horizontal, but very little vertical, mixing of density outside the vortices, so the background vertical density stratification and N remain within 1% of their initial unperturbed values. The lack of vertical mixing, despite strong horizontal mixing, was seen in our earlier simulations [Barranco and Marcus 2005] and laboratory experiments [Aubert et al. 2012] of vortices in rotating, stratified flows.

Figure 3.2 shows the flow in Figure 3.1 viewed in the x–z plane and illustrates our main result: at late times the domain fills with anticyclones. Because the initial flow is homogeneous with uniform σ and $\bar{N}$, the vortices form a regular lattice despite the flow's turbulence. As time progresses in Figure 3.2, the vortex population spreads out from the perturbing vortex at the origin. At early times (Figure 3.2a) the flow has 1^{st}-generation critical layers, with $|m| = 1$, 2, and 3 being most apparent. In this first generation, and all subsequent generations, a vortex perturbs the flow and creates four new prominent vortices at its $|m| = 1$ critical layers at locations in x that are $\pm l_x$ distant from itself and at locations in z that are $\pm l_z$ distant from itself. (l_x is physically set by, and equal to, the distance in x from a perturbing vortex to the anticyclonic piece of the vortex layer formed by its $|m| = 1$ critical layer; this distance is slightly greater than unity.) The 2^{nd}-generation $m = 1$ critical layers created by the 1^{st}-generation vortices with $|m| = 1$, 2, and 3 are faintly visible in Figure 3.2b and much more so in Figure 3.2c. At later times (Figure 3.2d), the $|m| = 1$ vortices descended from the 1^{st}-generation $|m| = 1$ vortices dominate and form a lattice of zombie vortices located at $[x = 2j\, l_x, z = 2k\, l_z]$ and at $[x = (2j+1)l_x, z = (2k+1)l_z]$, for all integers j and k.

The characteristic $|Ro|$ of late-time zombie vortices in Figure 3.1 and Figure 3.2 is ~ 0.2, consistent with zombie vortices in flows initialized with noise. After a vortex forms, its $|Ro|$ intensifies to its approximate peak value within a few of its turn-around times, and it remains near that value indefinitely. To examine the energy of the vortices and discover its source, we decomposed the flow's energy into two orthogonal parts: (1) the $z$onal component consisting of the kinetic energy of the stream-wise velocity component with Fourier modes $k_z = k_y = 0$ (i.e., the background shearing flow); and (2) the $n$on-zonal component consisting of everything else. If the initial flow were unperturbed, then the initial energy would be all zonal. In the flow in Figure 3.1 and Figure 3.2, there is a small initial non-zonal component due to the initial vortex at the origin. At later times, the non-zonal component represents the energy of the initial vortex and the zombie vortices (and turbulence and waves). After initial transients with faster than exponential growth, the non-zonal energy increases approximately exponentially with an e-folding time of ~ 1000 from just after the time of Figure 3.2a to times later than that in Figure 3.2d. The non-zonal energy in Figure 3.2d is more than 400 times larger than its initial value. The energy is supplied by the zonal energy. This is

proved in detail in Chapter 6. If the self-replication were self-similar, we would expect the perimeter of the front between the vortex-populated flow and unperturbed flow in each x-z plane to grow as t and the number of vortices to increase as t^2, which is consistent with our calculations.

3.5 Waves and Vortex Pair Perturbation

Our numerical simulations with wave generator show that they can excite critical layers and form vortex lattices by breaking and producing closely-spaced pairs of anticyclones, which in turn excite critical layers. This is showed in Figure 3.4*ab*. The 4 pairs of critical layers in Figure 3.4*b* are created by the vortex pair near the origin. They are growthing in time and roll up into vortices at time later than Figure 3.4*b*. The energy supplies their growth is extracted from the background shear by the vortex pair instead of the wave generator. This has been seen in the earlier time of the simulation: those 4 pairs of critical layers are produced once the vortex pair forms. It is also proved by the designed numerical simulation in the next chapter.

To better understand how vortex pairs self-replicate. we performed numerical simulation with an initial condition consisting of the equilibrium $\bar{V}(x)$ superposed with a pair of small volume, almost spherical anticyclones near the origin separated in x by a small distance Δ. Figure 3.5*abcd* illustrates how vortex pair self-replicate and form vortex lattices. The main difference between this flow and the one initialized with single vortex perturbation is that $s \neq 0$ because the two initial anticyclones advect in opposite stream-wise directions with an approximate relative speed between them of $|\sigma\Delta|$. Because the stream-wise direction has a periodicity length of L_y, this advection perturbs the flow with temporal frequencies $(2\pi\sigma\Delta)/(pL_y)$, where p is a non-zero integer. Fourier analysis confirms that the baroclinic critical layers are excited with $s = (2\pi\sigma\Delta)/(pL)$ (as observed in any frame), and, in accord with equation (3.13), the layers are at

$$x^* = \pm(1/m) \pm \Delta/(pm), \tag{3.14}$$

where the two $\pm$ terms in this expression are independent. It is less ambiguous and more insightful (when $\Delta \ll 1$, as is the case here) to think of the critical layers as forming in *p*airs with the pairs centrally located at $X = \pm 1/m$, and with the two critical layers in each pair separated from each other by a distance in x of $\Delta' = 2\Delta/|pm|$ (i.e., $x^* = X \pm \Delta'/2$). Each critical layer within a pair rolls up to form anticyclones at $z \simeq \pm X$ and such that the vortices within each pair are separated from each other in x by Δ'. The new anticyclones advect past each other and excite new critical layers in the same manner that the original pair of vortices did. If $|pm| = 2$, then $\Delta' \equiv \Delta$, and due to the shift-and-boost symmetry, the self-replication of the vortex pairs and critical layers is self-similar. A Fourier analysis of the flow in Figure 3.5*abcd* shows that the strong critical layers have $|pm| = 2$, and in Figure 3.5*d* the layers with $|p| = 2$, $|m| = 1$ are the strongest. These values of p and m create a face-centered lattice of anticyclone pairs.

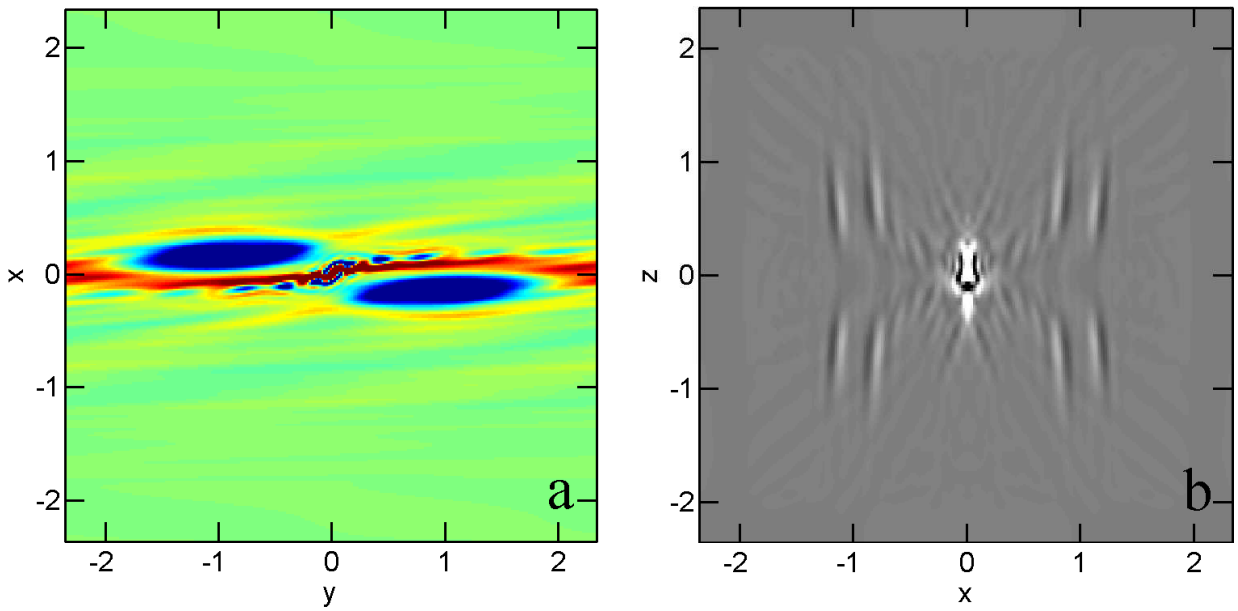

Figure 3.4: Wave generator excites strong layers by producing vortex pairs. The backgroud flow has $\sigma/f = -3/4$, $\bar{N}/f = 1$. The computational domain is a cubic box with size $L = 2.3562$. The wave generator placed at origin has frequency $s = 0.75\bar{N}$ and magnitude $A = 3.75 \times 10^{-4}(\Omega^2 L)$. Anticyclonic ω_z is blue and cyclonic ω_z is red, with the color is bluest at $\omega_z/f = -0.1$ and reddest at $\omega_z/f = -0.1$. a) $t = 607.37$, $x - y$ plane at z=0. The wave generator under the effect of background shear creates a pair anticyclonic vortices with a small separation distance $\Delta = 0.3314$ in the cross stream direction. b) $t = 670.21$, $x - z$ plane at y=0. 4 pairs of critical layers with $m = 1$ and separation distance Δ are produced centered at $|X| = 1$ by the counter moving vortices near origin. 4 weak pairs of $m = 2$ critical layers can also be seen near the $|X| = 1/2$. The wave generator is at origin. The diagonal line emitted from the origin are the $m = 0$ internal inertial-gravity waves. The 4 curved lines come from the wave generator are $m = 1$ internal inertial-gravity waves with the forcing frequency of the wave generator.

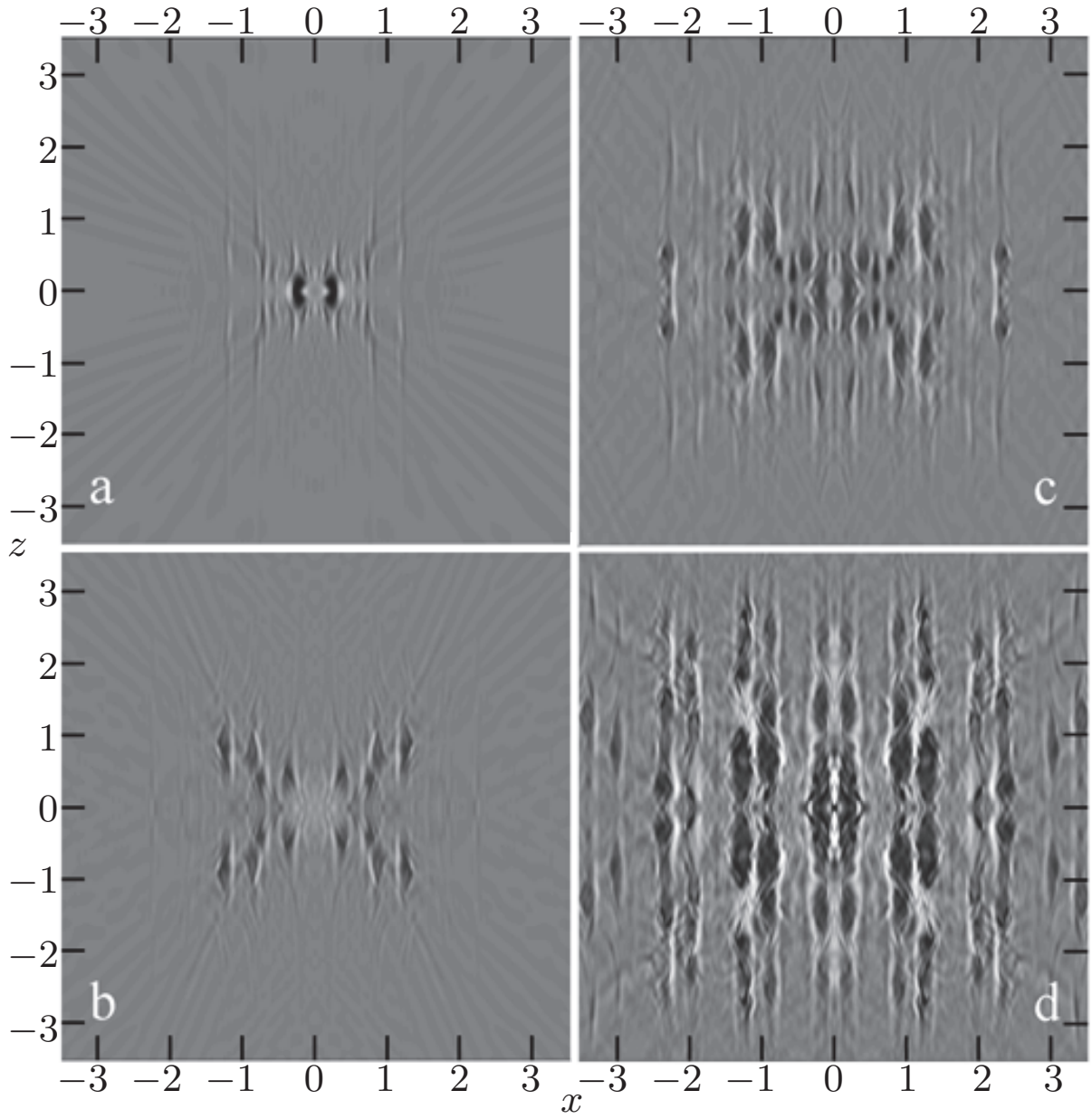

Figure 3.5: Zombie vortices sweep outward from the perturbing vortex pair at the origin in the x–z plane (at $y = 0$). Anticyclonic ω_z is black (darkest is $\omega/f = -0.2$) and cyclonic is white (lightest is $\omega/f = 0.2$). $f/\bar{N} = 1$ and $\sigma/\bar{N} = -3/4$. The $x-z$ domain has $|x| \le 4.7124$; $|z| \le 4.7124$, and is larger than the region shown. a) $t = 160/\bar{N}$. 1^{st}-generation critical layers with $|m| = 1$, 2 are visible at $|X| = 1$ and $1/2$. Diagonal lines are $k_y = 0$ internal inertia-gravity waves with shear, not critical layers. Initial vortex pair can also be seen near $x = 0$. b) $t = 576$. 1^{st}-generation vortex pairs with central location of the pair at $|X| = 1$ and $1/2$, roll-up from the critical layers with $|m| = 1$ and 2 in panel a, respectively. c) $t = 1856$. 2^{nd}-generation vortex pairs with $|X| = 0$ and 2 spawned from the 1^{st}-generation pairs near $|X| = 1$, and a weaker 2^{nd} generation with $|X| = 1/2$ and $3/2$ spawned by the weak 1^{st} generation with $|X| = 1/2$. d) $t = 3200$. 1^{st}, 2^{nd} and 3^{rd} generation vortex pairs. The lattice spacing of the pairs in the x direction is approximately unity, and the dominant critical layers all have $|p| = 2$, $|m| = 1$.

3.6 Energy and Saturation of Zombie Instability

Energy Analysis of Single Vortex

We present energy analysis of flow initialized with a single vortex perturbation to show the energy that supports the instability is extracted from the background zonal flow. The initial vortex here has Gaussian vorticity profile in all three directions and has a maximum Ro the same as the one in Chapter 3. In our numerical simulations, we use the decomposition $\mathbf{v} = \bar{V}(x)\hat{\boldsymbol{y}} + \boldsymbol{v}'$. However, this is not a good way to define zonal and non-zonal components of the flow because $\bar{V}(x)\hat{\boldsymbol{y}}$ and $\boldsymbol{v}'$ are not orthogonal to each other. The cross term $\int \bar{V} v'_y \, \mathrm{d}\mathcal{V}$ exists when computing the components of total kinetic energy. Here we use a decomposition that results in two orthogonal components of the total kinetic energy. To do that, we decompose the total velocity $\mathbf{v}$ as

$$\mathbf{v} = \bar{\bar{V}}(x,t)\hat{\boldsymbol{y}} + \hat{\boldsymbol{v}}(x,y,z,t), \tag{3.15}$$

where $\bar{\bar{V}}$ is the zonal velocity and $\hat{\boldsymbol{v}}$ is the non-zonal velocity. Note the difference between this decomposition and and the one used in the simulation are only in the stream-wise component of the velocity. The two decompositions are related as

$$\bar{\bar{V}}(x,t) = \bar{V}(x) + < v'_x(x,y,z,t) >_{yz} \tag{3.16}$$

$$\hat{v}_y = v'_y - < v'_y(x,y,z,t) >_{yz} \tag{3.17}$$

$$\hat{v}_x = v'_x \tag{3.18}$$

$$\hat{v}_z = v'_z, \tag{3.19}$$

where $<>_{yz}$ denotes the spacial average in stream-wise and vertical directions. With the new decomposition, there is no cross term when computing the total kinetic energy resulting in two orthogonal parts: zonal kinetic energy KEZ and non-zonal kinetic energy KEN. The total energy E of the Boussinesq flow can be written as $E \equiv KEZ + KEN + PE$, where PE denotes the perturbed potential energy. Each component of the energy are defined as

$$KEZ \equiv \int \frac{1}{2}\bar{\bar{V}}^2 \, \mathrm{d}\mathcal{V} - E_{ref} \tag{3.20}$$

$$KEN \equiv \int \frac{1}{2}|\hat{\boldsymbol{v}}|^2 \, \mathrm{d}\mathcal{V} \tag{3.21}$$

$$PE \equiv \int \tilde{\rho} g z \, \mathrm{d}\mathcal{V} \tag{3.22}$$

where $\tilde{\rho} = (\rho - \rho_0 - \bar{\rho})/\rho_0$, and all integrals are taken over the computational volume $\mathcal{V}$: $-L_x/2 \le x \le L_x/2$, $-L_y/2 \le y \le L_y/2$, $-L_z/2 \le z \le L_z/2$. In equation (3.20), we subtracts a constant reference energy $E_{ref} \equiv \int \frac{1}{2}\bar{V}(x)^2 \, \mathrm{d}\mathcal{V}$, which does not change with time. For linear shear $\bar{V}(x) = \sigma x$, we can derive the energy evolution equation for each components. The Boussinesq equations written in zonal and non-zonal velocities are

$$\boldsymbol{\nabla} \cdot \hat{\boldsymbol{v}} = 0, \tag{3.23}$$

$$\frac{\partial \bar{\bar{V}}}{\partial t}\hat{\boldsymbol{y}} + \frac{\partial \hat{\boldsymbol{v}}}{\partial t} = -\bar{\bar{V}}\frac{\partial \hat{\boldsymbol{v}}}{\partial y} - (\hat{\boldsymbol{v}}\cdot\boldsymbol{\nabla})\hat{\boldsymbol{v}} - \hat{v}_x\frac{\partial \bar{\bar{V}}}{\partial x}\hat{\boldsymbol{y}} + \hat{\boldsymbol{v}}\times f\hat{\boldsymbol{z}} - \boldsymbol{\nabla}\tilde{p} - f(\bar{\bar{V}} - \bar{V})\hat{\boldsymbol{x}}. \tag{3.24}$$

$$\frac{\partial \tilde{\rho}}{\partial t} = -\bar{\bar{V}}\frac{\partial \tilde{\rho}}{\partial y} - (\hat{\boldsymbol{v}}\cdot\boldsymbol{\nabla})\tilde{\rho} + \frac{\bar{N}^2}{g}\hat{v}_z. \tag{3.25}$$

We obtain evolution equations of KEZ and KEN by multiplying equation (3.24) by $\bar{\bar{V}}\hat{\boldsymbol{y}}$ and $\hat{\boldsymbol{v}}$ respectively, and then integrate over $\mathcal{V}$. Similarly, we obtain evolution equation of PE by multiplying equation (3.25) by gz and integrate over $\mathcal{V}$. Note all the variables are periodic in x and y, except terms including $\bar{\bar{V}}(x,t)$, which are not periodic in x because they contain σx. In vertical direction, variables are expanded in Chebyshev series and we have $\hat{v}_z = 0$ at $z = \pm L_z/2$. Many of the resulting terms can be written as perfect divergences which will integrate to zero with periodicity in x and y and the vertical boundary conditions. The leftover terms are the source/sink terms of the energy including the damping terms due to hyperviscosity:

$$\frac{\partial}{\partial t}(KEZ) = \mathcal{S}_1 + \mathcal{S}_2 + \mathcal{H}_{KEZ}, \tag{3.26}$$

$$\frac{\partial}{\partial t}(KEN) = -\mathcal{S}_2 + \mathcal{S}_3 + \mathcal{H}_{KEN}, \tag{3.27}$$

$$\frac{\partial}{\partial t}(PE) = -\mathcal{S}_3 + \mathcal{H}_{PE}. \tag{3.28}$$

The total energy evolution equation can be written:

$$\frac{\partial}{\partial t}E = \mathcal{S}_1 + \mathcal{H}_{KEZ} + \mathcal{H}_{KEN} + \mathcal{H}_{PE}. \tag{3.29}$$

where the source/sink terms are defined:

$$\mathcal{S}_1 \equiv -\int_{x=L_x/2} \sigma L_x(\hat{v}_y + \bar{\bar{V}} - \bar{V})\hat{v}_x \,\mathrm{d}y\,\mathrm{d}z, \tag{3.30}$$

$$\mathcal{S}_2 \equiv \int \sigma \hat{v}_x\hat{v}_y \,\mathrm{d}\mathcal{V} - \int f\hat{v}_x\bar{\bar{V}} \,\mathrm{d}\mathcal{V}, \tag{3.31}$$

$$\mathcal{S}_3 \equiv -\int \tilde{\rho}g\hat{v}_z \,\mathrm{d}\mathcal{V}. \tag{3.32}$$

$\mathcal{S}_1$ is the source/sink term of the total energy. This term is due to the fact that shear velocity is linear function of x but the boundary conditions of x are periodic. This inconsistency results in a surface integral term on the cross-stream boundaries that does not vanish. Physically, it represents the flow of energy into and out of the edges of the domain in the cross-stream direction. $\mathcal{S}_2$ and $\mathcal{S}_3$ are the source/sink terms that exchange energy between KEZ and KEN, KEN and PE. In equation (3.31), the first term on the right-hand-side is the dominant term of $\mathcal{S}_2$. The second term can be written in a divergence form as $\int \boldsymbol{\nabla}\cdot[f\hat{\boldsymbol{v}}B]\,\mathrm{d}\mathcal{V}$, where $B(x) = \int_0^x \bar{\bar{V}}(x')\,\mathrm{d}x'$. In general, $B(x)$ may not be periodic in x and

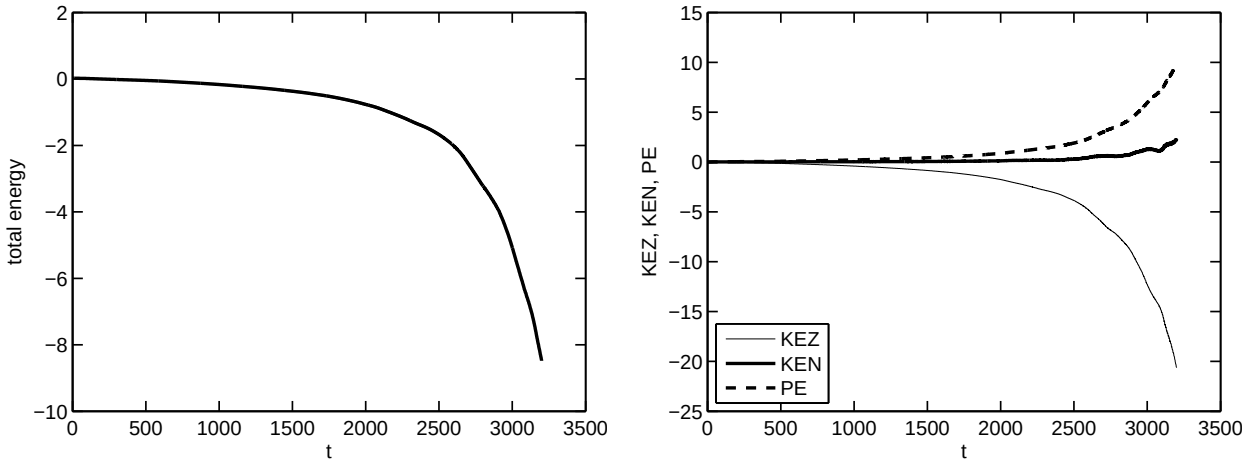

Figure 3.6: Time evolution of energy for single vortex simulation. Time is normalized by $1/\bar{N}$. Left panel: total energy. Right panel: energy components based on zonal and non-zonal decomposition. Solid thin line: KEZ; solid bold line: KEN; dash line: PE.

this term is not zero. However, throughout simulations, it is of several order of magnitude smaller than the first term. $\mathcal{H}_{KEZ}$, $\mathcal{H}_{KEN}$ and $\mathcal{H}_{PE}$ are hyperviscosity damping terms of the corresponding energy components.

Left panel of Figure 3.6 shows the total energy of the system decreases due to the hyperviscosity damping. The right panel shows the zonal kinetic energy decreases while the non-zonal kinetic energy and potential energy increase. By adding equations (3.27) & (3.28) together, only one source term $-\mathcal{S}_2$ exists. Therefore, the energy increase of non-zonal kinetic energy and potential energy must be due to energy transfered from the zonal flow. It is even more clear to look at the plots of right-hand-side terms of equations (3.26)–(3.28).

Figure 3.7 shows the right-hand-side terms of KEZ evolution equation (3.26). The dominant term is $\mathcal{S}_2$ (solid bold line), which is a sink term extracting huge amount of energy from zonal flow. As more zombie vortices are produced, the term grows dramatically in magnitude, indicating more energy are extracted from the zonal flow. $\mathcal{S}_1$ (dash line) is the source/sink term due to the shearing sheet boundary condition. It is very small during the simulation. This is because it is a surface integral term evaluated on the cross-stream boundaries. We intended to use a large domain in the cross-stream direction. So unless zombie vortices are close to the cross-stream boundaries, the effect of this term can be negligible comparing to $\mathcal{S}_2$. The hyperviscity term $\mathcal{H}_{KEZ}$ (solid thin line) is also negligible.

Figure 3.8 shows the right-hand-side terms of KEN evolution equation (3.27). Here the source term is $-\mathcal{S}_2$ (solid bold line), which is a source term that transfers kinetic energy from zonal to the non-zonal component. It is this amount of energy that supplies the instability to grow. $\mathcal{S}_3$ (dash line) is a sink term that transfers part of the income energy to the potential energy. $\mathcal{H}_{KEN}$ (solid thin line) is the hyperviscosity damping of the non-zonal kinetic energy. It is not a small term and increases with time. The reason is hyperviscosity acts like a

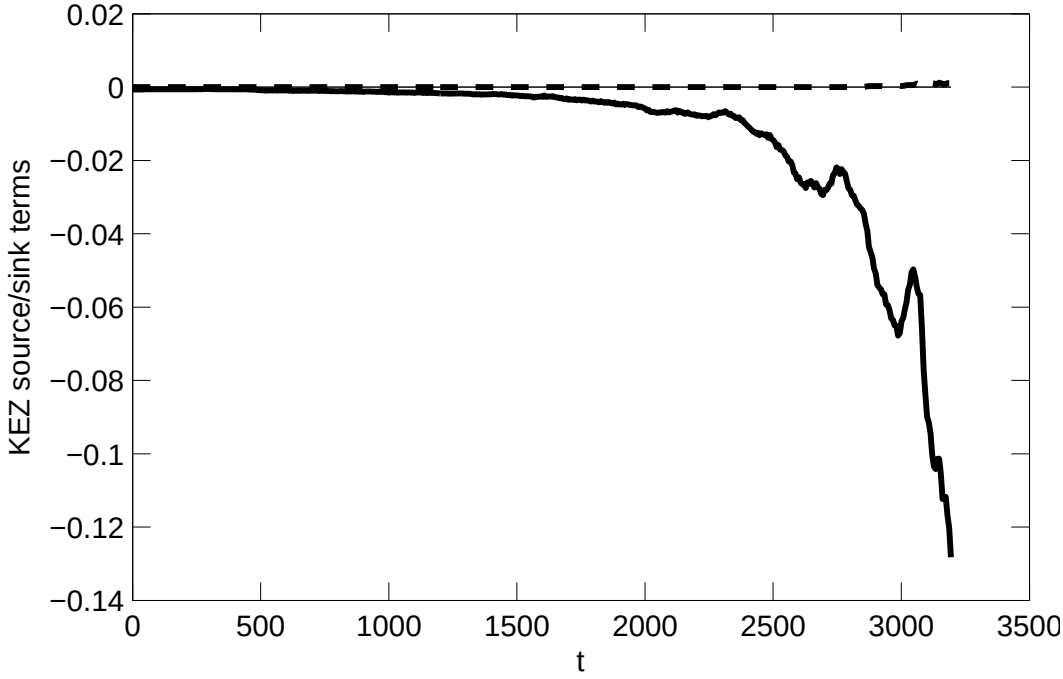

Figure 3.7: Source/sink terms of zonal kinetic energy KEZ. The original data oscillate dramatically in time. A moving average with a window size of $127(1/\bar{N})$ is used for better visualization. Dash line: $\mathcal{S}_1$; solid bold line: $\mathcal{S}_2$; solid thin line: $\mathcal{H}_{KEZ}$. (The dash line and the solid thin line almost lie on each other.)

low-pass filter in space. As more zombie vortices are produced, the flow becomes more turbulent and produces lots of small scale structures which are damped by the hyperviscosity. During the instability, the source term $-\mathcal{S}_2$ is greater than the summation of the two sink terms resulting in a net increase of non-zonal kinetic energy as showed in the right panel of Figure 3.6 (solid bold line).

Figure 3.9 shows the right-hand-side terms of PE evolution equation (3.27). $-\mathcal{S}_3$ (solid bold line) is a source term that transfers energy from non-zonal kinetic energy to potential energy. $\mathcal{H}_{PE}$ (solid thin line) is the hyperviscosity damping of potential energy, which is very small. The potential energy increase showed in right panel of Figure 3.6 (dash line) is almost purely due to the energy transfered from the non-zonal flow, which is part of the total amount of energy transfered from the zonal flow.

From above analysis, we conclude during the growth of the instability, energy that supports the instability is extracted from the zonal kinetic energy and transferred to the non-zonal kinetic energy. This amount of energy is divided into three parts. One part becomes the energy source to supply non-zonal kinetic energy growth, one part is continue transferred to the potential energy; the leftover part is damped by the hyperviscosity. The direction of energy transfer is from KEZ to KEN, then to PE. Once the instability begins, as more

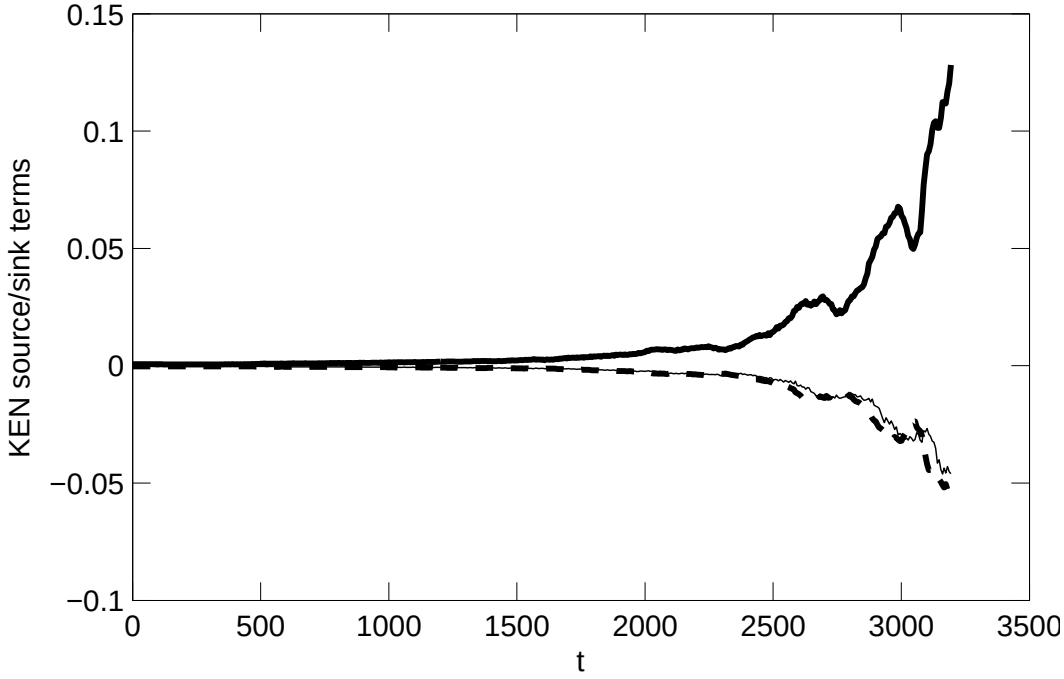

Figure 3.8: Source/sink terms of non-zonal kinetic energy KEN. The original data oscillate dramatically in time. A moving average with a window size of $127(1/\bar{N})$ is used for better visualization. solid bold line: $-\mathcal{S}_2$; dash line: $\mathcal{S}_3$; solid thin line: $\mathcal{H}_{KEN}$. (The dash line and the solid thin line almost lie on each other.)

zombie vortices are produced, more energy is extracted from the zonal flow.

Energy Extracted From Shear by Vortex Pair

In Chapter 4, we make the statement the energy that supplies the growth of the 4 pairs of critical layers (c.f. Figure 3.4b) is extracted from the background shear rather than provided by the wave generator. This can be proved by the following numerical experiment: at time showed in Figure 3.4b, we stop the wave generator forcing and let the flow continue to evolve in time. The 4 pair critical layers still grow and subsequently roll-up into 4 pairs of vortex, which generate new critical layers. This is because although the external forcing disappears, the vortex pair near origin still exist and continue extracting energy from the background shear to supply the instability to grow. The results are shown in Figure 3.10ab. Figure 3.10a shows the time evolution of non-zonal kintic energy KEN after turning off the wave generator forcing. The growth of KEN indicates energy is continuously supplied by zonal flows through KEN source term $-\mathcal{S}_2$. Figure 3.10$a$also shows a well-defined frequency. This frequency corresponds to the paasing-by frequency of the vortex pair at the origin $2\pi\Delta/|\sigma|L$. Equation (3.21) indicates KEN contains the first harmonic of the first fundamental frequency of the flow. The fundamental frequency of the flow is $\pi\Delta/|\sigma|L$, which is also the

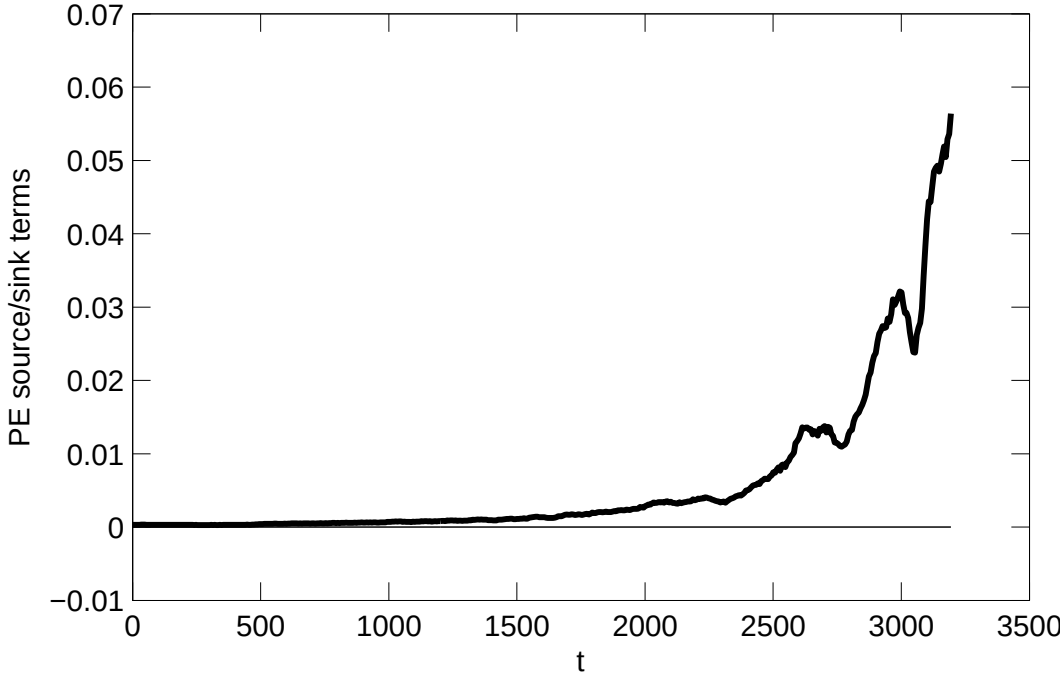

Figure 3.9: Source/sink terms of potential energy PE. The original data oscillate dramatically in time. A moving average with a window size of $127(1/\bar{N})$ is used for better visualization. solid bold line: $-\mathcal{S}_3$; solid thin line: $\mathcal{H}_{PE}$.

frequency associated with critical layers centered at $|X| = 1$, confirmed by Fourier analysis. The anticyclonic vortex layer pairs intensify and later roll up into vortex pairs centered at $|X| = 1$, which in turn excite next generation critical layer pairs centered at $X = 0$ as shown in Figure 3.10b.

Saturation of Zombie Instability

The exponential growth of the instability is due to the fact that vortices in the vortex-populated region grow exponentially in size, and not due to a long-term exponential increase of the velocity of each zombie vortex. Therefore, instability is expected to be saturated when the vortices fill the domain. Based on several numerical experiments, it appears that the late-time status of zombie vortices depend on the background parameters, $\bar{N}$, f and σ rather than on properties of the initial perturbation. In all simulations, $\sigma/f = -3/4$ are chosen to be relevant to PPDs, the saturated states of the flows only depend on $\bar{N}/f$. This is showed in Figure 3.11 by plotting the long time evolution of non-Keplerian kinetic energy $KE \equiv \int \frac{1}{2}|\boldsymbol{v}'|^2 \, \mathrm{d}\mathcal{V}$ of several different initial conditions including single vortex at different cross-stream locations, vortex pair, 2D and 3D noise with Kolmogorov spectrum but different initial kinetic energy. In these simulations, we have $f/\bar{N} = 1/2$. All the simulations use Fourier series in horizontal direction and Chebyshev series in vertical direction, except for

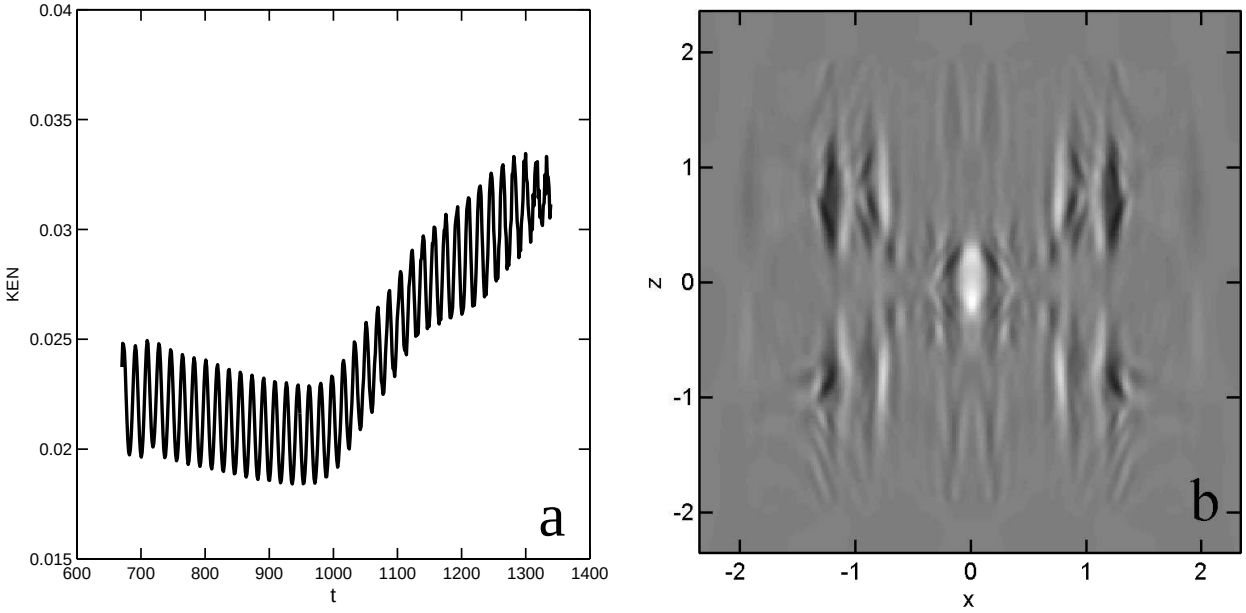

Figure 3.10: Energy supplied is extracted from background shear. All the parameters are the same as Figure 3.4 except the wave generator forcing is stopped at $t = 670.21$. The backgroud flow has $\sigma/f = -3/4$, $\bar{N}/f = 1$. The computational domain is a cubic box with size $L = 2.3562$. a) Non-zonal kinetic energy KEN evolution in time. b) $t = 1340.41$, $x - z$ plane at y=0. Anticyclonic ω_z is blue and cyclonic ω_z is red, with the color is bluest at $\omega_z/f = -0.1$ and reddest at $\omega_z/f = -0.1$. 4 pairs of critical layers in Figure 3.4b roll up into 4 pairs of vortex centered at $|X| = 1$. 2^{nd} generation of critical layer pairs are excited centered at $X = 0$.

the one with blue dot dash line, which use Fourier series in all directions. Despite their differences, when zombie instability saturate, they all have the same level of KE as shown in Figure 3.11.

Their flows look very similar, whose cross-stream direction are filled with 7 zombie vortices. For instance, the late time results of the flows initialized with a single vortex at origin are shown in Figure 3.12ab. The reason that there are only 7 zombie vortices rather than 9 (Analytically, the flow will contain 9 critical layers in the cross-stream direciton.) is because each of these well-developed vortices could have their cross-stream diameters slightly larger than 1. This is confirmed by the plot of non-Keplerian kinetic energy spectrum as a function of corss-stream Fourier mode, shown in Figure 3.13. All the data in the plot are taken when the flows saturate. A peak can be seen for all the spectrum at $|n| = 7$, which confirms the cross-stream flow structures shown in Figure 3.12ab. It is showed energy is extracted from background zonal flow to non-zonal flow, the peak shows this amount of energy is injected to the non-zonal flow at a cross-stream length scale corresponding to $|n| = 7$, the cross-stream length scale of zombie vortices. This implies zombie vortices are responsible for energy ex-

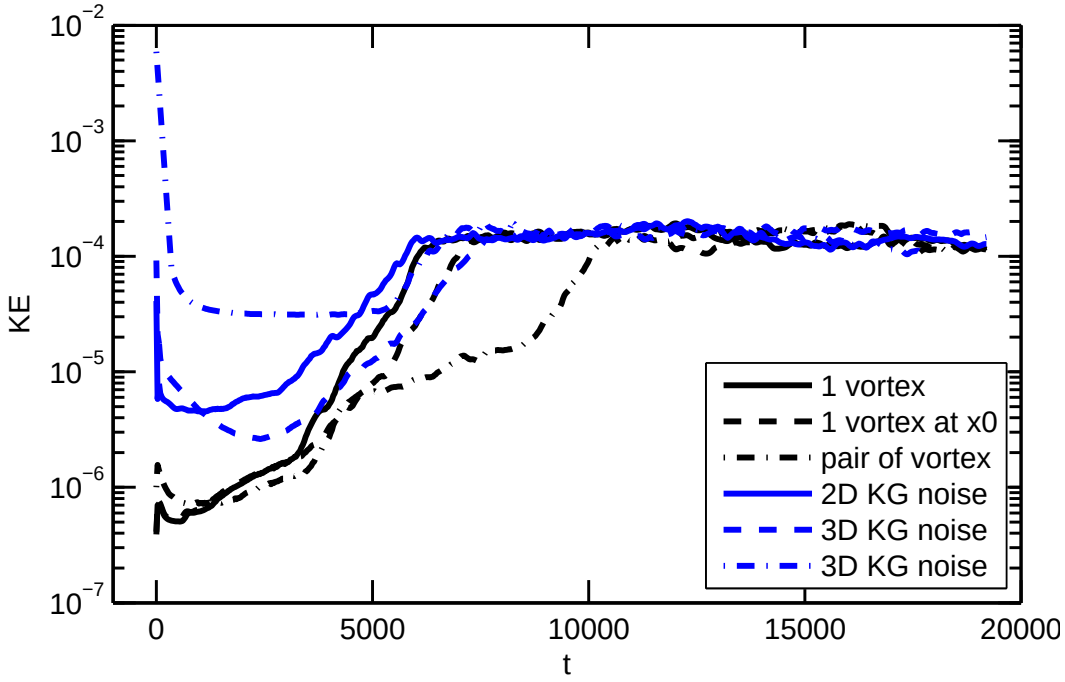

Figure 3.11: Long time non-Keplerian kinetic energy evolution. A moving average with a window size of $127(1/\bar{N})$ is used for better visualization. All the simulation have background parameters $\sigma/f = -3/4$ and $f/\bar{N} = 1/2$, and are performed in a cubic box with size $L = 4.7124$. Lines represents different initial conditions. Black solid line:a single Gaussian vortex at $x = 0$, $y = 0$ and $z = 0$; Black dash line: a single Gaussian vortex at $x = 3.7699$, $y = 0$ and $z = 0$; Black dot dash line: pair of Gaussian vortex with their center at $x = 0$, $y = 0$ and $z = 0$, and their separation distance $\Delta = 0.8247$. Blue solid line: 2D noise with Kolmogorov spectrum, $KE_0 = 4.1 \times 10^{-5}(\Omega L)^2$; Blue dash line: 3D noise with Kolmogorov spectrum, $KE_0 = 9.2 \times 10^{-5}(\Omega L)^2$; Blue dot dash line: 3D noise with Kolmogorov spectrum, $KE_0 = 5.9 \times 10^{-3}(\Omega L)^2$.

traction. The spectrums have slope of $-5/3$ from the peak downwards to high wave number modes, indicating these zombie vortices are surrounded by turbulent flows. All the spectrum collapse to nearly a single curve at scles smaller than the charactertistic cross-stream length scale of zombie vortices, despite their huge different initial condtions.

3.7 Conclusion

We have shown that linearly, neutrally stable plane Couette flow becomes finite-amplitude unstable when it is vertically stably-stratified. In the examples here, baroclinic critical layers are excited by a small vortex or a vortex pair, but our calculations show that a variety of small-volume, small-energy perturbations cause critical layers to grow and roll-up into

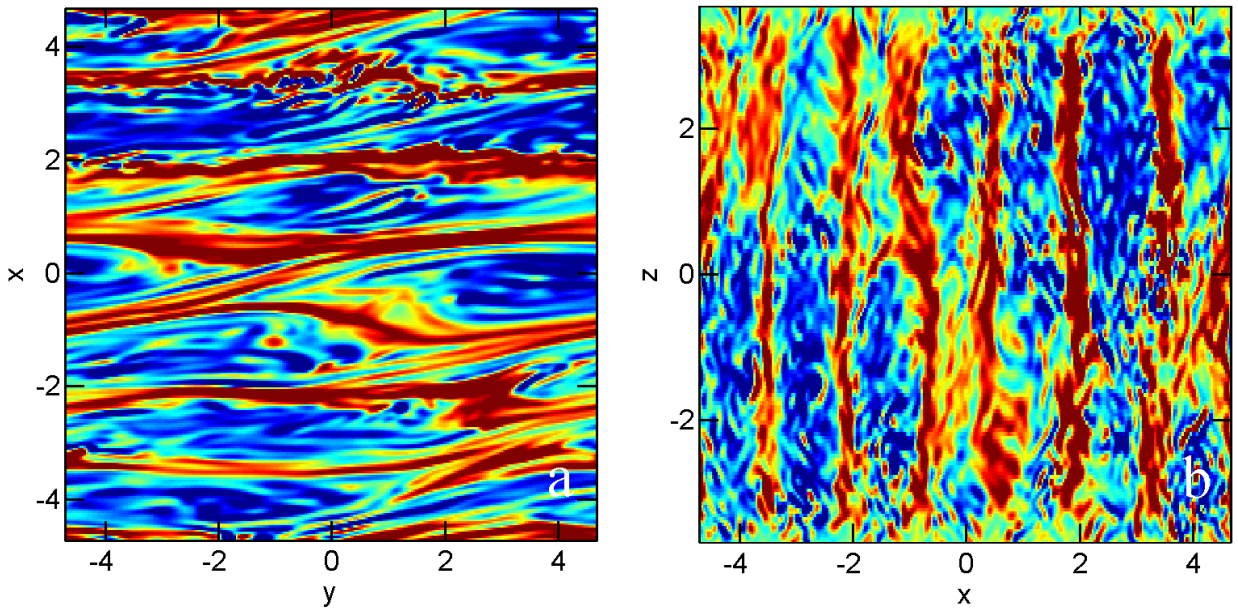

Figure 3.12: Well-developed zombie vortices fill the domain at late time $t = 19200$. The background flow has $\sigma/f = -3/4$, $\bar{N}/f = 1/2$. The initial condition is a single Gaussian vortex placed at the origin with a maximum $Ro = -0.3125$. Anticyclonic ω_z is blue and cyclonic ω_z is red, with the color is bluest at $\omega_z/f = -0.25$ and reddest at $\omega_z/f = -0.25$. a) $x - y$ plane at $z = 0$. There are 7 zombie vortices filled in the cross-stream direction. b) $x - z$ plane at $y = 0$. Vertical boundary damping are used in this simulation. Here the damping regions are cropped for better visualization.

large-volume, large-energy vortices. In general, this instability self-replicates with each new vortex exciting new layers that roll-up until the domain fills with compact 3D (i.e., not Taylor columns) vortices. The robustness of zombie vortices is evident from the fact that survive indefinitely even though they are embedded in a turbulent flow at late times. They survive by drawing energy from the background shear flow. For constant $\bar{N}$ and σ, the unperturbed flow is homogeneous, and vortex self-replication is self-similar with zombie vortices forming a regular lattice. The regularity of the lattice allows for reinforcement: each vortex re-excites four other vortices in the lattice, and each vortex in the lattice is continually re-excited by four other vortices. Zombie vortices occur frequently in our simulations of Boussinesq, anelastic and fully-compressible fluids, so they pose a paradox: if they are so common, why have they not been reported earlier? We believe the reasons are as following:

One reason that our instability was not discovered previously is that we use a spectral, rather than a finite-difference or finite-volume numerical method. Spectral methods can resolve features that are approximately 1216 times smaller (in each spatial dimension) than a second-order finite-difference calculation with the same number of computational elements. Our instability is 3D, and to be simulated, it requires a 3D code with radial resolution of

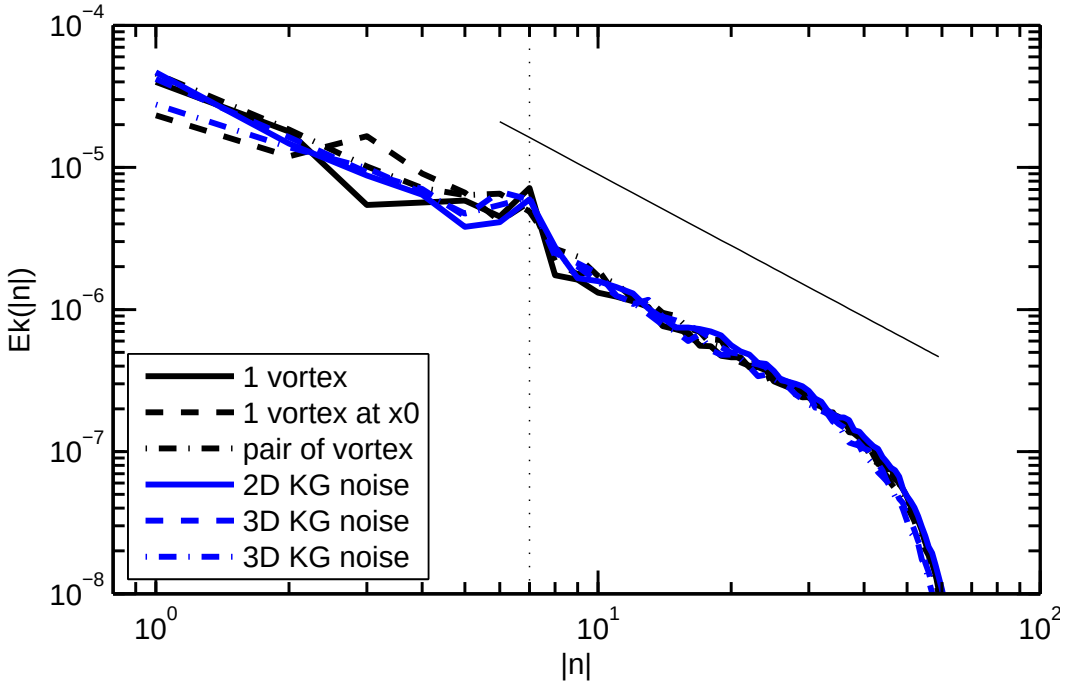

Figure 3.13: Kinetic energy spectrum as function of cross-stream Fourier mode $|n|$, where $kx \equiv 2\pi n/L_x$ with n being an integer. Background parameters and legend are the same as Figure 3.11. All the spectrum data are at time $t = 19200$ except for blue dash dot line (the last in the legend) has data at $t = 17600$. Thin solid line: $|n|^{-5/3}$; Vertical thin dot line: $n = 7$.

the PPD that is better than $H = 10$, where H is the vertical pressure scale height. Most previous PPD calculations did not have the required resolution.

A more fundamental reason that our new instability was not previously discovered is that much of the PPD literature used constant-density fluids, c.f., [3] or ideal gases in which the initial density was uniform in the vertical direction, rather than stably stratified. Rayleighs criterion for centrifugal stability applies only to fluids with constant density and therefore is not relevant to PPDs where the density falls off approximately like a Gaussian away from the midplane. Instabilities have not been systematically sought in stratified Couette flows [Le Bars and Le Gal 2007]. With few exceptions [Tevzadze, Chagelishvili, and Zahn 2008], stability studies of ideal gases in PPDs were carried out with no initial vertical stratification. For instance, one stability study of PPDs [Balbus, Hawley, and Stone 1996] argues that the stability of a PPD is governed by Rayleighs centrifugal criterion (i.e., PPDs are both linearly and nonlinearly stable), and another initial-value study of PPDs [Shen et al. 2006] with a very high spatial resolution did not show our new instability. However, both studies initialized the flow with constant density even though they both used an ideal gas equation of state. We can only speculate on why non-onstant density flows have been overlooked

in previous stability analyses of PPDs, but there appears to be a belief that if a fluid flow with a constant density is stable, then the same flow with a density that is vertically stably-stratified is even more stable. This belief is not true, and zombie instability requires stable vertical stratification. These omissions eliminate baroclinic instabilities.

Zombie vortices occur in our calculations of the dead zones of protoplanetary disks, which suggests that they may have an important role in star and planet formation[Barranco and Marcus 2005]. In addition, zombie vortices should be observable in laboratory circular Couette flows with stratified salt water for parameter values where the flow is linearly stable with respect to centrifugal instability [Drazin and Reid 1981a], SRI [Le Bars and Le Gal 2007; Molemaker et al. 2001; Yavneh et al. 2001] and other instabilities [Le Dizés and Billant 2009].

Chapter 4

The Dead Zones of PPDs Are Not Dead

4.1 Introduction

Angular momentum transport plays an important role in the structure and evolution of an accretion disk. Collisional viscosity is thought to be very inefficient at angular momentum transport; thus, one must appeal to transport by a turbulent viscosity [Shakura and Sunyaev 1973]. In magnetized accretion disks, this turbulence is thought to be generated and sustained by the magnetorotational instability (MRI) [Balbus and Hawley 1991], first proposed by [Chandrasekhar 1960; Velikhov 1959]. However, some regions of the disks around a protostar (protoplanetary disk, or PPD) are too cold and neutral to effectively couple to a magnetic field [Gammie 1996]. These regions are stable to MRI, and are thus referred to as "dead zones." However, angular momentum must somehow be transported through the dead zone in order for protostars to accrete and become stars.

There has been substantial effort to determine whether or not a Keplerian shear flow is hydrodynamically stable or unstable. Such a shear flow is linearly stable, as its angular momentum increases with radius [Rayleigh, Lord 1916]. There have been some claims that a Keplerian shear flow may be *nonlinearly* unstable, by analogy with non-rotating shear flows such as Taylor-Couette flow and Pouseuille flow. However, sustained turbulence has not be observed in numerical simulations ([Balbus, Hawley, and Stone 1996], hereafter BHS96; [Shen et al. 2006], hereafter SSG06;) or laboratory experiments ([Ji et al. 2006]; though see [Balbus 2011; Paoletti and Lathrop 2011; Schartman et al. 2012] for some recent controversy). Because the Keplerian shear flow appears to be hydrodynamically stable, many have investigated whether additional physics can render the flow unstable [Klahr and Bodenheimer 2003; Lesur and Papaloizou 2010; Lovelace et al. 1999; Molemaker et al. 2001; Yavneh et al. 2001]. We find these instability mechanisms unsatisfying, as they either require subtle conditions or rely on unphysical initial and boundary conditions.

In this chapter, we study the effects of vertical stratification on a Keplerian shear flow,

building on the work of [Barranco and Marcus 2005][hereafter BM05], [Barranco and Marcus 2006][hereafter BM06], and [Marcus, Pei, et al. 2013][hereafter MPJH13]. A thin, isothermal accretion disk in hydrostatic equilibrium is stably stratified, and has a buoyancy (Brunt-Väisälä) frequency N which increases linearly from the mid-plane. We show that in simulations of a uniformly, stably stratified, small amplitude random noise is unstable to the formation of large, coherent vortices. We ran simulations using our anelastic pseudo-spectral code (BM06), as well as the Athena code [Gardiner and Stone 2008; Stone, Gardiner, et al. 2008], which solves the fully compressible equations. The instability is present in both codes, and has similar characteristics.

The linear evolution of vertically stratified Keplerian shear flows has been studied extensively [Salhi and Cambon 2010; Salhi, Lehner, et al. 2013; Tevzadze, Chagelishvili, and Zahn 2008; Tevzadze, Chagelishvili, Zahn, et al. 2003; Volponi 2010]. These papers study the transient amplification of leading vortex modes via shearing, which can then couple to long-living spiral-density waves. However, they do not provide any (nonlinear) mechanism by which the spiral-density waves could regenerate the leading vortex modes. This style of analysis also neglects any instability of the shearing vortex modes, such as Kelvin-Helmholtz instabilities (e.g., SSG06), which inhibit transient amplification.

In addition, several groups have simulated the fully nonlinear evolution of vertically stratified Keplerian shear flows [Fleming and Stone 2003; Fromang and Papaloizou 2006; Oishi and Mac Low 2009]. These three papers describe simulations of accretion disks composed of magnetized plasma whose magnetic resistivity becomes large near the mid-plane. Although the MRI is present far from the mid-plane, the large magnetic resistivity prevents the plasma from efficiently coupling to the magnetic field near the mid-plane. Thus, an MRI-stable "dead zone" forms near the mid-plane.

These simulations show no sign of a hydrodynamic instability of the dead zone. This is completely consistent with our results, which show that the instability is only present for simulations with at least 128 grid points or modes in the radial direction per pressure scale height. [Fromang and Papaloizou 2006] uses a resolution of 30 radial points per pressure scale height, and [Fleming and Stone 2003; Oishi and Mac Low 2009] use at most 64. Furthermore, the growth time of the instability is hundreds of orbits, whereas previous studies only integrated for at most one hundred orbits.

In this chapter, we focus on flows with constant vertical stratifications. We show that the amplitude threshold for zombie instability is vorticity rather than velocity. We propose that in the limit of very small dissipation (as the flows in PPDs), zombie instability is effetively an linear instability. Only extremely small initial perturbations would be required to seed it. How zombie instability will affect the angular momentum transport in PPDs is also discussed. Finally, we speculate there might not be laminar Keplerian disks at all. The disk are essentially turbulent.

4.2 Equations for the Fluid Motion in Local PPD Approximation

The stability of flows in protoplanetary disks have been examined using a variety of approximations to the equations of motion Here, we limit ourselves to approximations in which the curvature of the disk is ignored and in which the unperturbed azimuthal flow is expanded locally around a fiducial cylindrical radius R_0. Hill [Hill 1878] was the first to carry out this type of expansion. We consider only fluid that with no dissipation and no radiative transfer.

Ideal, fully compressible flow

Consider a disk in which the unperturbed steady flow is only in the azimuthal direction with an angular velocity $\Omega(R)$ such that

$$\Omega(R) \propto R^{-q}. \tag{4.1}$$

In the local Cartesian approximation around R_0, Euler's equation for an observer in a frame rotating with angular velocity $\Omega_0 \equiv \Omega(R_0)$ around the z-axis is:

$$\begin{aligned} &\frac{\partial \mathbf{v}}{\partial t} + (\mathbf{v}\cdot\boldsymbol{\nabla})\mathbf{v} = -\frac{1}{\rho}\boldsymbol{\nabla} P \\ - \quad &2\Omega_0\,\hat{\mathbf{z}}\times\mathbf{v} + 2q\Omega_0^2\,x\,\hat{\mathbf{x}} - g(z)\,\hat{\mathbf{z}}, \end{aligned} \tag{4.2}$$

where $\mathbf{v}(x,y,z)$ is the gas velocity written in the Cartesian approximation, where P and ρ are the gas pressure and density, $-2\Omega_0\,\hat{\mathbf{z}}\times\mathbf{v}$ is the Coriolis term, $2q\Omega_0^2\,x$ is the tidal acceleration that arises from the difference between the centrifugal acceleration $-R\Omega^2(R)$ and the quantity $R_0\Omega^2(R_0)$, $-g(z)$ is the acceleration of gravity in the z direction, and where a "hat" above a coordinate means the unit vector in that coordinate's direction. The Cartesian approximation in eq. (4.2) uses $x \ll R_0$, where the Cartesian x coordinate corresponds to the cylindrical radial direction with $x \equiv R - R_0$, where the Cartesian y coordinate corresponds to the azimuthal ϕ coordinate with $y \equiv -R_0\phi$, and where z is identical in the Cartesian and cylindrical coordinate systems. Using the same local Cartesian approximation, the continuity equation becomes

$$\frac{\partial \rho}{\partial t} + \boldsymbol{\nabla}\cdot(\rho\mathbf{v}) = 0, \tag{4.3}$$

and the energy equation becomes

$$\frac{\partial \rho\epsilon}{\partial t} = -\boldsymbol{\nabla}\cdot(\rho\epsilon\mathbf{v}) - P\,(\boldsymbol{\nabla}\cdot\mathbf{v}), \tag{4.4}$$

where ϵ is the internal energy of the gas. Following BHS96, we write $\epsilon \equiv (3/2)\mathcal{R}T$, where $\mathcal{R}$ is the gas constant, T is the gas temperature, and the ideal gas equation of state is

$$P = (\gamma - 1)\rho\epsilon = \mathcal{R}\rho T, \tag{4.5}$$

where γ is the ratio of the specific heats at constant pressure and constant volume and set to 5/3. The steady, unperturbed equilibrium velocity (written with an overbar) that satisfies eqs. (4.2) – (4.5) is

$$\bar{v}_x = \bar{v}_z = 0 \tag{4.6}$$

$$\bar{v}_y = -q\Omega_0\, x. \tag{4.7}$$

The steady equilibrium pressure and density, that satisfy eqs. (4.2) – (4.5) are functions of z only and obey the hydrostatic equation:

$$d\bar{P}(z)/dz = -\bar{\rho}(z)g(z). \tag{4.8}$$

The steady equilibrium internal energy and temperature are also functions of z only and satisfy the equation of state: $\bar{\epsilon}(z) = (3/2)\bar{P}(z)/\bar{\rho}(z)$ and $\bar{T}(z) = \bar{P}(z)/[\mathcal{R}\bar{\rho}(z)]$.

Because there is no thermal radiation, diffusion, or dissipation in equations (4.2) – (4.5), there is a degeneracy of the allowable steady equilibrium thermodynamic solution. In general, one thermodynamic quantity, $\bar{P}(z)$, $\bar{T}(z)$, $\bar{\rho}(z)$, or $\bar{\epsilon}(z)$ can be arbitrarily specified (but see the one exception to this degeneracy explained in the next paragraph). Once that quantity is specified the others follow uniquely (up to a constant of integration) from the hydrostatic equation and the equation of state.

In the Cartesian approximation of a Keplerian disk in which the self-gravity of the gas is ignored, but the vertical z component of the gravity from the central object is included, $g(z) = -\Omega_0^2\, z$, where $z = 0$ is the mid-plane of the disk. This vertical gravity was used in our anelastic calculations in BM05 and BM06 along with the choice that $\bar{T}(z)$ is constant (motivated by models such as [Chiang and Goldreich 1997]). This calculation produced *z*ombie vortices. In contrast, the disk stability studies in BHS96, and in SSG06 use equations eqs. (4.2) – (4.5) with $g(z) \equiv 0$, and, as we show in § 6, the latter approximation prohibits the *z*ombie instability. When $g = 0$, the steady state equilibrium pressure corresponding to the steady velocity in eqs. (4.6) – (4.7) must be constant, and therefore cannot be an arbitrary function of z. However, $\bar{T}(z)$ or $\bar{\rho}(z)$ or $\bar{\epsilon}(z)$ can still be arbitrarily specified. In the stability calculations in BHS96, and in SGS06 with $g = 0$, the steady equilibrium internal energy, temperature and density were all chosen to be constants (see § 3), so that the unperturbed disk flow is *b*arotropic (see [Kundu 1990] and below for definition).

Anelastic flows

The anelastic approximation to eqs. (4.2) – (4.5) is commonly used in atmospheric flows [Peter R Bannon 1996; Gough 1969; Ogura and Phillips 1962], where there is a reference density or steady equilibrium density $\bar{\rho}(z)$ that varies with z. In the anelastic approximation $\bar{\rho}(z)$ can be an arbitrary function of z, and the changes in $\bar{\rho}(z)$ with respect to z can be arbitrarily large. However, the anelastic approximation has two requirements for all locations and for all time: (1) $\left|\rho(x,y,z,t) - \bar{\rho}(z)\right| \ll \bar{\rho}(z)$, and (2) $\left|\mathbf{v}\right|$ must be much less than the isothermal speed of sound $C_s \equiv \sqrt{\mathcal{R}\,T}$ (or that the Mach number Ma must be small). The

latter requirement is not satisfied in many astrophysical flows, so the anelastic equations are not commonly used in astrophysics. However, it should be noted that both requirements are fulfilled in the computations of disk stability in BHS96, BM05, and in SSG06.

One computational nicety of using the anelastic approximation in an initial-value code is that at every time step conditions (1) and (2) can be examined, and it can be determined if the approximations required by the anelastic equations are still satisfied. For example, in BM05 we used the anelastic approximation to study the evolution of an initial vortex in the mid-plane of a protoplanetary disk and the subsequent formation of *z*ombie vortices off the mid-plane. At no time in our calculations did the Mach number exceed 0.1 or $\big|\rho(x,y,z,t) - \rho(z)\big|/\bar{\rho}(z)$ exceed 0.2.

The anelastic equations are usually written in terms of the steady equilibrium density $\bar{\rho}(z)$ and pressure $\bar{P}(z)$, where $\bar{P}(z)$ and $\bar{\rho}(z)$ satisfy the hydrostatic equation (4.8). The anelastic equations for disk flow were derived in BM06 from eqs. (4.2) – (4.5) by expanding in powers of $\big|\rho(x,y,z,t) - \bar{\rho}(z)\big|/\bar{\rho}(z)$. For a disk in which the angular velocity of the unperturbed steady equilibrium flow is proportional to R^{-q}, the anelastic version of the local Cartesian Euler equation (4.2) in the rotating frame becomes:

$$\begin{aligned} \frac{\partial \mathbf{v}}{\partial t} + (\mathbf{v}\cdot\boldsymbol{\nabla})\mathbf{v} &= -\frac{1}{\bar{\rho}(z)}\boldsymbol{\nabla}[P(x,y,z,t) - \bar{P}(z)] \\ - \quad 2\Omega_0\,\hat{\mathbf{z}}\times\mathbf{v} + 2q\Omega_0^2\,x\,\hat{\mathbf{x}} &- \frac{\rho(x,y,z,t) - \bar{\rho}(z)}{\bar{\rho}(z)} g(z)\,\hat{\mathbf{z}}. \end{aligned} \tag{4.9}$$

Using the anelastic approximation, the continuity equation (4.3)) becomes

$$\boldsymbol{\nabla}\cdot[\bar{\rho}(z)\mathbf{v}] = 0, \tag{4.10}$$

The equation of state and energy equation are most conveniently written in terms of the potential temperature (see BM05 and BM06). However, for the study presented here, we need not complicate the equations with potential temperature. The dissipationless anelastic equations, like the dissipationless fully compressible equations, have a degeneracy in the steady equilibrium thermodynamic solution so that the equilibrium temperature $\bar{T}(z)$ is arbitrary. Here, as in BM05, BHS96, and SSG96, we choose a constant $\bar{T}(z) = T_0$. For $\bar{T}(z) = T_0$, eq. (4.9) reduces to (see BM06):

$$\begin{aligned} \frac{\partial \mathbf{v}}{\partial t} + (\mathbf{v}\cdot\boldsymbol{\nabla})\mathbf{v} &= -\boldsymbol{\nabla}\frac{P(x,y,z,t) - \bar{P}(z)}{\bar{\rho}(z)} - \\ 2\Omega_0\,\hat{\mathbf{z}}\times\mathbf{v} + 2q\Omega_0^2\,x\,\hat{\mathbf{x}} &+ \frac{T(x,y,z,t) - T_0}{T_0} g(z)\,\hat{\mathbf{z}}. \end{aligned} \tag{4.11}$$

For $\bar{T}(z) = T_0$, we still use the continuity equation (4.10). Energy equation (4.4) and the equation of state (4.5) become

$$\frac{\partial T(x,y,z,t)}{\partial t} = -(\mathbf{v}\cdot\boldsymbol{\nabla})T - T w_z N^2(z)/g(z), \tag{4.12}$$

and

$$\frac{P(x,y,z,t)-\bar{P}(z)}{\bar{P}(z)} = \frac{\rho(x,y,z,t)-\bar{\rho}(z)}{\bar{\rho}(z)} + \frac{T(x,y,z,t)-T_0}{T_0}, \tag{4.13}$$

where $N(z) \equiv \sqrt{g(z)\,[(1/\gamma)(d\,ln\bar{P}/dz) - d\,ln\bar{\rho}/dz}$ is the Brunt-Väisälä frequency of the unperturbed steady equilibrium flow [Kundu 1990; Schwartzchild 1958]. For $\bar{T}(z) = T_0$,

$$N(z) = \sqrt{(1/\gamma - 1)\,g(z)\,(d\,ln\bar{\rho}/dz)} \tag{4.14}$$

Equations (4.10) – (4.14) are the governing anelastic equations for constant $\bar{T}(z)$. Note that the steady equilibrium solution to eqs. (4.10) – (4.14) is the same as the steady equilibrium solution to the fully compressible equations where $\mathbf{v}$ is given by eqs. (4.6) – (4.7), and the relation between $\bar{P}(z)$ and $\bar{\rho}(z)$ is given by the hydrostatic equation (4.8), and $\bar{T} = T_0$.

For $\bar{T} = T_0$ and *K*eplerian vertical gravity $g(z) = \Omega_0^2\, z$, $\bar{P}(z)$ and $\bar{\rho}(z)$ are Gaussian functions of z with

$$\bar{P}(z) = P_0 \exp\left[-z^2/(2H^2)\right], \tag{4.15}$$

$$\bar{\rho}(z) = \rho_0 \exp\left[-z^2/(2H^2)\right], \tag{4.16}$$

where $\rho_0 \equiv \bar{\rho}(z=0)$ and where $P_0 \equiv \bar{P}(z=0) = \mathcal{R}\,\rho_0\,T_0$, and $H \equiv \sqrt{\mathcal{R}\,T_0}/\Omega_0$, where H is the defined as the fiducial vertical pressure scale height (equal to the actual vertical scale height only at $z = H$). Note that

$$C_s = H\,\Omega_0 = (g/\Omega_0)(H/z), \tag{4.17}$$

where $C_s \equiv \sqrt{\mathcal{R}\,T_0}$ is the isothermal sound speed. In this case, the Brunt-Väisälä frequency is linear in z with $N(z) = \Omega_0^2\, z/\sqrt{\mathcal{R}T_0\gamma/(\gamma-1)} = (\Omega_0^2\, z/C_s)\sqrt{1-1/\gamma}$.

For $\bar{T} = T_0$ and *c*onstant gravity $g(z) = g_0$, $\bar{P}(z)$ and $\bar{\rho}(z)$ are exponential functions of z with

$$\bar{P}(z) = P_0 \exp\left(-z/H\right), \tag{4.18}$$

$$\bar{\rho}(z) = \rho_0 \exp\left(-z/H\right), \tag{4.19}$$

where $\rho_0 \equiv \bar{\rho}(z=0)$ and where $P_0 \equiv \bar{P}(z=0) = \mathcal{R}\,\rho_0\,T_0$, and $H \equiv \mathcal{R}T_0/g_0 = C_s^2/g_0$ is the vertical pressure scale height. In this case the Brunt-Väisälä frequency is constant $N = N_0 = g_0/\sqrt{\mathcal{R}T_0\gamma/(\gamma-1)} = (g_0/C_s)\sqrt{1-1/\gamma}$. For the anelastic equations with constant gravity, it is useful to define the dimensionless constant

$$\beta \equiv g_0/(H\,\Omega_0^2), \tag{4.20}$$

so that

$$C_s = \beta^{1/2} H\,\Omega_0 = \beta^{-1/2}(g_0/\Omega_0). \tag{4.21}$$

When β is unity, $C_s = H\,\Omega_0$, as in eq. (4.17), the case for Keplerian gravity. In this paper, all of the equations are solved in a Cartesian domain of size $L_x \times L_y \times L_z$. The dimensionless equations for anelastic flow (and for fully compressible flow) with constant T and constant gravity contain four dimensionless numbers: γ (which is always 5/3 in this paper), q (which is the negative of the shear of the steady equilibrium flow in eqs. (4.6) – (4.7) in units of Ω_0), H/L_x (which we set to unity throughout this chapter), and β (which is equal to $\gamma N_0^2/(\gamma-1)$ in units of Ω_0^2 and is therefore a dimensionless measure of the vertical stratification), that is

$$N_0/\Omega_0 = \sqrt{\beta(\gamma-1)/\gamma}. \tag{4.22}$$

In addition, two dimensionless number describe the size of the computational domain: L_y/L_x and L_z/L_x. Unless otherwise specified in this paper $L_y/L_x = L_z/L_x = 1$.

The anelastic approximation removes acoustic and sound waves from their solutions. For numerically computing weather in the Earth's atmosphere (which has low Mach numbers and which was the motivation for the development of the anelastic equations), the filtering has been shown, in general, to have no deleterious effects on the computation of atmospheric instabilities, eddies, thermal convection, and other large scale flows, nor does the anelastic approximation have an adverse effect on computing Rossby, inertial, internal-gravity, or Poincaré waves. The anelastic approximation has also been used successfully in computing thermal convection and other low-Mach number flows in stars. As discussed in our Conclusions, the anelastic approximation prevents turbulence created by the *z*ombie instability from launching acoustic waves. Because acoustic waves are efficient in transporting momentum and have been considered by many authors as the main mechanism for transporting angular momentum outward in PPDs. the anelastic equations are *n*ot suitable for computing angular momentum transport rates and α in disks, even if they are suitable for computing *z*ombie instabilities.

Boussinesq flows

The Boussinesq equations are another commonly used approximation for vertically stratified flows. These are frequently used as the governing equations for the oceans and for laboratory flows in which there are vertical density stratifications either due to the fluid temperature or salt [Kundu 1990]. The Boussinesq equations are commonly used in the study of laboratory convection [Chandrasekhar 1981] and often for models of convection in stars [Spiegel 1971]. The Boussinesq equations are valid when there is an average density ρ_0 such that for all space and time $\left|\rho(x,y,z,t) - \rho_0\right| \ll \rho_0$. Here, we consider the case where the density variations in the fluid are due only to compositional changes (say, for example the density of salt dissolved in water) and not due to temperature. The Boussinesq equations for disk flow can be obtained from eqs. (4.2) – (4.5) by expanding in powers of $\left|\rho(x,y,z,t) - \rho_0\right|/\rho_0$. For a disk in which the angular velocity of the unperturbed steady equilibrium flow is proportional to R^{-q}, the Boussinesq version of the local Cartesian Euler equation (4.2) in the rotating

frame becomes:

$$\frac{\partial \mathbf{v}}{\partial t} + (\mathbf{v}\cdot\boldsymbol{\nabla})\mathbf{v} = -\boldsymbol{\nabla}\frac{P(x,y,z,t)-\bar{P}(z)}{\rho_0} -$$
$$2\quad\Omega_0\quad \hat{\mathbf{z}}\times\mathbf{v} + 2q\Omega_0^2\, x\,\hat{\mathbf{x}} - \frac{\rho(x,y,z,t)-\bar{\rho}(z)}{\rho_0} g(z)\,\hat{\mathbf{z}}, \tag{4.23}$$

where the steady equilibrium pressure $\bar{P}(z)$ and steady equilibrium density $\bar{\rho}(z)$ satisfy the hydrostatic equation (4.8). The Boussinesq version of the continuity equation (4.3) is

$$\boldsymbol{\nabla}\cdot\mathbf{v} = 0, \tag{4.24}$$

and the Boussinesq version of the fully compressible energy equation (4.4) or anelastic energy equation (4.12) is

$$\frac{\partial \rho(x,y,z,t)}{\partial t} = -(\mathbf{v}\cdot\boldsymbol{\nabla})\rho \tag{4.25}$$
$$= -(\mathbf{v}\cdot\boldsymbol{\nabla})[\rho(x,y,z,t)-\bar{\rho}(z)]$$
$$+ \rho_0 w_z N^2(z)/g(z), \tag{4.26}$$

where the Boussinesq Brunt-Väisälä frequency of the steady equilibrium flow is defined as

$$N(z) = \sqrt{-g(z)(d\bar{\rho}/dz)/\rho_0} \tag{4.27}$$

Equation (4.25) is the diffusionless advection equation for the total density ρ. Due to the fact that this equation has no diffusion, there is a degeneracy in the steady equilibrium thermodynamic solution, and in this Boussinesq case this means that $\bar{\rho}(z)$ is an arbitrary function of z. Notice that the Boussinesq equations (4.23) – (4.24) and (4.26) – (4.27) do not include T and that there is no equation of state. The steady velocity equilibrium solution to these Boussinesq equations is the same as the steady equilibrium solution to the fully compressible equations and to the anelastic equations given by eqs. (4.6) – (4.7) and hydrostatic equilibrium (4.8).

For *c*onstant $N(z) = N_0$ and for *c*onstant gravity $g(z) = g_0$, $\bar{\rho}(z)$ is linear in z, and eq. (4.27) is often used to parameterize the steady equilibrium density:

$$\bar{\rho}(z) = \rho_0(1 - N_0^2 z/g_0). \tag{4.28}$$

In the case of constant gravity and N, the dimensionless Boussinesq equations of motion depend on only two dimensionless numbers: q (which, as in the anelastic equations, is the negative of the shear of the steady equilibrium flow in units of Ω_0), and N_0/Ω_0. As we did with the anelastic equations, we set the two dimensionless numbers that describe the computational domain, L_y/L_x and L_z/L_x equal to unity.

For the case in which $g = 0$, the Brunt-Väisälä frequency N is also equal to zero, $\bar{P}(z) = P_0$ is constant, but $\bar{\rho}(z)$ is still an arbitrary (and dynamically unimportant) function of z.

For the case $g = 0$ and $\bar{\rho}(z) = \rho_0$ is constant, the Boussinesq and anelastic equations become identical.

In most laboratory experiments, the diffusion time of salt is very long compared to any other physically relevant time, so the equations of motion effectively have no diffusion. The degeneracy in $\bar{\rho}(z)$ is frequently exploited in laboratory experiments, and experiments are often initialized with a steady equilibrium in which $\bar{\rho}(z)$ is chosen arbitrarily to suit the experimenter's needs (c.f., Aubert et al. 2012). Note that the inclusion of the tidal acceleration term $2q\Omega_0^2\, x\, \hat{\mathbf{x}}$ in eq.(4.23) is somewhat misleading because the equation can be re-written without it by defining the pressure head $\Pi \equiv [P(x,y,z,t) - \bar{P}(z)]/\rho_0 - q\Omega_0^2\, x^2$ as

$$\begin{aligned} \frac{\partial \mathbf{v}}{\partial t} + (\mathbf{v}\cdot\boldsymbol{\nabla})\mathbf{v} = & - \boldsymbol{\nabla}\Pi - 2\Omega_0\, \hat{\mathbf{z}} \times \mathbf{v} \\ & - \frac{\rho(x,y,z,t) - \bar{\rho}(z)}{\rho_0} g(z)\, \hat{\mathbf{z}}, \end{aligned} \tag{4.29}$$

indicating that dropping the tidal acceleration does not effect the velocity $\mathbf{v}$ (but it does change the value of the pressure P). Thus, the Boussinesq equations (4.24) and (4.26) – (4.29) govern the velocity and density of rotating, salt-stratified laboratory flows in which the rotation axis, gravity and the equilibrium density gradients are aligned in the z direction and in flows in which viscosity and salt diffusion can be ignored. Those flows include channel flows or unbounded flows in which the unperturbed equilibrium is $\bar{v}_x = \bar{v}_z = 0$ and $\bar{v}_y(x)$ is an arbitrary function of x. An example of the latter is plane Couette flow, for which $\bar{v}_y(x) \equiv q\Omega_0 x$ is a linear function of x, and thus the Boussinesq equations that govern plane Couette flow are the same as those that govern Boussinesq disk flow. Unbounded, rotating plane Couette flows with constant Brunt-Väisälä frequency N_0 make up a two-parameter family of flows, with dimensionless parameters q and N_0/Ω_0. These plane Couette flows are all thought to be linearly *n*eutrally stable meaning that if the equations are linearized about the steady equilibrium Couette flow in hydrostatic equilibrium the eigenmodes neither grow nor decay exponentially in time.

4.3 Evidence of Instability in Protoplanetary Disks and Channels with Vertical Gravity

Temporal growth and decay of an initial energy fluctuation

One of the most cited pieces of evidence that protoplanetary disks are stable to purely hydrodynamic instabilities is given by Figure 1 in BHS96, which we reproduce below. This figure shows the growth/decay of the kinetic energy fluctuations of the flow as a function of time and q, where q is defined in eq. (4.1) and where the kinetic energy fluctuations is defined as $[\mathbf{v}(x,y,z,t) - \bar{v}_y\, \hat{\mathbf{y}}]^2/2$, where $\bar{v}_y\, \hat{\mathbf{y}}$ is the steady equilibrium flow in eq. (4.7). For $q = 3/2$, the energy fluctuation would be the non-Keplerian component of the flow. The initial-value calculation that produced Figure 4.1 used the fully compressible equations (4.2)

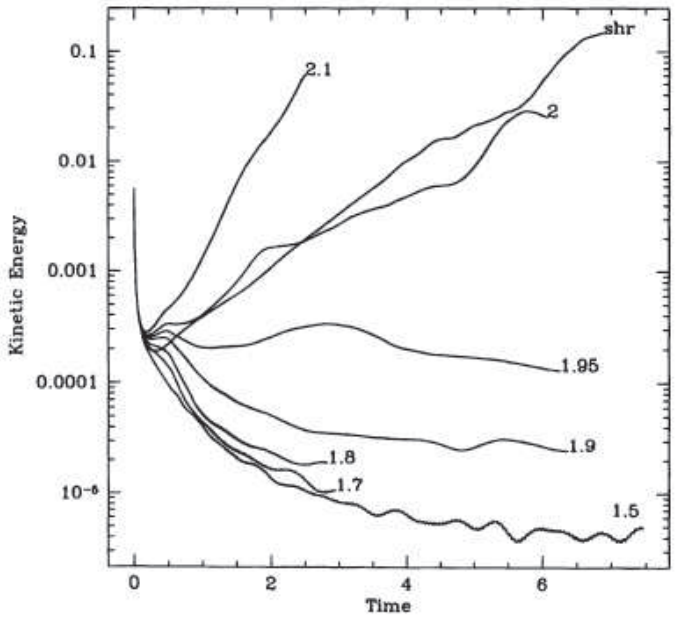

Figure 4.1: This is Figure 1 from BHS96, which shows the temporal evolution of the fluctuation kinetic energy per unit mass, defined in § 4.3, where time is in units of "years" $(2\pi/\Omega_0)$ and the kinetic energy per unit mass is in units of $(L_x\Omega_0)^2$. The time evolutions are for different values of q as defined by eq. (4.1). These are fully-compressible simulations with $g = 0$, $N = 0$, $\gamma = 5/3$. The size of the computational domain is $L_x = L_y = L_z$. The numerical code was ZEUS with a spatial grid of 64^3 points. The initial fluctuation kinetic energy per unit mass is $KE_0 = 5.9\times10^{-3}$, corresponding to an initial fluctuation rms velocity of $\sim\ 0.1(\Omega_0 L_x)$. The initial spectrum of the noise was homogeneous, isotropic, and Gaussian in wavenumber k. The initial unperturbed equilibrium flow had uniform pressure, density, and temperature. The curve labeled with "shr" in Figure 4.1 corresponds to the case with $q = 3/2$ and with the Coriolis and tidal acceleration terms dropped from eq. (4.2) The growth and decay of the fluctuation kinetic energy as a function of q supports Rayleigh's theorem that the flow is stable for $q < 2$ for $f$lows with constant density.

– (4.5) starting with the steady equilibrium flow in eqs. (4.6) – (4.8) perturbed with small-amplitude noise. The initial value of the noise's rms velocity was $\sim\ 0.1\ L_x\,\Omega_0$. The gravity g was set equal to zero in this problem and the values of steady equilibrium temperature, density and pressure were all chosen to be constants; $\bar{T}(z) = T_0$; $\bar{\rho}(z) = \rho_0$; $\bar{P}(z) = P_0$. The equations were solved with periodic boundary conditions in y and z and shearing box boundaries in y [Goldreich and Lynden-Bell 1965; Marcus and Press 1977].

Because the energy fluctuations all increase in time for $q \geq 2$ and decrease in time for $q < 2$, Figure 4.1 is used to support the hypothesis that the flow is stable (unstable) to all perturbations when the angular momentum per unit mass of the flow, $R^2\,\Omega(R) \propto R^{(2-q)}$,

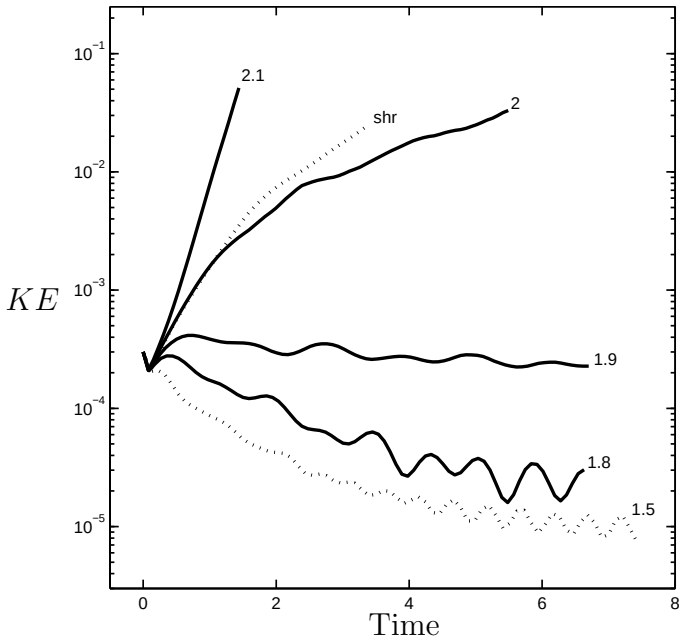

Figure 4.2: Time evolution of the fluctuation kinetic energy per unit mass with different q as in Figure 4.1 and with the same parameter values and units as in Figure 4.1, but using the anelastic equations, which are identical to the Boussinesq equations when $g \equiv 0$, as is the case here. Unlike the flows in Figure 4.1, the flows here were initialized with a smaller energy fluctuation (see text for details) of 3×10^{-4} (which is the value of the energy that all of the curves in Figure 4.1 plummet to almost immediately). The initial 3D spectrum of the energy fluctuations used in this figure was homogeneous and isotropic, but unlike the initialization in Figure 4.1, was Kolmogorov, rather than Gaussian (see § 4 for details). The Boussinesq/anelastic simulations used $g = 0$, $N = 0$. The spatial resolution of the spectral calculations used 128^3 Fourier modes. The stability of the anelastic and computed flows as a function of q are the same as shown in Figure 4.1.

increases (decreases) in the radially outward direction. This hypothesis is consistent with the Rayleigh's centrifugal stability theorem; however, it must be noted that Rayleigh's theorem was proved only for the case of constant density fluids [Rayleigh, Lord 1916] and therefore may not be applicable to astrophysical flows in disks. The curve labeled with "shr" in Figure 4.1 corresponds to the case with $q = 3/2$ and with the Coriolis and tidal acceleration terms dropped from eq. (4.2), which would be appropriate for fully compressible flow in a channel with cross-stream shear, but no rotation. We have reproduced Figure 4.1 using the ATHENA code.

Figure 4.2 shows a nearly identical set curves as those in Figure 4.1, but in Figure 4.2, the flow is computed with a spectral numerical code (BM06) using the anelastic equations (4.10) – (4.14). Similar boundary conditions were used as were used in Figure 4.1, and the flow

was initialized as in Figure 4.1 with noise added to the steady equilibrium flow in eqs. (4.6) – (4.8). (See Section 4 for details of the initial noise.) The initial value of the noise's rms velocity in Figure 4.2 is $\sim\ 0.04\ L_x\,\Omega_0$, or equivalently, with an initial average kinetic energy per unit mass (see caption for definition) in the fluctuations of $3.0\times10^{-4}\ (L_x\,\Omega_0)^2$. We chose the energy in the initial fluctuation to be smaller than that in Figure 4.1; there is an initial precipitous decay in the fluctuating energy for all of the curves in Figure 4.1 from its initial value of $5.9\times10^{-3}\ (L_x\,\Omega_0)^2$ to the smaller value of $\sim\ 3.0\times10^{-4}\ (\ L_x\,\Omega_0)^2$, which is the value that we initialized the fluctuating energies to in Figure 4.2. As in Figure 4.1, the flows in Figure 4.2 were computed with the gravity $g=0$ and $\bar{T}(z)=T_0$; $\bar{\rho}(z)=\rho_0$; $\bar{P}(z)=P_0$. We remind the reader that the Boussinesq and anelastic equations become identical when $g=0$ and $\bar{T}(z)=T_0$; $\bar{\rho}(z)=\rho_0$; $\bar{P}(z)=P_0$, so Figure 4.2 would be the same if we had used the Boussinesq rather than the anelastic equations.

Figure 4.3 is similar to Figure 4.1 and Figure 4.2, but the three curves shown here are all for the Keplerian case with $q=3/2$. The broken black curve is the same as the curve in Figure 4.2 for $q=3/2$, but plotted for a much longer time. The blue solid curve is computed with the anelastic equations (4.10) – (4.14). The black curve is computed with the Boussinesq equations (4.24) – (4.27). The blue and black curves are both computed using the same boundary and initial conditions as in Figure 4.2*b*ut with one important difference. In Figure 4.3, the blue and black curves were computed with $g=g_0\neq0$ and $N=N_0\neq0$. The initial steady flow for the stratified anelastic calculation constant $N_0/\Omega_0=2$ (or, equivalently, $\beta=10$) with $\bar{P}$ and $\bar{\rho}$ given by eqs. (4.18) and (4.19), has $\bar{T}=T_0$, and pressure scale height $H=L_x$. For the Boussinesq flow, $N_0/\Omega_0=2$, and $\bar{\rho}$ is given by eq.(4.28). To emphasize instability of the flows with non-zero gravity and with non-zero initial vertical density stratification (i.e., $d\bar{\rho}(z)dz\neq0$), we initialized both flows in Figure 3 with a small perturbing fluctuation kinetic energy. It is $9.2\times10^{-5}\ (L_x\,\Omega_0)^2$, approximately $1/64^{th}$ used in Figure 1 by BHS96. (See the next section for how small we can make the initial kinetic fluctuation and still make the flow go unstable.)

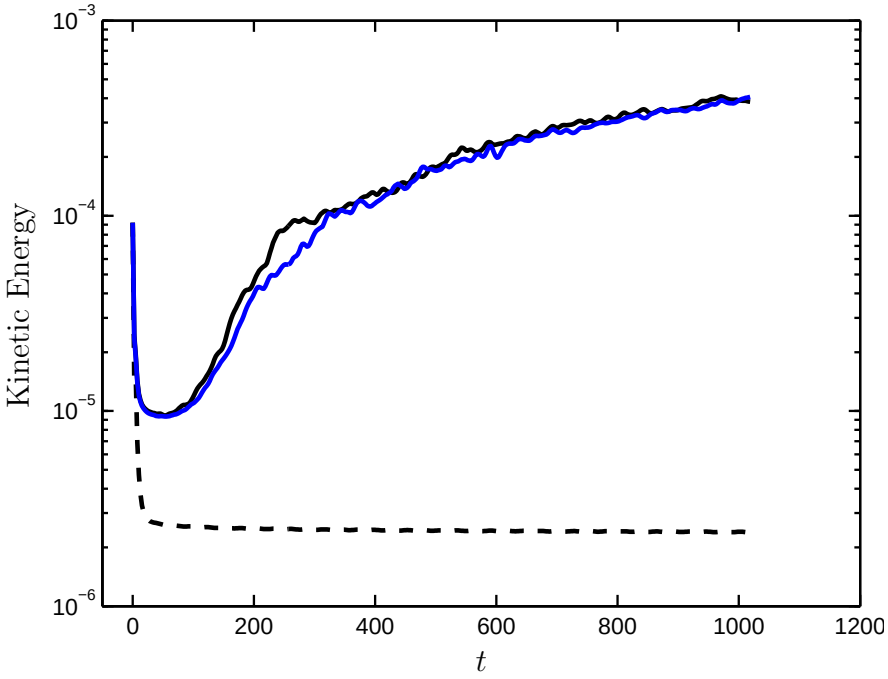

Figure 4.3: Time evolution of the fluctuation kinetic energy per unit mass (which in this case is the non-Keplerian kinetic energy) for anelastic and Boussinesq flows for $q \equiv 3//2$. Blue solid line - anelastic calculation with vertical density stratification. Black solid line – Boussinesq with vertical density stratification. Black dash line - Boussinesq/anelastic flow with $g = 0$ and $N = 0$, which is the same calculation as shown in Figure 4.2 labeled with "1.5", but integrated for a much longer time. The figure shows that with vertical density stratification, flows with $q = 3/2$ are unstable. In the two density stratified simulations, we set $H = L_x = L_y = L_z$ and $N_0/\Omega_0 = 2$ or $\beta = 10$. Note that the Brunt-Väisälä frequencies, gravity are spatially uniform in the stratified flow. The spatial resolution is 256^3 Fourier modes. To guide the eye, and to remove fast oscillations in the energy that are due to the shearing box boundary conditions, the due energies in this figure and in Figure are moving-averages-in-time, with a window size of 10 yrs. The anelastic simulation has an initial rms Mach number $Ma_0 = 4.3 \times 10^{-3}$ based on the isothermal sound speed. The initial anelastic flows are isothermal, and all three flows were initially perturbed with Kolmogorov noise as in Figure 4.2 with an initial fluctuation kinetic energy of 9.2×10^{-5} (see Figure 4.1 for units), which is 1/64 of the initial fluctuation kinetic energy used in Figure 4.1. The time evolution of kinetic energy can be divided into 3 parts. The first part is from $t = 0 \sim 50\ yr$, in which the flow adjusts from the initial condition with most of the initial vorticity destroyed by hyper-viscosity. This causes the initial fast decrease in the fluctuation kinetic energy. After the time that the fluctuation kinetic energy reaches its minimum to $t =\sim 250\ yr$, the fluctuation kinetic energy increases approximately exponentially. During this time, the critical layers are strongly excited (see § 5), turn into vortex layers, and roll-up into $z$ombie vortices. In third part, from $t = 250\ yr$ onward, the fluctuation energy growth is slower as the flow reaches a statistically steady equilibrium. The fluctuation kinetic energy asymptotes at late times to a value of $\sim 3 \times 10^{-4}$.

The dashed curve in Figure 4.3 shows the fluctuating or non-Keplerian energy per unit mass as a function of time using the same parameters values, boundary conditions, and initial conditions as the anelastic flow in Figure 4.3 (with the exception that the initial fluctuating non-Keplerian energy is approximately two times larger). Also plotted in Figure 4 is the fluctuating energy per unit mass of the same flow, but computed with the fully compressible equations (4.2) – (4.5) using ATHENA, rather than the anelastic equations. Figure 4.3 also differs from Figure 4.2 and Figure 4.3 in that the flows are integrated forward in time for only 200 years rather than 1200 years because ATHENA is much more computer resource intensive than the spectral codes. None the less, Figure 4.3 clear shows that the full compressible flow with $q = 3/2$ is also unstable. In fact for the first 200 years, the compressible flow grows faster than the anelastic flow. This is due to the vertical boundary conditions used in the anelastic spectral code, which are highly dissipative. At late times, i.e., at 1000 yrs the non-Keplerian fluctuating energy of the flow anelastic flow in Figure 4.3 is approximately the same as the late-time anelastic flow in Figure 4.3. The fact that the late-time anelastic flows in Figure 4.3 and Figure 4.3 are similar despite the fact that they were initialized with different magnitude perturbation is one of many numerical indications that after a flow goes unstable to the zombie instability, it evolves to an attracting turbulent solution whose gross properties are independent of the details of the initial conditions.

The vertical vorticity of the zombie instability

The growth of the non-Keplerian kinetic energies in Figure 4.3 and Figure 4.3 is evidence of instability, but spatial plots of the relative vorticity of the flow, defined as $\boldsymbol{\omega} \equiv \boldsymbol{\nabla} \times (\mathbf{v} - \bar{\mathbf{v}}) = \boldsymbol{\nabla} \times \mathbf{v} + q\,\Omega_0\,\hat{\mathbf{z}}$ are more useful in illustrating the zombie instability's strength and ubiquitousness throughout the computational domain. In particular, the point-wise Rossby number, defined in terms of the relative vertical vorticity as $Ro(x, y, z, t) \equiv [\hat{\mathbf{z}} \cdot \boldsymbol{\omega}(x, y, z, t)]/(2\Omega_0)$ will be shown in § 4 and § 5 to be much more indicative of the zombie instability than, say, the Mach number, because the threshold for instability depends on Ro, and the late-time zombie turbulence has a characteristic $|Ro|$ of 0.25, regardless of the values of the parameters of the flow such as q, β, H/L_x, and γ. The nature of the zombie instability is best shown in plots of $Ro(x, y, z, t)$ as functions of time and space when the initial perturbation of the steady equilibrium flow $\bar{\mathbf{v}}$ is a single, isolated vortex. However, that type of perturbation is not relevant to protoplanetary disks, so we defer a study of those types of perturbations to § 5. The focus of this section is to show how $Ro(x, y, z, t)$ develops in a Keplerian flow ($q = 3/2$) when the initial perturbation is Kolmogorov noise. Even with an initial perturbation of noise, plots of $Ro(x, y, z,)$ reveal some of the more salient features of the zombie instability.

Figure 4.5 show $Ro(x, y, z, t)$ for an anelastic flow in the x–z plane at four different times and at an arbitrary stream-wise location in y. (Because the equations, boundary conditions and initial conditions are invariant under translation in y, the flow in all x–z planes is statistically the same for all time.) Figure 4.6 shows $Ro(x, y, z, t)$ in the x–y plane for the same flow at $z = 0$, which is midway between the upper and lower boundaries.

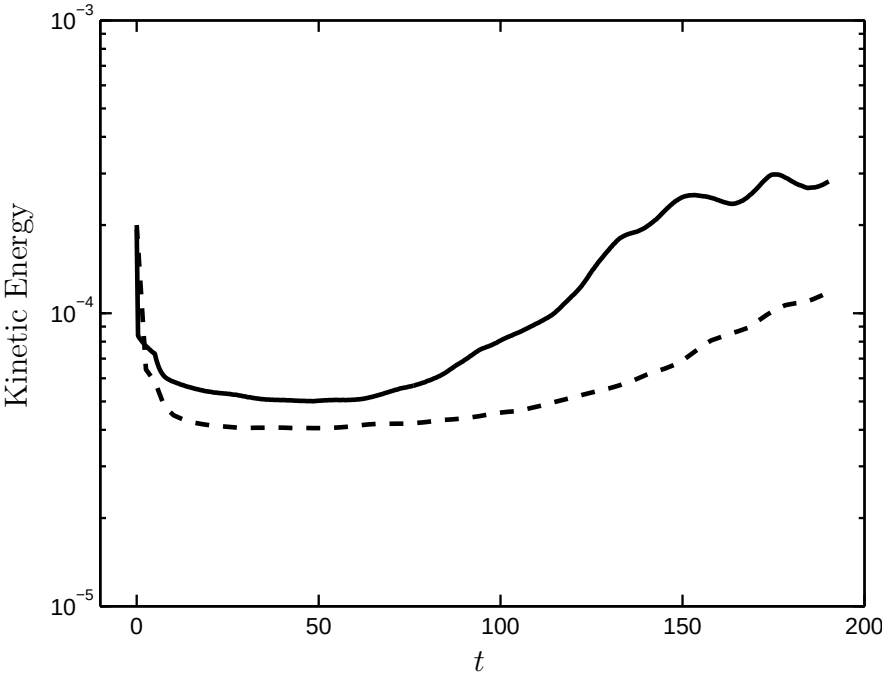

Figure 4.4: As in Figure 4.3 with $\beta = 10$, but with both of the plotted flows having an initial fluctuating energy per unit mass of 1.9×10^{-4}, which is approximately twice that of the blue curve in Figure 4.3, and both flows have $\beta = 10$. The dashed curve is computed with the anelastic equations, and the solid curve computed with the fully compressible equations using ATHENA. The reason why the anelastic kinetic energy is relatively small is due to the anelastic code's vertical boundary damping.

The parameter values, initial conditions and boundary conditions of the flow in Figure 4.5 and Figure 4.6 are identical to the stratified anelastic flow shown in Figure 4.3 with the exception that $N_0/\Omega_0 = 1$, rather than 2, or, equivalently, with $\beta = 2.5$, rather than 10. Note that the initial perturbing velocity has a Kolmogorov energy spectrum in which the velocity phases are random, so there are no coherent features of any kind in the initial flow. As discussed in § 4.1, the relative vorticity field $\boldsymbol{\omega}(x, y, z, t)$ and $Ro(x, y, z, t)$ of Kolmogorov noise is dominated by the Fourier modes with the smallest length scales, so Figure 4.5a and Figure 4.6a are dominated by the smallest scales, and in fact, the sizes of the patches in the panels are equal to the spatial resolution of the calculation, which is $L_x/256$ in each direction. Figure 4.5a and Figure 4.6a look the same because the initial perturbation of noise is homogeneous and isotropic. Very quickly after $t = 0$, much of the initial vorticity in Figure 4.5a and Figure 4.6a is destroyed by the numerical code's hyper-viscosity, which is largest at the smallest length scales in the numerical calculations. By time $t = 2.5\ yrs$ (Figure 4.5b and Figure 4.6b) most of the surviving initial vorticity has inverse-cascaded to larger length scales and the initial $\bar{\mathbf{v}}$ has smeared out the vorticity in the stream-wise y direction to form elongated vortical structures. At time $t = 2.5\ yrs$, the asymmetry between

cyclonic and anticyclonic vorticity ω_z – one of the signatures of the zombie instability – is apparent. Relative vorticity is defined as cyclonic [anticyclonic] when ω_z and Ω_0 have the same [opposite] signs, or equivalently, when $Ro(x, y, z, t) > 0$ [$Ro(x, y, z, t) < 0$]. In all of the figures in this paper, cyclonic [anticyclonic] vorticity is shown as red [blue] in color-plots and as white [black] in grey-scale plots. As we shall elaborate in § 5, "stripes" or layers of cyclonic vorticity aligned in the stream-wise direction are linearly stable. In contrast, stripes or layers of anticyclonic vorticity aligned in the stream-wise direction are linearly unstable; the anticyclonic vortex layers roll-up into stable anticyclonic vortices. The instability of the anticyclonic vortex layers is primarily cause of the cyclone/anticyclone asymmetry in Figures 5 and 6.

By 50.9 yrs, the zombie instability is well underway. As shown in § 5, one of the first signatures of the instability is the excitation of critical layers (defined and reviewed in § 5) and their accompanying dipolar vortex layers, which are easily identified because they occur as a pair of "stripes" in the x-y plane with a layer of cyclonic relative vorticity immediately adjacent to a layer of anticyclonic relative vorticity. A dipolar vortex layer aligned in the stream-wise direction can be seen in Figure 4.6c at $x = 0.44/L_x$. It is unusual, especially with initial perturbation consisting of noise, to find dipolar vortex layers at late times due to the fast instability of the anticyclonic component of the dipolar layer. At the time of Figure 4.6c, the critical layer at $x = 0.44/L_x$ has only just recently been excited and formed a dipolar vortex layer. Shortly after the time shown in Figure 4.6c, the anticyclonic part of the dipolar vortex layer became unstable and rolled up into an anticyclonic vortex. (See § 5.) At late times, $t = 1370$ yrs in Figure 4.5d and Figure 4.6d, the flow has reached a statistically steady state of zombie turbulence. Here the flow has formed a pattern that appears to have cross-stream or x wavenumber of 6 or 7. This pattern is especially clear in Figure 4.6d. The relative vorticity, although very turbulent, has developed some spatial coherence. The cyclonic vorticity has formed approximately 2D layers that are approximately aligned in the y-z planes. Between these planes are approximately ellipsoidally-shaped turbulent anticyclones. The aspect ratio χ (defined as the stream-wise diameter of an anticyclone in the y direction divided by its cross-stream diameter in x) is approximately the same as the laminar vortices studied by [Moore and Saffman 1971].

$$-\frac{\omega_z}{q\,\Omega_0} \equiv \frac{-2Ro}{q} = \frac{\chi+1}{\chi-1}\frac{1}{\chi} \tag{4.30}$$

The Moore-Saffman relation was derived for a two-dimensional vortex with uniform relative vorticity embedded in flow with uniform shear. Many vortices have aspect ratios similar to that in eq. (4.30) because the relation is the quantification of the fact that a large relative vorticity tends to make a vortex "round" and a large background shear tends to elongate a vortex is its stream-wise direction. In Figure 4.6d, the approximate vorticity of the vortex is ω_z and the background shear is $(-q\,\Omega_0)$. Note that because at late times the characteristic magnitude of Ro of the anticyclones in $z$ombie turbulence is always $\sim$ -0.25, regardless of the parameters of the flow, and because $q = 3/2$ for a Keplerian disk, the aspect ratios χ of all of the $z$ombie vortices in all of our calculations, regardless of the values of β and H/L_x,

are the same and between 4 and 5, consistent with the Moore-Saffman relation. The general vortex patterns in Figure 4.5d and Figure 4.6d with a quasi-periodicity in the x direction is a signature of zombie turbulence and the periodicity's wavenumber is a predictable property of the flow and derived in § 5. Figure 4.5d and Figure 4.6d are highly turbulent, but the magnitudes of the Rossby numbers of the anticyclonic vortices and cyclonic layers persist indefinitely. We have carried out several sets of initial-value calculations in which zombie turbulence is created in fully compressible flows (Figure 4.7), anelastic, and Boussinesq for a wide variety of parameters and the $Ro(x, y, z, t)$ of the late-time flows always look like Figure 4.5d and Figure 4.6d.

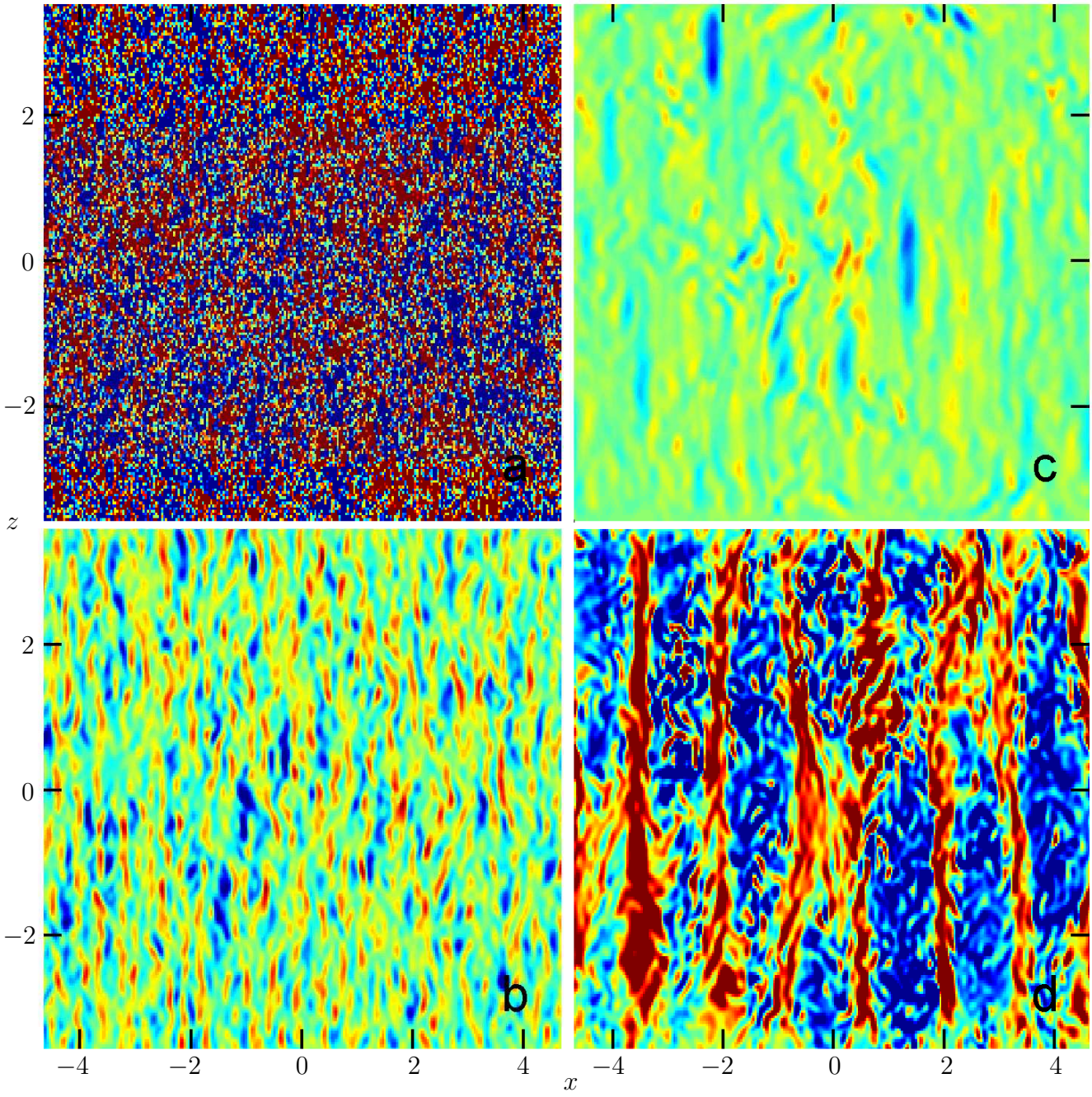

Figure 4.5: figure 5 caption see next page

caption for Figure 4.5 Time evolution of point-wise Rossby number $Ro(x, y, z, t)$ in the $x - z$ plane. The figure has been cropped in the z direction so it does not show the damping regions at the vertical boundaries. The unperturbed anelastic flow has $q = 3/2$ and $N_0/\Omega_0 = 1$, or $\beta = 2.5$. The initial noise has a Kolmogorov ($k^{-5/3}$) spectrum, and the initial fluctuation kinetic energy is 9×10^{-5}. The color-map ranges from -0.25 to 0.25, with blue [red] for anticyclones [cyclones] with $Ro < 0$ [$Ro < 0$]. Green corresponds to $Ro = 0$. (In grey-scale plots, the blackest pixels have $Ro = -0.25$ and whitest have $Ro = 0.25$.) Left column $x - z$ (radial-vertical) plane at $y = 0$. a) $t = 0yr$. Relative vorticity dominated by the smallest lengthscale, so the image is pixelated at the resolution length. The color and grey scales are over-saturated in this panel with the minimum Ro of this initial condition being 2.3 and maximum being 2.4. b) $t = 2.5yrs$. Decay of much of the initial relative vorticity and stretching in the stream-wise direction by the Keplerian shear. c) $t = 50.9yrs$. Inverse cascading to large scales and asymmetry between cyclonic and anticyclonic relative vorticity. d) $t = 1370.0\ yrs$. Zombie turbulence with zombie vortices filling up the whole domain with $Ro \simeq -0.3$. The near spatial periodicity, here with wavenumber between 6 and 7, of the turbulent flow in the x direction is one of the signatures that makes $z$ombie turbulence easy to identify.

Space-filling properties of the zombie turbulence

Figure 4.8 – Figure 4.10 show how the rms Mach numbers (based on the isothermal sound speed) $Ma_{rms}(t)$ and rms Rossby numbers $Ro_{rms}(t)$ evolve in time for three anelastic flows. For all three flows the values of $Ma_{rms}(t)$ and rms Rossby numbers $Ro_{rms}(t)$ initially plummet due to the dissipation, but then grow after the zombie instability sets in. All of our calculations with zombie turbulence have late-time values of $Ro_{rms}(t)$ between 0.2 and 0.3. A comparison of Figure 4.9 and Figure 4.10, for which the flows have the same values of β (or N_0/Ω_0), γ, H/L_x and q, but have different initial conditions, shows that the statistical properties of the late-time flows are independent of the intimal conditions.

To understand how the rms Mach $Ma_{rms}(t)$ and Rossby $Ro_{rms}(t)$ numbers evolve at late times, it is first necessary to show that their values are not independent. The rms Rossby number is approximately

$$Ro_{rms} \simeq v_{eddy}(L_\omega)/(L_\omega\,\Omega_0), \tag{4.31}$$

where L_ω is the characteristic length scale in the flow where the vorticity has its maximum value and $v_{eddy}(L)$ is the characteristic velocity of a turbulent eddy of diameter L (rigorously defined in § 4.1). The rms Mach number is approximately

$$\begin{aligned} Ma_{rms} &\simeq v_{eddy}(L_v)/C_s = v_{eddy}(L_v)/(\beta^{1/2} H\Omega_0) \\ &= Ro_{rms}\,\beta^{-1/2}\,\frac{v_{eddy}(L_v)}{v_{eddy}(L_\omega)}\,\frac{L_\omega}{L_x}\,\frac{L_x}{H}, \end{aligned} \tag{4.32}$$

where we used eq. (4.21). For the flow in Figure 4.8 with $\beta = 2.5$, $(L_x/H) = 1$, with $(L_x/L_\omega) \simeq 9$ (i.e., where there are quasi-periodicity in the x direction has wavenumber 9), and with $v_{eddy}(L_v) \simeq v_{eddy}(L_\omega)$ (which is obtained by assuming that at late times the energy, as well as the enstrophy, are dominated by the length scales that are approximately equal to the radii of the late-time coherent vortices), we see that $Ma_{rms} \simeq 0.07\,Ro_{rms}$, which is consistent between Figure 4.8*a* and Figure 4.8*b*. For the flows in Figure 4.9 and Figure 4.10, with $\beta = 10$, $(L_x/H) = 1$, and with $(L_x/L_\omega) \simeq 6$, we see that $Ma_{rms} \simeq 0.045\,Ro_{rms}$, which is consistent between Figure 4.9*a* and Figure 4.9*b*, and between Figure 4.10*a* and Figure 4.10*b*.

The fact that Figure 4.9 and Figure 4.10 show that the values of $Ro_{rms}(t)$ have plateaued at late times, but that the values of $Ma_{rms}(t)$ suggests that the flow has not yet reached a statistically steady state. However, eq. (4.32) implies that the only way in which $Ma_{rms}(t)$ can grow while keeping $Ro_{rms}(t)$ fixed is if $v_{eddy}(L_v)/v_{eddy}(L_\omega)$ is still growing, and the latter is indicative that the inverse cascade of energy is still continuing at late times in the flows in Figure 4.9 and Figure 4.10.

Of special importance to flows in protoplanetary disks in which the steady equilibrium vertical temperature is independent of height z, so that the gravity $g(z)$ is linear in z and $\beta \equiv 1$ (see eqs. (4.17) and (4.21)), is that eq.(4.32) shows that at late times $Ma_{rms} = Ro_{rms}\,[v_{eddy}(L_v)/v_{eddy}(L_\omega)]\,L_\omega/H$. If, as we argue in the Conclusion and that other have argued independently, that the turbulent flow in a disk inverse cascades until the length scale of the vortices is equal to H, then

$$Ma_{rms} \simeq Ro_{rms}, \tag{4.33}$$

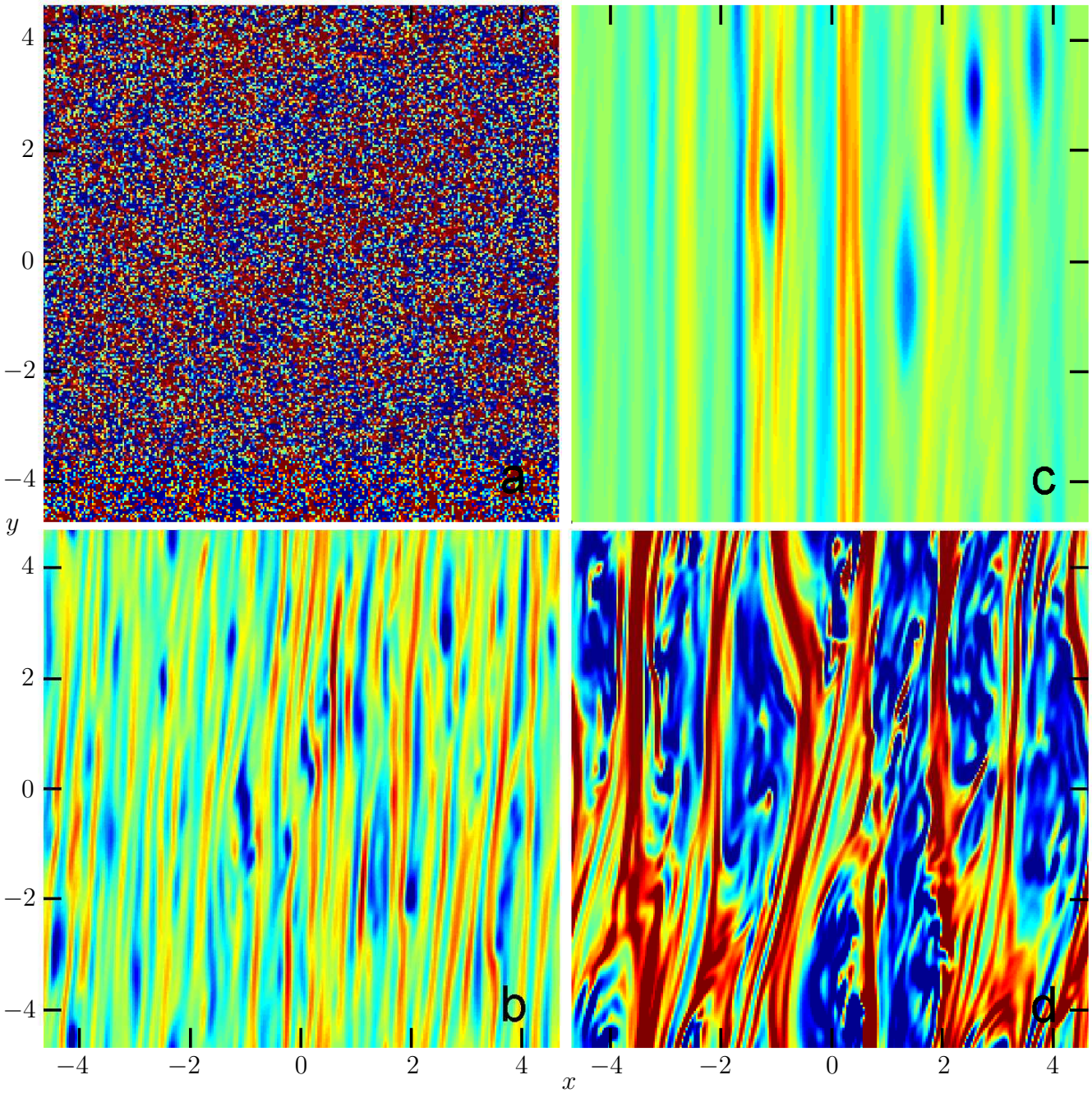

Figure 4.6: Same as Figure 5 but in the x-y plane at $z = 0$. Panel **a** looks like Figure 5**a** because the initial noise is isotropic and homogeneous.

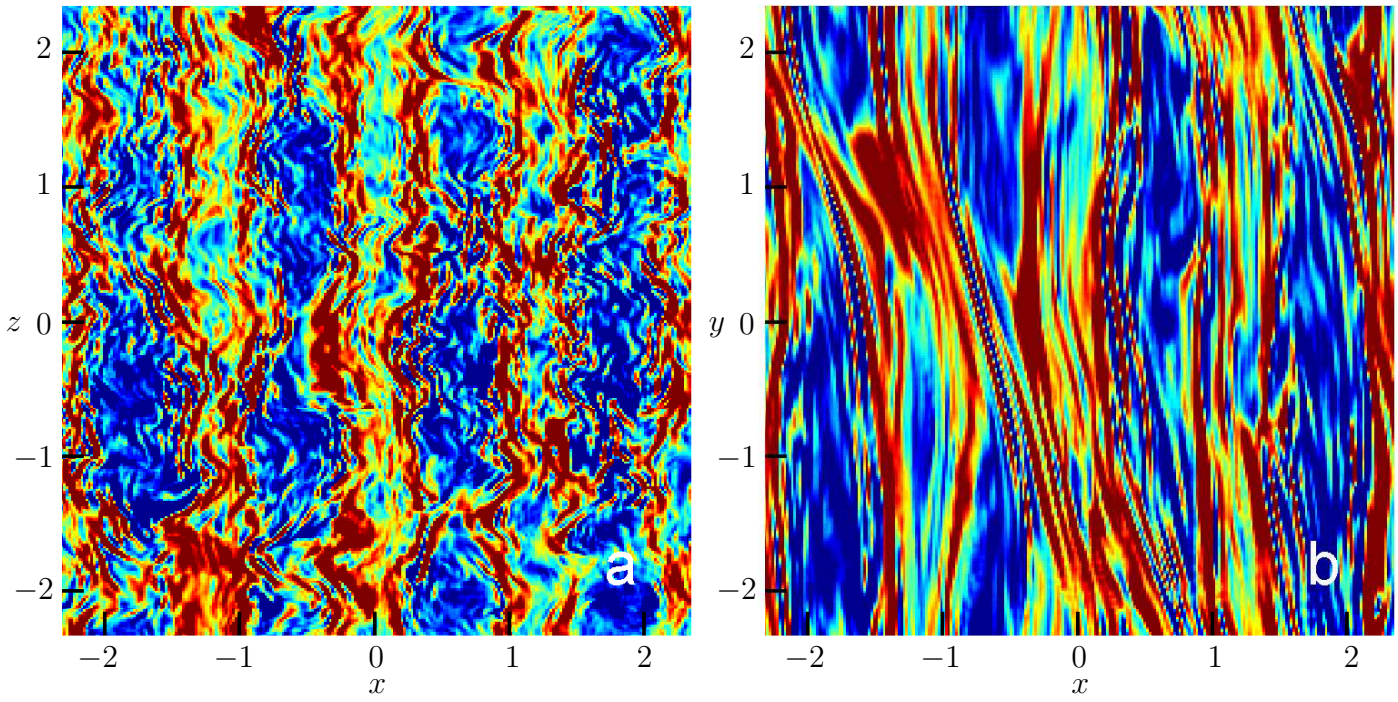

Figure 4.7: a) As in Figure 4.5d, b) as in Figure 4.6d, but for the flow computed with the fully compressible equations using ATHENA in Figure 4.3 with an initial fluctuation kinetic energy per unit mass of 1.9×10^{-4}, $\beta = 10$, or equivalently, with $N_0/\Omega_0 = 2$. No damping at the vertical boundaries is used in this simulation. The flow is shown at $t = 190\ yrs$. Although the zombie instability is well underway, the turbulence is not fully developed. The pattern is still evolving and the fluctuation kinetic energy is still growing.

which would have a profound effect on the rate of angular momentum transport in a disk.

Figure 11 demonstrates that the zombie fills the computational domain at late times and is not confined to a few spatial locations. This property was illustrated in Figure 4.5d, Figure 4.6d, and Figure 4.7. We quantify the space-filling property by defining a spatial filling factor for the turbulent vorticity: $f_{Ro}(\delta, t)$ is defined to be the volume fraction of the computational domain that has $|Ro(x, y, z, t)| \geq \delta$. We further quantify the space-filling property by defining a spatial filling factor for the turbulent velocity: $f_{Ma}(\delta, t)$ is defined to be the volume fraction of the computational domain that has $Ma(x, y, z, t) \geq \delta$. Figure 4.11 shows that for the anelastic flow in Figure 4.3 and Figure 4.9 that approximately 10 % of the flow is filled with vortices with Rossby numbers with magnitudes greater than 0.3; 30 % with magnitudes greater than 0.2; and almost 60 % with magnitudes greater than 0.1. Figure 4.12 demonstrates the space-filling property of the turbulent velocity in terms of $f_{Ma}(\delta, t)$. The filling factors in Figure 4.11 and Figure 4.12 are representative of all of our anelastic calculations.

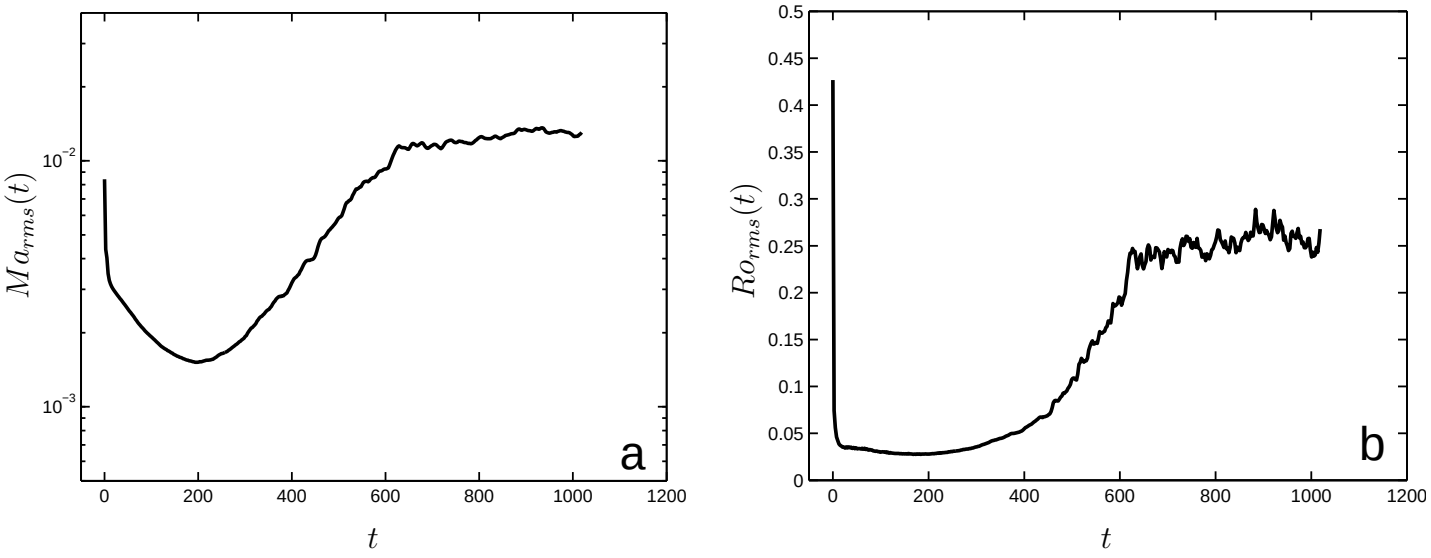

Figure 4.8: Time evolution of the rms Mach number (based on the isothermal sound speed) $Ma_{rms}(t)$ (panel **a**) and $Ro_{rms}(t)$ (panel **b**) for the anelastic flow in Figure 4.5 and Figure 4.6 with an initial fluctuation kinetic energy per unit mass of 9×10^{-5}, $N_0/\Omega_0 = 1$ or $\beta = 2.5$. The initial rms velocity is $v_{rms} = 0.0136(\Omega_0 L_x)$, which is $1/8^{th}$ of the value of the flows in Figure 4.1. The initial rms Mach numbers and Rossby numbers are 8.6×10^{-3} and $Ro_{rms} = 0.4267$, respectively. Both values rapidly plummet due to the dissipation, but grow after the zombie instability sets in and eventually plateau. All of our calculations with zombie turbulence have late-time values of $Ro_{rms}(t)$ between 0.2 and 0.3 At late times, the value of $Ma_{rms}(t)$ is slaved to the value of $Ro_{rms}(t)$ – § 3.3 for details.

4.4 Threshold for finite amplitude instability

Initial Perturbations: coherent vortices and random noise

Our first study of the zombie instability (MPJH13) was focussed on initial perturbations of steady equilibrium flows perturbed by a single vortex, and it determined that the instability was not linear, but required a finite amplitude to trigger it. We found that that the amplitude of the perturbing vortex was set by its vorticity or Rossby number, rather than its velocity. For Boussinesq flows with $q = 3/2$, the necessary initial $|Ro|$ was ~ 0.3. Here, to be relevant to protoplanetary disks, we examine the amplitude of three-dimensional noise that is needed to trigger the zombie instability in anelastic flows with $q = 3/2$. We designed three sets of numerical experiments to determine whether the necessary amplitude of the initial noise to trigger instability depended upon its Rossby number, Mach number, energy or some other property of the noise.

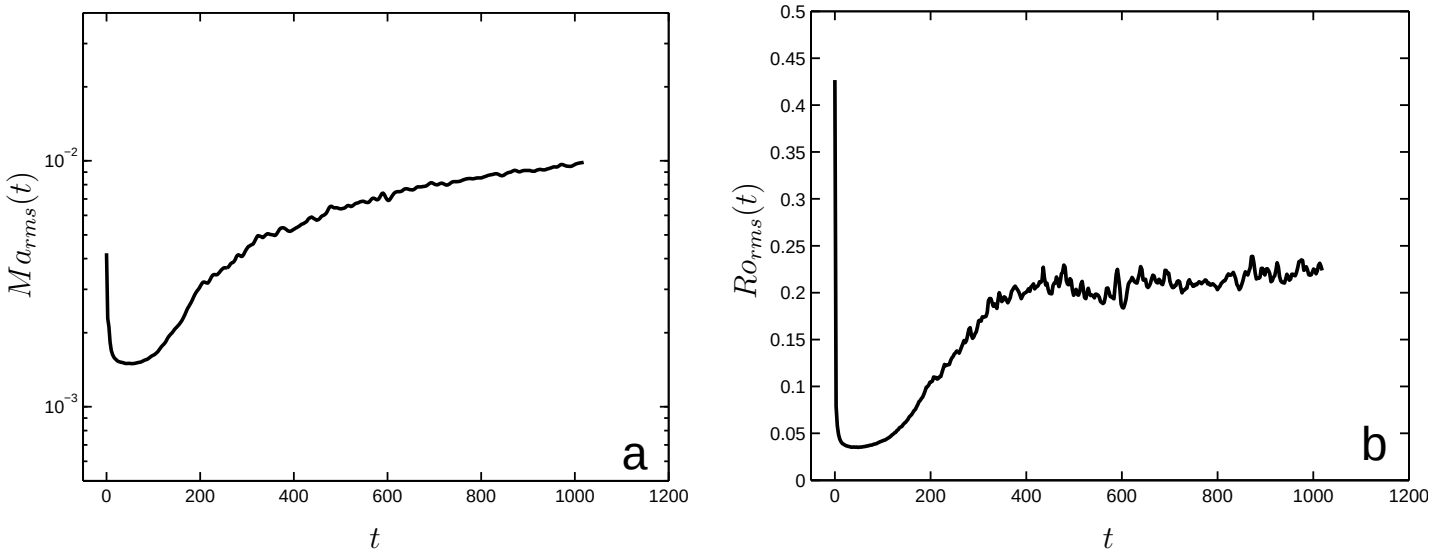

Figure 4.9: Time evolution of Ma_{rms} and Ro_{rms} as plotted in Figure 4.8, but for the anelastic flow in Figure 4.3 so this flow has the same initial fluctuation kinetic energy per unit mass of 9×10^{-5} as the flow in Figure 4.9 but $\beta = 10$ rather than 2.5 (or $N_0/\Omega_0 = 2$, rather than unity). The initial rms Mach and Rossby numbers are 4.3×10^{-3} and 0.4267, respectively. The late-time Ro_{rms} is slightly smaller than that in Figure 4.8. The flow at $t = 100\ yrs$ is not yet in equilibrium as indicated by the fact that $Ma_{rms}(t)$ is still increasing at that time. However, the fact that $Ro_{rms}(t)$ has reached a plateau at that time shows that the inverse cascade of energy is still active.

Review of Turbulent spectra, eddy velocities, eddy vorticities, and Fourier modes

To help understand the analysis of the instability created by noise, we briefly review the nomenclature used in describing homogeneous, isotropic turbulence (which is how define initial "noise" in this paper). We consider the differential kinetic energy spectrum per unit mass $E(k)$ as a function of spatial wave number $k \equiv |\mathbf{k}| = \sqrt{k_x^2 + k_y^2 + k_z^2}$. Often, the spectrum has a power-law dependence on k so $E(k) = E_0\, k^{-a}$, where a is the spectral index and E_0 is a constant. For example, Kolmogorov turbulence has $a = 5/3$. To simplify our analysis, we consider a constant (unity) density fluid (which is reasonable approximation for lengthscales in a disk that are less than the disk's vertical pressure scale height). The turbulence has a total kinetic energy of $E = \int_0^\infty E(k)\, dk$, an rms velocity equal to $\sqrt{2E} = C_s\, Ma_{rms}$, and $Ro_{rms} = [\int_0^\infty E(k)\, k^2\, dk]^{1/2}$.

It is useful to break up the turbulent velocity into a sequence of eddies, with each eddy half the size of the preceding eddy in the sequence. An eddy with wavenumber k and lengthscale $l \equiv 2\pi/k$ has kinetic energy $\int_k^{2k} E(k')\, dk'$ and and an rms eddy velocity of

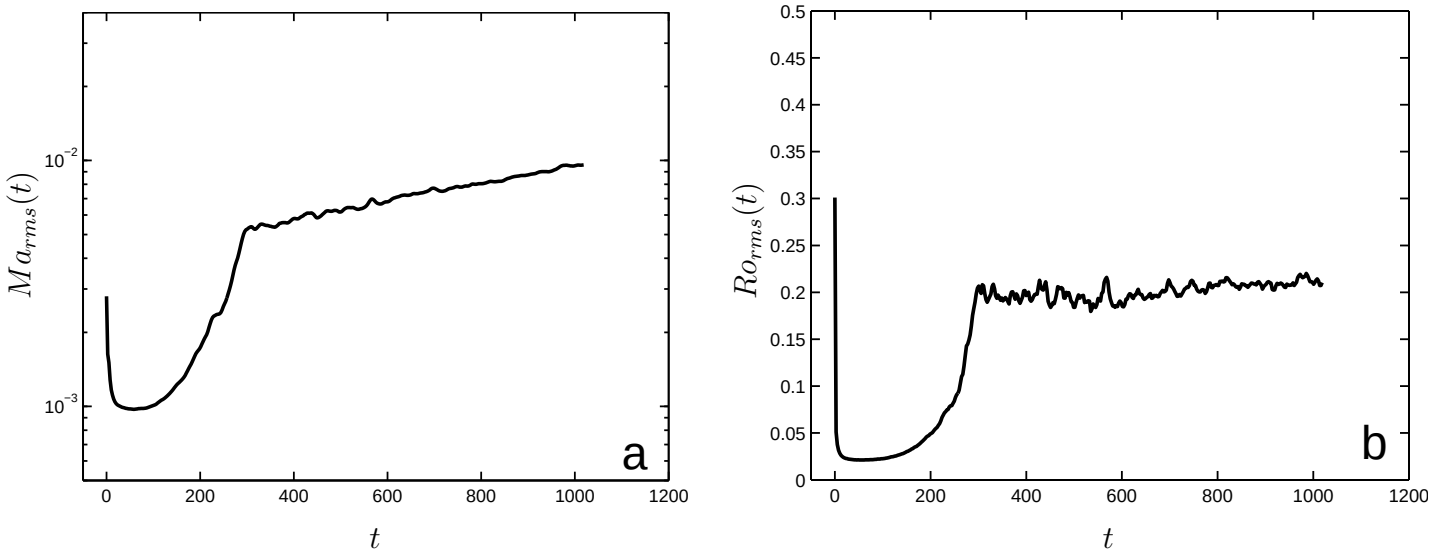

Figure 4.10: As in Figure 4.9 for an anelastic flow with same values of $\beta = 10$ (and $N_0/\Omega_0 = 2$) as in Figure 4.9, but with an initial fluctuation kinetic energy per unit mass of 4×10^{-5}, which is $4/9^{th}$ of the value in Figure 4.9. After $t \simeq 500\ yrs$, the statistical properties of the flows in Figure 4.9 and Figure 4.10 are nearly the same, which shows that the flows are drawn to at attractor that is independent of the details of the initial conditions.

$V_{eddy}(l) = [2\int_k^{2k} E(k')\,dk']^{1/2}$. For an $E(k)$ with spectral index a:

$$V_{eddy}(l) = V_{eddy}(L)\,(l/L)^{(a-1)/2}, \tag{4.34}$$

where L is the largest lengthscale of the flow.

We define the Rossby number $\widetilde{Ro}(k)$ and the Mach number $\widetilde{Ma}(k)$ of the eddy with wavenumber $k = 2\pi/l$ as:

$$2\Omega_0\, l\, \widetilde{Ro}(k) \equiv C_s\, \widetilde{Ma}(k) \equiv V_{eddy}(l), \tag{4.35}$$

so

$$\begin{aligned} \widetilde{Ma}(k) &\propto k^{(1-a)/2} \\ \widetilde{Ro}(k) &\propto k^{(3-a)/2} \end{aligned} \tag{4.36}$$

In particular, for the Kolmogorov spectrum with $a = 5/3$,

$$V_{eddy}(l) = V_{eddy}(L)\,(l/L)^{1/3} \tag{4.37}$$

$$\widetilde{Ma}(k) \propto k^{-1/3} \tag{4.38}$$

$$\widetilde{Ro}(k) \propto k^{2/3} \tag{4.39}$$

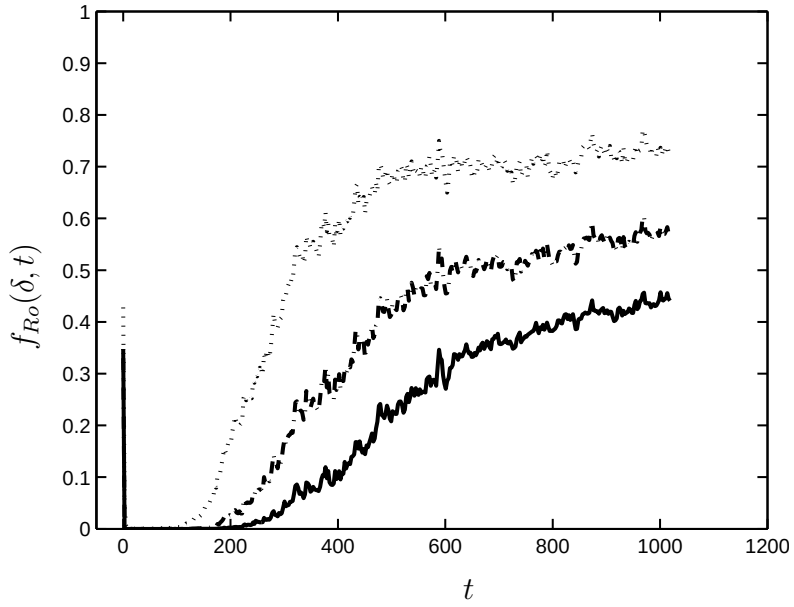

Figure 4.11: Time evolution of the spatial filling factor $f_{Ro}(\delta, t)$ of $|Ro|$ for the anelastic flow in Figure 4.3 and Figure 4.9 with an initial fluctuation kinetic energy per unit mass of 9.2×10^{-5} and with $\beta = 10$ or $N_0/\Omega_0 = 2$. $f_{Ro}(\delta, t)$ is the volume fraction of the computational domain that has $|Ro(x, y, z, t)| \geq \delta$. Dotted line for $\delta = 0.1$; dashed line for $\delta = 0.2$; solid line for $\delta = 0.3$. These filling factors are typical of all of our anelastic calculations.

For turbulence with spectral index $1 < a < 3$, equations (4.36) show that an eddy's kinetic energy and velocity decrease with decreasing lengthscale l, while its vorticity increases. Equivalently, with increasing k, $\widetilde{Ro}(k)$ increases and $\widetilde{Ma}(k)$ decreases. The implication of this is that most of the energy is at the large lengthscales, while most of the enstrophy is at the smallest. The largest lengthscale eddies contribute the most to the rms Mach number, while the smallest eddies contribute most to the rms Rossby number. For a turbulent spectrum with a large inertial range (i.e., where the ratio of its largest wavenumber to its smallest is large), the ratio of the rms velocity of the largest lengthscale eddy to the rms velocity of the total flow is

$$[1 - (1/2)^{(a-1)}]^{1/2}, \tag{4.40}$$

so for Kolmogorov turbulence, the rms Mach number of the largest eddy is 61% that of the rms Mach number of the total flow.

If the smallest lengthscale of the turbulence is determined by viscous dissipation, then that length l_ν is such that $l_\nu \, V_{eddy}(l_\nu) = \nu$, where ν is the kinematic viscosity, and eq. (4.34) shows that

$$l_\nu / L = Re^{-2/(1+a)}, \tag{4.41}$$

where $Re \equiv (L \, V_{eddy}(L))/\nu$ is the Reynolds number of the flow. For Kolmogorov turbulence with $a = 5/3$, l_ν is called the Kolmogorov length and is equal to $L \, Re^{-3/4}$.

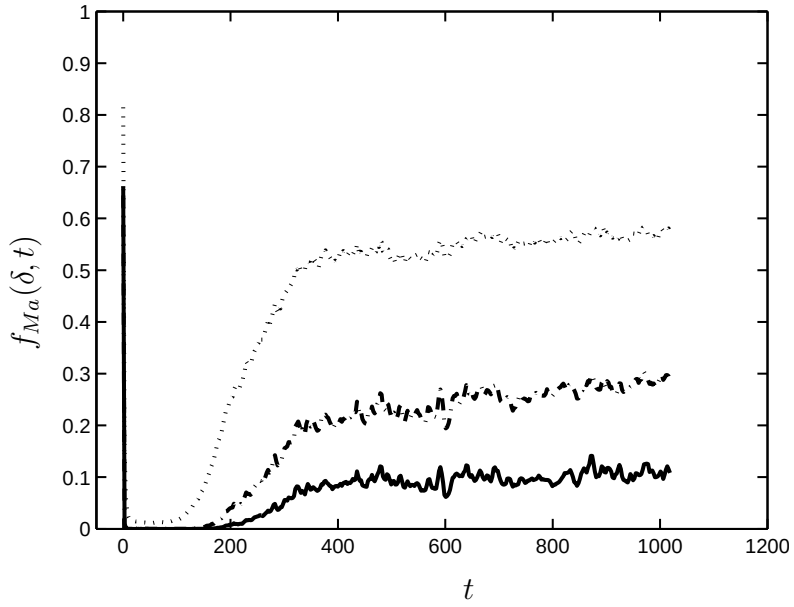

Figure 4.12: Filling factor for the flow in Figure 4.11, but for the Mach number where $f_{Ma}(\delta, t)$ is the volume fraction of the computational domain that has $Ma(x, y, z, t) \geq \delta$. Dotted line for $\delta = 0.1$; dashed line for $\delta = 0.2$; solid line for $\delta = 0.3$. At late times, the values of $f_{Ma}(\delta, t)$ are slaved to the values of $f_{Ro}(\delta, t)$. As shown in the text, for a fully compressible protoplanetary disk, we expect that the Mach and Rossby numbers, along with their filling factors, have the sames, with the values of the Rossby numbers and filling factors similar to those in Figure 4.8 – Figure 4.11.

We caution the reader that an eddy is not equivalent to a Fourier mode $\tilde{\mathbf{v}}_\mathbf{k}$ of the velocity, but rather it is the sum or integral of a band of Fourier modes with different wavenumbers centered around wavenumber $|\mathbf{k}|$. Unfortunately, there have been some confusion in the literature incorrectly stating that $|\tilde{\mathbf{v}}_\mathbf{k}|$ scales with k the same way as $V_{eddy}(2\pi/k)$ scales. If a turbulent velocity with spectral index a is written as a discrete sum of Fourier modes,

$$\mathbf{v}(\mathbf{x}) = \sum_{k_x} \sum_{k_y} \sum_{k_x} \tilde{\mathbf{v}}_\mathbf{k} \, e^{i\,\mathbf{k}\cdot\mathbf{x}}, \tag{4.42}$$

then

$$|\tilde{\mathbf{v}}_\mathbf{k}| \propto k^{-(a+2)/2} \tag{4.43}$$

because there are $[7\,(4\pi/3)|\mathbf{k}|^3$ Fourier modes in an eddy of wavenumber k made of Fourier modes between k and $2k$, so the energy of an eddy of wavenumber k is $2V_{eddy}(2\pi/k)^2 = 2|\tilde{\mathbf{v}}_\mathbf{k}|^2\ [7\,(4\pi/3)k^3]$. The velocity of the turbulent initial noise used in the calculations in this paper were created using eqs. (4.42) and (4.43) where the $\tilde{\mathbf{v}}_\mathbf{k}$ have random phases.

Figure 4.13 and Figure 4.14 illustrate how the spectral index a affects the spatial pattern and lengthscales of the vertical velocity and vertical vorticity of the initial noise in our calculations. Figure 4.13 is computed with Kolmogorov noise with $a = -5/3$ and shows

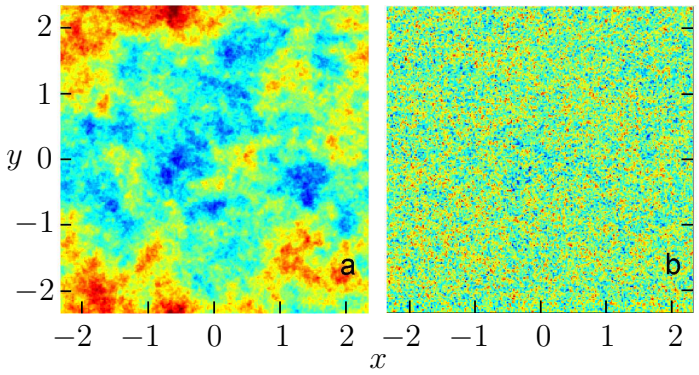

Figure 4.13: Vertical velocity (panel a) and vertical vorticity (panel b), shown in the x-y plane, of Kolmogorov noise with a spectral index $a = 5/3$. The largest lengthscales dominant the velocity, while the smallest lengthscales dominate the vorticity.

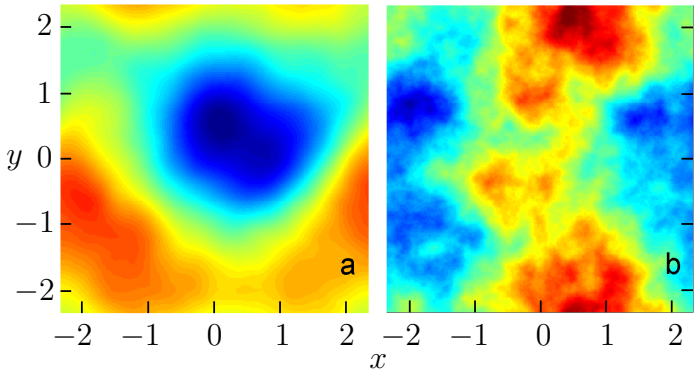

Figure 4.14: As in Figure 4.13 but with $a = 5$. Both the velocity and vorticity are dominated by the largest lengthscales.

the general behavior of turbulence with $1 < a < 3$: the velocity is gathered into large scale features, while the vorticity is dominated by the smallest scales (as also shown inFigure 4.5a and Figure 4.6a). In Figure 4.14, $a = 5$, so in accord with eqs. (4.36), $\widetilde{Ro}(k)$ and $\widetilde{Ma}(k)$ both decrease with increasing k, and the velocity and the vorticity are gathered into large scale features.

Threshold for the zombie instability

We have found that initial perturbations of noise can trigger the zombie instability in anelastic and fully compressible flows with a wide range of flow parameters. To determine the necessary threshold amplitude of the initial noise to trigger instability in an anelastic flow with $q = 3/2$, with uniform gravity g_0, and $\beta = 10$ or $N_0/\Omega_0 = 2$, we carried out three sets of numerical experiments in which we varied the properties of the initial noise. The dashed line in Figure 4.15a shows the initial spectrum $\widetilde{Ro}(k)$ of the Kolmogorov noise that we used

in a numerical experiment that did *not* produce zombie turbulence, but in which the initial non-Keplerian kinetic energy decayed. Because the initial noise has a Kolmogorov energy spectrum, $\widetilde{Ro}(k)$ increases with wavenumber as $k^{2/3}$ (i.e., with a slope in this semi-log plot of 2/3); while $\widetilde{Ma}(k)$ (not plotted) decreases as $k^{-1/3}$. The vertical dotted line in Figure 4.15*a* is the resolution wavenumber k_{res} of the calculation, i.e., wavenumbers with $k > k_{res}$ are specifically not included in the numerical calculation. In Figure 4.15*a* $k_{res} = 256\,(2\pi/L_x)$. To find a flow that was stable, rather than unstable, to the zombie instability, we began with the Kolmogorov noise that destabilized the anelastic flow shown in Figure 4.3. We then carried out a sequence of runs in which we steadily decreased the amplitude of the noise, while keeping all of the flow parameters and computational parameters fixed until we found a sufficiently low amplitude that the flow was not destabilized. Then, we carried out a binary-chop search on the amplitude of the initial noise to find the minimum threshold amplitude of the initial noise that triggered the zombie instability. Figure 4.15*a* illustrates the search. The flow with the unbroken curve in Figure 4.15*a* is the $\widetilde{Ro}(k)$ of an initial Kolmogorov noise (i.e., with slope 2/3) that destabilized the flow. Therefore, the $\widetilde{Ro}(k)$ of the noise with the minimum value for instability is bracketed between the broken and unbroken curves in Figure 4.15*a*. By carrying out the other two sets of numerical experiments (discussed below), we concluded that the criterion for instability is set by the maximum value of $\widetilde{Ro}(k)$ of the initial noise, and for $\beta = 10$ and $q = 3/2$, we determined that the minimum value $\widetilde{Ro}^*$ of $\widetilde{Ro}(k)$ needed to destabilize the flow is $\sim$ 0.19. The horizontal broken lines in all three panels of Figure 4.15 show $\widetilde{Ro}^*$. Because $\widetilde{Ro}(k)$ increases with k in all of the curves shown in Figure 4.15, the maximum value of the initial $\widetilde{Ro}(k)$ is $\widetilde{Ro}(k_{res})$. Therefore, $\widetilde{Ro}^*$ is bracketed by the two values of $\widetilde{Ro}(k_{res})$ shown in Figure 4.15*a*.

To convince ourselves that the maximum value of the initial $\widetilde{Ro}(k)$ is what determines whether the noise destabilizes the flow and that $\widetilde{Ro}^* \simeq 0.19$, we carried out a second series of numerical experiments for an anelastic flow with $\beta = 10$, $q = 3/2$. In these experiments, the kinetic energy of the initial noise was held fixed along with all of the flow and computational parameters. We chose the value of the kinetic energy of the initial noise to be the same as in the dashed curve in Figure 4.15*a*, which failed to destabilize the flow. In this new set of experiments, the only quantity that was varied was the spectral index a of the initial noise. In Figure 4.15*b*, the dashed curve is identical to the dashed curve in Figure 4.15*a*, which has a Kolmogorov spectral index of $a = 5/3$. The solid curve is $\widetilde{Ro}(k)$ for the initial noise with $a = 1 < 5/3$, (and therefore $\widetilde{Ro}(k)$ has a steeper slope of $(3 - a)/21 > 2/3$). This initial noise of the solid curve destabilized the flow. By carrying out a binary-chop on the minimum value a^* of $1 < a < 5/3$, we determined its threshold value needed to destabilize the flow. However, it is *n*ot the value of a^* that is important; its value is an artifact of the numerical resolution and initial energy of the noise – see below). What is important is that when a is equal to a^*, we find that $\widetilde{Ro}(k_{res})$ is equal to $\widetilde{Ro}^*$. In Figure 4.15*b*, $\widetilde{Ro}^*$ is bracketed by the values of $\widetilde{Ro}(k_{res})$ of the noise that destabilizes the flow (solid line) and the noise that fails to destabilize it (dashed line). These experiments support (but do not prove) our hypothesis

that it is the maximum value of $\widetilde{Ro}(k)$ that determines whether the noise triggers the zombie instability and that $\widetilde{Ro}^* \simeq 0.19$ for flows with $\beta - 10$, $q = 3/2$. However, because the values of the initial noise's kinetic energy and rms Mach number are the same in all of the runs in this second set of experiments, these experiments prove that neither the amplitude of the energy nor the rms Mach number of the initial noise determine whether the noise triggers the instability.

The third set of numerical experiments that we carried out to show that stability is determined by the maximum value of $\widetilde{Ro}(k)$ and that $\widetilde{Ro}^* \simeq 0.19$ is illustrated in Figure 4.15c. The flows in this set of experiments have $\beta = 10$, $q = 3/2$, and initial noise in all of the runs is Kolmogorov with identical energy spectra, $E(k) = E_0\, k^{-5/3}$, where the value of E_0 is the same in all of the experiments. Because E_0 is held fixed, the largest lengthscale eddies in the initial noise have the same Mach numbers and same Rossby numbers in all of our experiments. Equivalently, for $k \to 0$, the $\widetilde{Ro}(k)$ and $\widetilde{Ma}(k)$ of the initial noise is the same in all of the experiments. What changes in these experiments is the value of k_{res}. In Figure 4.15c the initial Kolmogorov noise represented by the dashed curve is the same as in in Figure 4.15ab. This calculation has $k_{res} = 256\,(2\pi/L_x)$, and the noise failed to destabilize the flow. The initial Kolmogorov noise corresponding to the solid curve in Figure 4.15c has $k_{res} = 384\,(2\pi/L_x)$. and it destabilizes the flow. By carrying out a binary chop search on k_{res}, we found that the minimum value k^*_{res} of k_{res} that destabilizes the flow. However, it is the value of k^*_{res} that is important; its value is an artifact of the spectral index and energy of the initial noise. What is important is that when $k_{res} = k^*_{res}$, we find that $\widetilde{Ro}(k_{res}) = \widetilde{Ro}^*$. In Figure 4.15$c$, $\widetilde{Ro}^*$ bracketed by the values of $\widetilde{Ro}(k_{res})$ for the noise that destabilizes the flow (solid line) and for the noise that fails to destabilize it (dashed line). These experiments adds further support (but still do not rigorously prove) our hypothesis that it is the maximum value of $\widetilde{Ro}(k)$ that determines whether the noise triggers the zombie instability and that $\widetilde{Ro}^* \simeq 0.19$ for flows with $\beta - 10$, $q = 3/2$. However, because the values the Mach numbers and Rossby numbers of the initial noise's largest lengthscale eddies are the same in all of the runs in this third set of experiments, the experiments prove that neither the Mach number or Rossby number of largest eddies in the initial noise determines whether the noise triggers the instability. Although the values of the kinetic energy of the initial is not held fixed in this series of numerical experiments, for all practical purposes it is: the difference in its value for two experiments with resolutions of k_{res} and k'_{res} is $\int_{k_{res}}^{k'_{res}} E_0\, k^{-5/3}\, dk$, which is negligible compared to the total energy of the initial noise, $\int_{2\pi/L}^{k'_{res}} E_0\, k^{-5/3}\, dk$.

This third set of experiments has important implications for astrophysical flows. Generally, *l*inear instabilities are viewed as more "reliable" in destabilizing a flow than a finite-amplitude instability because the threshold for the latter might be too large. For example, in a protoplanetary disk, it may be that the initial noise does not have sufficient energy or the initial noise does not have a sufficiently high Mach number to trigger a finite-amplitude instability. For the zombie instability this is not a problem. Three properties of protoplanetary disks and turbulence conspire to make the energies and Mach numbers of the needed

noise to trigger the zombie instability in a protoplanetary disk extraordinarily small: (1) the trigger for zombie instability depends on the maximum value of the Rossby number of the eddies in the noise, (2) in turbulence with a spectral index with $1 < a < 3$ the Mach numbers and the and kinetic energies of eddies decrease with increasing wavenumber k, while their Rossby numbers increases with k, and (3) the viscosity of the fluid is relatively small. If the the requirement to trigger instability is that for some k, $\widetilde{Ro}(k) \geq \widetilde{Ro}^*$, and if $a < 3$, then this requirement becomes

$$\widetilde{Ro}(k_>) > \widetilde{Ro}^*, \tag{4.44}$$

where $k_>$ is the largest wavenumber in the flow (which in a numerical calculation would be k_{res}, and in a viscously damped flow would be $2\pi/l_\nu$). Using eq. (4.36), eq. (4.44) becomes

$$\left[\frac{L\,k_>}{2\pi}\right]^{\frac{3-a}{2}} \tilde{Ro}\left(\frac{L}{2\pi}\right) > \widetilde{Ro}^*, \tag{4.45}$$

and using eq. (4.35), eq. (4.45) becomes

$$\left[\frac{2\Omega_0\,L}{C_s}\right]\left[\frac{L\,k_>}{2\pi}\right]^{\frac{3-a}{2}} \widetilde{Ma}\left(\frac{L}{2\pi}\right) > \widetilde{Ro}^*. \tag{4.46}$$

Using eq. (4.40), eq. (4.46) becomes

$$[1-(1/2)^{(a-1)}]^{1/2}\left[\frac{2\Omega_0\,L}{C_s}\right]\left[\frac{L\,k_>}{2\pi}\right]^{\frac{3-a}{2}} Ma_{rms} > \widetilde{Ro}^*. \tag{4.47}$$

For Kolmogorov turbulence and with $k_> = 2\pi/l_\nu$, eq. (4.47) becomes

$$Ma_{rms} > 0.8\,\beta^{1/2}\left[\frac{H}{L}\right]\widetilde{Ro}^*\,Re^{-1/2}, \tag{4.48}$$

where we used eq. (4.21) to eliminate C_s. For fully compressible flows $\beta = 1$. Many authors have argued (c.f., BM05) that due to the shear in a protoplanetary disk, it is difficult for coherent objects to have L much greater than H and that vortices will merge and inverse cascade their energies until $L \simeq H$. Therefore, in a protoplanetary disk, eq. (4.48) shows that the condition for Kolmogorov noise to have a sufficiently large amplitude to trigger the zombie instability is

$$Ma_{rms} > Re^{-1/2}. \tag{4.49}$$

Typical Reynolds numbers Re of the noise in protoplanetary disks are $\sim 10^{12}$, so the disks will go unstable if $Ma_{rms} > 10^{-6}$. Thus, although the zombie instability is formally a linear instability and requires a finite-sized perturbation to trigger it, the requirement on the amplitude of the noise is so small that for all practical purposes it can be considered to be

like a linear instability. Another way of showing how small the amplitude is that is needed to trigger the instability is to re-write eq. (4.49) as

$$Ma_{rms} > \frac{\nu}{L\,C_s} \simeq \frac{\Lambda}{L}, \tag{4.50}$$

where we have used the definitions of the Mach and Reynolds numbers to obtain the first part of eq.(4.50), and the fact that for most ideal gases $\nu \simeq \Lambda\, C_s$ to obtain the second part, where Λ is the mean free path of the gas.

Note that if the energy spectrum $E(k)$ of the initial turbulence is so steep that $\widetilde{Ro}(k)$ decreases, rather than increases, with k, then the noise must have a much larger Mach number, of order $\widetilde{Ro}^*$, to destabilize the flow. Thus if the spectral index a of the initial turbulent noise were greater than 3, then the noise must have a significant Mach number to destabilize the flow. In Figure 4.1, BHS96 used initial noise with a spectrum of $E(k) \propto k^2\, e^{-k^2}$, which is so steep that $\widetilde{Ro}(k)$ decreases with k. Thus, even if vertical gravity and density stratification had been included in their calculations, the initial Mach number would have had to been 6 orders of magnitude large than 10^{-6} to trigger the zombie instability, which argues that future tests of disk instability should be carried out with physically relevant energy spectra.

Caption for Figure 4.15 : Plot of $\widetilde{Ro}(k)$ for three sets of experiments. All of the unperturbed steady equilibrium flows in the figures are anelastic with $\beta = 10$, or $N_0/\Omega_0 = 2$, and with $L_x = L_y = L_z = H$. In all three panels, the thin broken horizontal dash line is $\widetilde{Ro}^* = 0.1913$, which corresponds to the lowest Rossby number of the initial noise that destabilizes the flow. The thin vertical dotted line is $k = 256\,(2\pi/L_x)$, which is the spatial resolution of the calculations in panels (a) and (b). For all the calculations shown here, the largest value of $\widetilde{Ro}(k)$ occurs when $k = k_{res}$, the largest wavenumber of the computed flow. In all three panels, the thick broken straight line with slope 2/3 is the $\widetilde{Ro}(k)$ of a calculation that has initial Kolmogorov turbulence with an amplitude that is a little too weak to destabilize the flow, and that initial noise has $\widetilde{Ro}(k_{res}) < \widetilde{Ro}^*$. **a**) The thick unbroken straight line is the $\widetilde{Ro}(k)$ of initial Kolmogorov turbulence with an amplitude that is large enough to destabilize the flow. That line has $\widetilde{Ro}(k_{res}) > \widetilde{Ro}^*$. **b**) The thick unbroken straight line is the $\widetilde{Ro}(k)$ of initial turbulence with a spectral index $a = 1$. This noise destabilizes the flow. The kinetic energies of the initial noise represented by the thick solid and broken lines are equal, but the thick unbroken curve has $\widetilde{Ro}(k_{res}) > \widetilde{Ro}^*$. **c**) The thick unbroken straight line is the $\widetilde{Ro}(k)$ of initial Kolmogorov turbulence that destabilizes the flow. This initial turbulence has an energy spectrum $E(k) = E_0\,k^{-5/3}$ that is identical to the spectrum of the thick broken line (which is plotted with slight vertical displacement so that it is not covered by the thick solid line). However, the flow with the initial noise represented by the thick solid line was computed with a k_{res} that was greater than the resolution of the calculation represented by the thick broken curve. The thick unbroken line has $\widetilde{Ro}(k_{res}) > \widetilde{Ro}^*$.

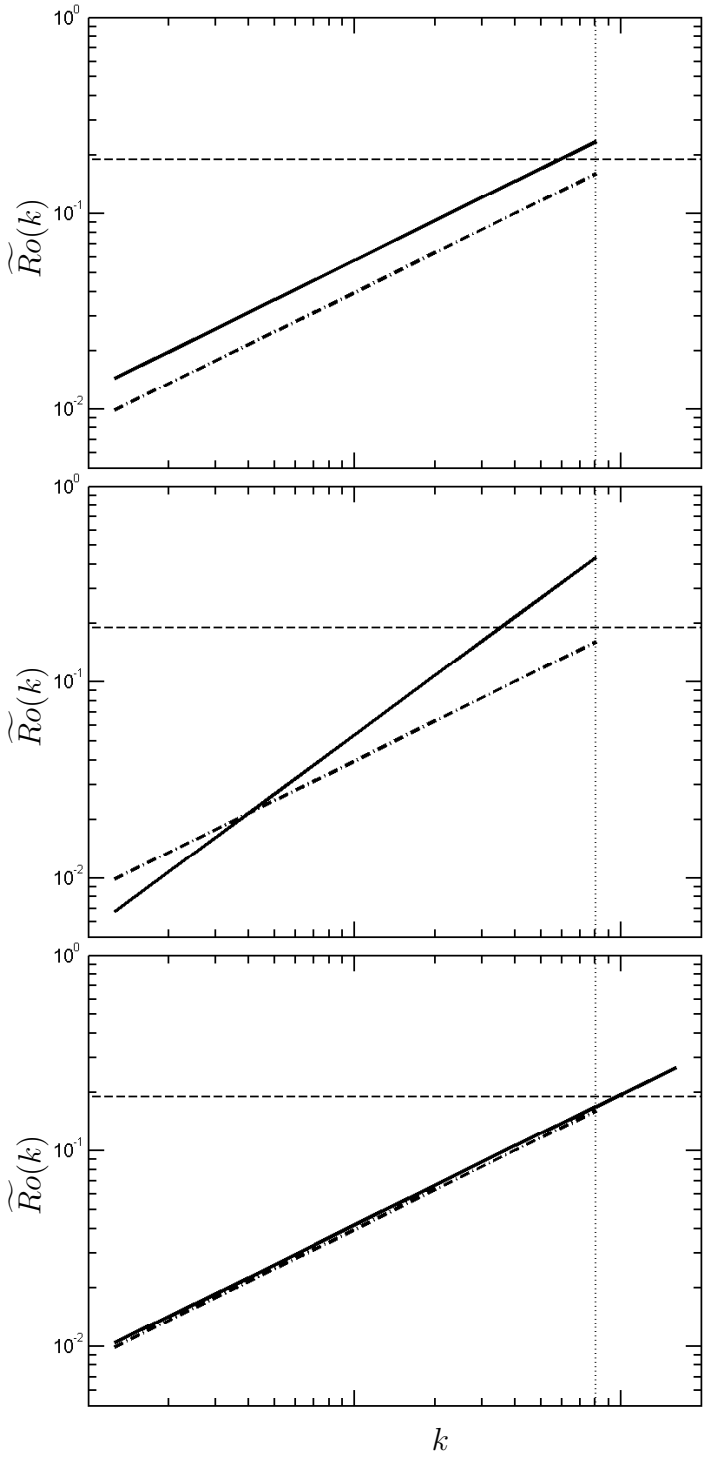

Figure 4.15: caption for figure 15 on next page

4.5 Review of the Physics of the Zombie Instability

The zombie instability is due to the excitation of a neutrally stable, eigenmode followed by the linear instability of a vortex layer. It is most easily analyzed using the Boussinesq equations (4.24) – (4.29) with a spatially uniform gravity g_0 and Brunt-Väisälä frequency N_0 and with an unperturbed, steady, equilibrium density that is linear in z as in eq. (4.28). The analysis is the same in anelastic and fully compressible flows and with flows in which g and N are not uniform, but these cases require a WKB expansion [Mathews and Walker 1970].

Neutrally stable linear eigenmodes and critical layers

When eqs. (4.24), (4.26), and (4.29) are linearized about a steady equilibrium velocity $\bar{\mathbf{v}}(x)$ and pressure $\bar{P}$ and $\bar{\rho}(z)$ in eq. (4.28), with $g = g_0$ and $N = N_0$, the eigenmodes are proportional to $e^{i(k_y y + k_z z - st)}$. The eigen-equation for the eigenmodes of this linearization is a generalization of Rayleigh's equation [Drazin and Reid 1981b] and is a 2^{nd}-order o.d.e in which the coefficient of the highest-derivative term is

$$[\bar{v}_y(x) - s/k_y]\{[\bar{v}_y(x) - s/k_y]^2 - (N_0/k_y)^2\}. \tag{4.51}$$

It should be noted that *a*ny velocity field $\bar{v}_y(x)$ for any function of x is a steady equilibrium solution of the Boussinesq equations (4.24), (4.26), and (4.29) for $v_y = v_x = 0$ and for $\bar{\rho}(z)$ given by eq. (4.28) with an appropriate $\bar{P}$. The coefficient given by expression (4.51) is valid not only for $\bar{v}_y = q\,\Omega_0\,x$, but also for arbitrary $v_y(x)$. When the initial steady equilibrium density $\bar{\rho}(z)$ is stably-stratified or constant and when $\bar{\mathbf{v}} = 3/2\,\Omega_0\,\hat{\mathbf{y}}$ (i.e., Keplerian flow), the flow is neutrally linearly stable (i.e., s is real, and eigenmodes neither grow nor decay). Eigenmodes of an o.d.e. are singular at locations x^* where the coefficient of the highest-derivative term of the eigen-equation is zero [Mathews and Walker 1970] and at x^* create *c*ritical layers [Drazin and Reid 1981b]. Although these eigenmodes are singular, they are not just mathematical curiosities but are relevant to flows in protoplanetary disks and in the laboratory: in fluids with viscosity ν, the "infinities" in the eigenmodes are replaced by terms proportional to $\nu^{-1/3}$. For neutrally stable fluids with uniform density ρ_0, eq. (4.51) shows that locations x^* of the critical layers obey $\bar{v}_y(x^*) = s/k_y$. We refer to these as *b*arotropic critical layers. Laboratory experiments and numerical computations show that neutrally stable eigenmodes with barotropic critical layers are difficult to excite, and, with the exception of contrived conditions in boundary layers, never form vortices. However, eq. (4.51) shows that there is another class of neutrally stable eigenmodes with critical layers that have $\bar{v}_y(x^*) - s/k_y \pm N_0/k_y = 0$, and we call them *b*aroclinic critical layers. [Boulanger et al. 2007] created weak baroclinic critical layers in a non-rotating, stratified flow in the laboratory. From MPJH13, we now know that those laboratory experiments could not produce strong critical layers and create zombie vortices due to the lack of rotation in the experiments. Rotation's important role in creating vertical vorticity is seen by taking the

curl of eq. (4.29):

$$\partial\omega_z/\partial t = -(\mathbf{v}\cdot\nabla)\omega_z + (\boldsymbol{\omega}\cdot\nabla)v_z + (2-q)\,\Omega_0\,(\partial v_z/\partial z), \tag{4.52}$$

where for now and the remainder of this section we restrict ourselves to linearly neutrally stable flows $\bar{v}_y(x) = q\,\Omega_0$. Vortex layers form at baroclinic critical layers because v_z, the z-component of the velocity eigenmode, and $(\partial v_z/\partial z)$ are large (in fact, singular) there. Equation (4.52) shows that the generalized Coriolis term $(2-q)\,\Omega_0\,(\partial v_z/\partial z)$ creates ω_z. In contrast, barotropic critical layers do not create vortex layers because the y, rather than the z, component of their velocity eigenmodes are singular, and the eigenmodes' $(\partial v_z/\partial z)$ are finite and too weak to create vorticity via the Coriolis term.

Within a baroclinic critical layer, the singular $\partial v_z/\partial z$ is nearly anti-symmetric about $x = x^*$; on one side of the layer $\partial v_z/\partial z \to \infty$, and on the other $\partial v_z/\partial z \to -\infty$; thus, the last term in Eq. (4.52) creates a large-amplitude vortex layer centered at x^* that is made of dipolar segments with one side cyclonic ($\omega_z/\Omega_0 > 0$) and the other anticyclonic ($\omega_z/\Omega_0 < 0$) (c.f., Figure 4.16*a*). Vortex layers that are embedded in a background shearing flow, like those in a protoplanetary disk are, in general, linearly stable [unstable] when the relative vertical vorticity of the layer ω_z has the opposite [same] sign as the vertical vorticity of the background shearing flow. For a vortex layer embedded in a Keplerian disk, this means that a vortex layer with cyclonic ω_z is stable, while the anticyclonic layer is unstable. The linear instability of vortex layers is a generalization of the study of Kelvin-Helmholtz instability and are amenable to the same type of analyses [Drazin and Reid 1981b]. We examined the instabilities of embedded vortex layers that were aligned in the stream-wise direction of background shearing flows when we carried out studies to determine the conditions under which the Jovian zonal (east-west) flows become linearly unstable and create Great-Red-Spot-like vortices [Marcus 1993]. When a vortex layer goes unstable, its edges become wavy, the waves amplify, the layer breaks up into a stream-wise series of vortices, and eventually the vortices usually merge together into one, Moore-Saffman-like vortex [Marcus 1988; 1990]. An analysis of vortex layer stability and subsequent roll-up that was nearly identical to our study was carried out later by [Lovelace et al. 1999] in the context of the Rossby wave instability in accretion disks.

Vortex spacing

Figures 16 and 17 show how a linearly neutrally stable baroclinic critical layer forms a vortex layer and how the layer produces *z*ombie vortices. However, one of the most important pieces of physics shown in these two figures is how the near-periodic behavior develops in the cross-stream x direction. In expression (4.51) $k_y \equiv 2\pi m/L_y$ is the wavenumber in the stream-wise direction, where m is an integer and L_y is the domain size in y (which in a protoplanetary disk would be its circumference). Baroclinic critical layers have $k_y \neq 0$, and expression (4.51) shows that the locations of the critical layers are

$$x^* = -[(s \pm 1)/m]\,\Delta, \tag{4.53}$$

where $\Delta \equiv (L_y\, N_0)/(2\pi q \Omega_0)$. Eq. (4.53) should not be misunderstood. It does not mean that x^* is the radius in a protoplanetary disk where critical layers form, rather, x^* is the is the radial distance or distance in x between a perturbation and the location of the critical layer that it excites. The governing equations (4.24), (4.26), and (4.29) and their shearing box boundary conditions are invariant under translations in y and z, and also under translation in x by δ when accompanied by a stream-wise boost in velocity of $(q\Omega_0)\delta$. The latter symmetry is *s*hift-and-boost symmetry (c.f., [Goldreich and Lynden-Bell 1965; Marcus and Press 1977]) and is the symmetry that is exploited that allows the use of shearing box boundary conditions. Due to the shift-and-boost symmetry, the origin of the x-axis is not unique, so in eq. (4.53) x^* must be the relative distance between two features, in this case, a perturbation and the critical layer it excites. To demonstrate that this is the correct interpretation of x^*, we simulated flows in which the flow was perturbed by either a compact wave generator or by a single compact vortex. When we used a vortex as the initial perturbation, it was "shielded" and consisted of an anticyclone (with a shape given by the Moore-Saffman equation (4.30)) surrounded by an outer layer of cyclonic vorticity so that the total vorticity (i.e., its circulation) was zero [Hassanzadeh et al. 2012]. We shielded the vortex so that its velocity had only a short range effect compared to an unshielded vortex in which the velocity falls off slowly as the inverse distance from the vortex and has a more global effect. Figure 16 shows $\omega_z(x, y, z, t)$ in the x–y plane for $z \neq 0$ at four times where the initial shielded anticyclone is at the origin, so it lies in a plane distinct from the one shown in the figure. The initial density perturbation to the flow is confined to the interior of the shielded vortex at the origin. Note that the governing equations of motion allow ρ as well as the velocity and pressure to change in time. The perturbing vortex is nearly in a steady equilibrium with background flow $\bar{\mathbf{v}}$, so it primarily excites critical layers with frequencies $s = 0$. (This is confirmed by taking a time series of the velocity at locations inside the critical layer and determining its temporal Fourier components with a minimum entropy method.) The critical layers in Fig. 16(a) are at $|x^*|/\Delta = 1/|m|$ for $|m| = 1$, 2 and 3, and with no critical layers at $|x|/\Delta > 1$, in accord with the fact that the perturbation is at $x = 0$ and with eq. (4.53). Each critical layer has produced a dipolar vortex layer aligned in the stream-wise direction, and the ω_z $x/\Delta = 1/|m|$ appears as $|m|$ segments (i.e. dominated by $k_y = 2\pi|m|/L_y$) of dipolar stripes in the stream-wise y direction. Figure 4.16*b* shows cyclonic vortex layers that are wavy but that are more-or-less continuous and aligned in the stream-wise direction, indicating that they are stable; whereas the anticyclonic layers are clearly unstable, have roll-up into discrete anticyclones, and are starting to merge into one large anticyclone at each critical layer. In particular, the anticyclonic vorticity at $x/\Delta = 1/3$ has rolled up and merged into a single anticyclone (near $y/\Delta = 1.5$). The anticyclonic vorticity at $x/\Delta = 1/2$ has rolled up into an anticyclone near $y/\Delta = -0.5$. In contrast, the cyclonic ω_z near $x/\Delta = 1/2$ has formed a continuous, meandering filament. At later times (Figure 4.16*c*) the anticyclones near $x/\Delta = 1/3$ (and near $y/\Delta = 2$) and near $x/\Delta = 1/2$ (and near $y/\Delta = -1$) have become larger. The x–y plane in Figure 4.16 is at a z where the $|m| = 2$ anticyclones are strongest, so the $|m| = 3$ and 1 anticyclones appear artificially weak. Figure 4.16*c* and Figure 4.16*d* show critical layers and vortices at $|x|/\Delta > 1$, which according to eq.(4.53) cannot be cre-

ated by a perturbations at $x = 0$. The layers at $|x|/\Delta > 1$ are due to the self-replication of 1^{st}-generation vortices at $|x|/\Delta \leq 1$. A vortex at *a*ny location will excite critical layers in a manner exactly like the original perturbing vortex due to the shift-and-boost symmetry (and will have $s = 0$ when viewed in the frame moving with the perturbing vortex). Figure 4.16*c* shows 2^{nd}-generation critical layers at $1 < |x|/\Delta \leq 2$ all with $|m| = 1$ and excited by 1^{st}-generation vortices at $|x|/\Delta \leq 1$. Figure 4.16*d* shows 3^{rd}-generation critical layers at $2 < |x|/\Delta \leq 3$, and 4^{th}-generation critical layers forming at $|x|/\Delta > 3$. At later times the vortices from $|m| = 1$ critical layers dominate. At very late times, the vortices have cross-stream diameters of order unity. (See below.) Within each zombie vortex the density mixes so that it is in accord with its near hydrostatic and geo-cyclostrophic equilibrium (c.f., [Hassanzadeh et al. 2012]). However, there is horizontal, but very little vertical, mixing of density outside the vortices, so the background vertical density stratification and N remain within 1% of their initial unperturbed values. The lack of vertical mixing, despite strong horizontal mixing, was seen in our earlier simulations (BM06) and also in our laboratory experiments [Aubert et al. 2012] of vortices in rotating, stratified flows.

Figure 4.16 shows that each generation of vortices excites new critical layers in an adjacent unperturbed region, which spawn the next generation of vortices. The spawning of new generations of new critical layers from old critical layers, the self-replication of the vortices, the eventual takeover of the entire domain by the vortices, and the fact that the vortices are created in a "dead" zone, were the traits that led us in MPJH13 to naming them *z*ombie vortices.

Figure 4.17 shows the same flow as in Figure 4.16 but viewed in the x–z plane at $y = 0$. At late times the domain fills with anticyclones. Because the initial flow is homogeneous with uniform shear and N, the vortices form a regular lattice despite the flow's turbulence. As time progresses in Figure 4.16, the vortex population spreads out from the perturbing vortex at the origin. At early times (Figure 4.17*a*) the flow has 1^{st}-generation critical layers, with $|m| = 1$, 2, and 3 being most apparent. In this first generation, and all subsequent generations, a vortex perturbs the flow and creates four new prominent vortices at its $|m| = 1$ critical layers at locations in x that are $\pm l_x$ distant from itself and at locations in z that are $\pm l_z$ distant from itself. (l_x is physically set by, and equal to, the distance in x from a perturbing vortex to the anticyclonic piece of the vortex layer formed by its $|m| = 1$ critical layer; this distance is slightly greater than Δ.) The 2^{nd}-generation $m = 1$ critical layers created by the 1^{st}-generation vortices with $|m| = 1$, 2, and 3 are faintly visible in Figure 4.17*b* and much more so in Figure 4.17*c*. At later times (Figure 4.17*d*), the $|m| = 1$ vortices descended from the 1^{st}-generation $|m| = 1$ vortices dominate and form a lattice of zombie vortices located at $[x = 2n\ l_x, z = 2j\ l_z]$ and at $[x = (2n + 1)l_x, z = (2j + 1)l_z]$, for all integers n and j.

The creation of a lattice of *z*ombie vortices in an artifact of having one localized initial perturbation, and lattices do not form from initial noise. With noise, perturbations at random locations excite critical layers, and the vortices spawned from the different critical layers interact with each other, merge and inverse cascade their energies to larger length-scales. None the less, the spacing Δ in x between a perturbation and the fundamental critical

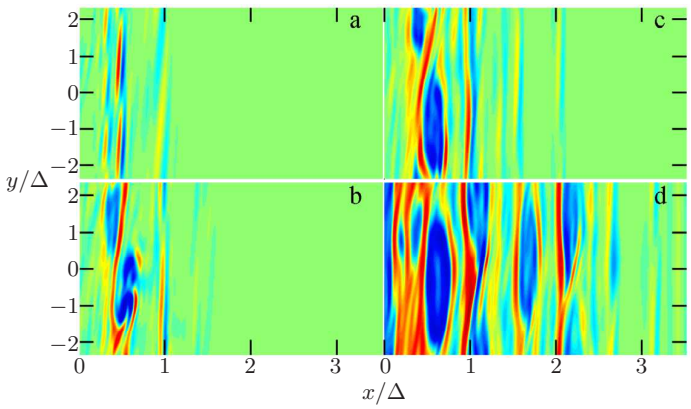

Figure 4.16: Boussinesq with constant gravity and Brunt-Väisälä frequency with $N_0/\Omega_0 = 2$. ω_z of the anticyclonic (blue) vortices and cyclonic (red) vortex layers in the x-y plane. The initial perturbing vortex at the origin is above the plane shown here ($z/\Delta = -0.4$). The first generation zombie vortices form at $|x|/\Delta \leq 1$, and sweep outward in x. The Rossby number Ro of these vortices is $\sim$ -0.2. (The color is reddest at $\omega_z/\Omega_0 = 0.4$, bluest at $\omega_z/\Omega_0 = -0.4$, and green at $\omega_z = 0$). $\Omega_0/N_0 = 0.5$ and $q = 3/2$. The x-y domain is $|x|/\Delta \leq 4.7124$; $|y|/\Delta \leq 2.3562$, and is larger than shown. a) $t = 64/N_0$. b) $t = 256/N_0$. c) $t = 576/N_0$. d) $t = 2240/N_0$.

layer it excites with $m = 1$ is evident in the temporal evolution of $z$ombie turbulence created from initial noise. This spacing Δ is what give the turbulence a near periodicity in x at late times in Figure 4.5, Figure 4.6 and Figure 4.7.

4.6 Conclusion and future work

Zombie instability shows in Boussinesq, anelastic and fully compressible simulations with our spectral code as well as the ATHENA code. It is not subtle and should be reproduced by various codes used in the astrophysical community. The reasons that previous study with fully-compressible simulations couldn't see it are: 1) insufficient resolution. The instability is due to baroclinic critical layers, which has near logarithm singularity in the cross-stream direction. Certain resolution is required to resolve the critical layers as we pointed out in [Marcus, Jiang, et al. 2013; Marcus, Pei, et al. 2013]. Even the initial Ro_{rms} reaches the critical value for the instability, the flow will not be destabilized if the critical layers are under resolved due to lack of resolution. Therefore, to trigger the instability, numerical simulations need to have high resolution and low dissipation to resolve critical layers, which is not attained in most of previous studies. 2) no gravity or vertical stratification missing. Most previous studies do not include gravity and initialize constant density flows, even though their initial Kolmogorov noises have Ma close to 1. In their simulations, they eliminates

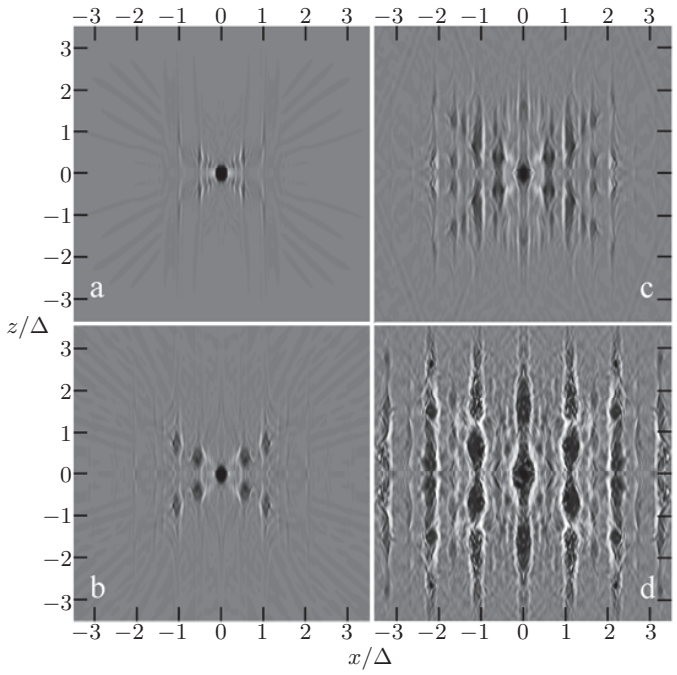

Figure 4.17: Zombie vortices sweep outward from the perturbing vortex at the origin in the x–z plane (at $y = 0$). Anticyclonic ω_z is black (darkest is $\omega_z/\Omega_0 = -0.4$) and cyclonic is white (lightest is $\omega_z/\Omega_0 = 0.4$). This is the same flow as in Figure 4.16. The domain has $|z|/\Delta \leq 4.7124$ and is larger than shown. a) $t = 128/N_0$. Critical layers and young zombie vortices with $s = 0$ and $|m| = 1$, 2, and 3 are visible. Diagonal lines are internal inertia-gravity waves with shear, not critical layers. b) $t = 480/N_0$. 1^{st}-generation vortices near $|x|/\Delta = 1$ and $1/2$ have rolled-up from critical layers with $s = 0$ and $|m| = 1$ and 2, respectively. c) $t = 1632/N_0$. 2^{nd}-generation vortices have spawned from the 1^{st} generation vortices. d) $t = 3072/N_0$. 1^{st}, 2^{nd} and 3^{rd} generation vortices.

the baroclinic effect which is required in zombie instability. 3) improper initial spectrum. From above analysis, only the spectrum with index $1 < a < 3$, has its Ro increase toward small scales. With improper spectrum, increasing resolution might either requires a very large Ma initial perturbation ($a < 1$) to trigger the instability or obtains a small Ro that cannot trigger the instability. 4) not wait enough time. Zombie instability in our simulations typically needs tens or hundreds of orbital periods to develop, depending on the magnitude of the initial perturbations. Short time evolution will not see it.

We have proved by our numerical simulations zombie instability is a finite amplitude instability. The threshold of the instability is set by the initial vorticity rather than velocity. Zombie instability happens with a very small initial Ma. There exists a critical value of rms vorticity such that if the initial noise has a rms vorticity larger than the critical value, the zombie instability will be triggered. For initial noise that has a spectrum $Ek(k) \sim k^a$ with

$1 < a < 3$, the smallest scale dominates the rms Rossby number. If the length of inertial range is long enough down to small scale such that it could reach the critical length scale at which the rms Rossby number is larger than the critical value, zombie instability will happen. Zombie instability can be seen as an effectively linear instability in PPDs. A infinitesimal velocity perturbation could have an infinite vorticity to trigger the zombie instability. For example, consider a star with mass of one solar nebular, based on the local sound speed and viscosity at 10AU, the Reynolds number will be 10^{10}, which provides a favorable condition for the zombie instability to happen.

The instability will saturates when the whole domain is filled with zombie vortices. These vortices have a Rossby number of -0.3. The filling factor of the zombie vortices is about 30%. In anelastic approximation we filter out the acoustic waves. However, acoustic waves play an key role in angular momentum transport [Johnson and Gammie 2005b; Lesur and Papaloizou 2010; Lyra and Klahr 2011; Raettig et al. 2013; Shen et al. 2006]. If we run the fully compressible simulation in a large enough domain, such that all the acoustic waves are allow to developed. Then based on our scaling analysis, $\alpha \prec Ma^2$ and $Ma \simeq Ro$, we will have an $\alpha \sim 10^{-2}$.

As (BM05, [Lesur and Papaloizou 2009]) pointed out, no stable mid-plane vortex has been found in the protoplanetary disk. Our numerical simulation here has its computational domain corresponding to an box above mid-plane. One may think even if it provides enough angular momentum transport with the zombie instability in our simulation, the effective transport at the mid-plane could still be a problem. This is another reason we need to go to the fully compressible simulation. For a fully developed compressible turbulence filed, there exists equi-partition of the kinetic energy between the solenoidal (toroidal and poloidal) parts and the dilatational part of the velocity [Kritsuk et al. 2007; Lemaster and Stone 2009]. In our anelastic simulation we have already showed zombie instability could produce large amount solenoidal energy from rotational turbulence. Based on equi-partition of kinetic energy, it is expected to also produce large amount of dilatational energy in terms of acoustic waves. Although the zombie vortices is not at the mid-plane, acoustic wave can propagate to the mid-plane thus provide enough angular momentum transport at the mid-plane to help star and planetesimal formations.

We have showed in Chapter 3, the saturation of instability only depends on background parameters rather than the initial conditions. We speculate zombie instability provide another equilibrium flow to the PPD in contrast to the laminar Keplerian flow. It is well known that pipe flow has two equilibrium solution. One is the laminar time-independent Poiseuille flow, while the other is a statistically steady turbulent flow that occurs at large Reynolds number. Both of the solutions are attractors to the pipe flow. At high Reynolds number, flows are most likely to be the turbulent flow rather than the laminar Poiseuille flow. By analogy, the turbulent flows created by the zombie instability could be the same as the turbulent flow solution in a pipe. Because PPDs have large Reynolds number, it is much more likely the flows are steady state turbulence rather than laminar Keplerian flows. Note most of the instability study of PPDs start from perturbing the laminar Keplerian flow. We argue that once PPD is created from a collapsing gas cloud, the flow will not be Keplerian,

but rather be the turbulent flows. Further, it could be the turbulent flows filled with zombie vortices.

Appendix: Wave Generator

Wave generator produces a 3D vector field changing with time added as external force term to the momentum equations. We define A, s, ϕ_0 to be the amplitude, frequency and the initial phase of the wave generator; x_{WG}, y_{WG}, z_{WG} to be the center of the wave generator; h_x, h_y, h_z to be the size of the wave generator in each direction. We use $\mathbf{F}$ as the force produced by the wave generator. $\mathbf{F}(x, y, z, t)$ is pure toroidal in space and can be written as:

$$\boldsymbol{F} = [\nabla \times \nabla \times (\psi \hat{\boldsymbol{z}})] \sin(st + \phi_0), \tag{4.54}$$

where ψ is a 3D scalor function that varies as a Gaussian function in all three directions

$$\psi = A \exp[-\frac{(x - x_{WG})^2}{2h_x^2} - \frac{(y - y_{WG})^2}{2h_y^2} - \frac{(z - z_{WG})^2}{2h_z^2}]. \tag{4.55}$$

For all the cases, the wave generator has an initial phase $\phi_0 = 0$. Its size is set to be $h_x = L_x/64, h_y = L_y/64, h_z = L_z/32$. Note since the wave generator is purely toroidal in space, it doesn't produce any vertical vorticity.

Bibliography

Adams, F. C. and R. Watkins. Vortices in Circumstellar Disks. *The Astrophysical Journal* 451 (Sept. 1995), p. 314.

Armitage, P. J. Dynamics of Protoplanetary Disk. *Annual Review of Astronomy and Astrophysics* 49 (2011), pp. 195–236.

Aubert, O., M. Le Bars, P. Le Gal, and P. S. Marcus. The universal aspect ratio of vortices in rotating stratified flows: experiments and observations. *Journal of Fluid Mechanics* 706 (Sept. 2012), pp. 34–45.

Avila, M. Stability and Angular-Momentum Transport of Fluid Flows between Corotating Cylinders. *Physical Review Letters* 108.12, 124501 (Mar. 2012), p. 124501.

Bai, X.-N. and J. Goodman. Heat and Dust in Active Layers of Protostellar Disks. *The Astrophysical Journal* 701 (Aug. 2009), pp. 737–755.

Balbus, S. A. Fluid dynamics: A turbulent matter. *Nature* 470 (Feb. 2011), pp. 475–476.

Balbus, S. A. and J. F. Hawley. A powerful local shear instability in weakly magnetized disks. I - Linear analysis. II - Nonlinear evolution. *The Astrophysical Journal* 376 (July 1991), pp. 214–233.

— Instability, turbulence, and enhanced transport in accretion disks. *Review of Modern Physics* 70 (1 Jan. 1998), pp. 1–53.

Balbus, S. A., J. F. Hawley, and J. M. Stone. Nonlinear Stability, Hydrodynamical Turbulence, and Transport in Disks. *The Astrophysical Journal* 467 (Aug. 1996), p. 76.

Bannon, P. R. On the anelastic approximation for a compressible atmosphere. *Journal of the Atmospheric Sciences* 53.23 (1996), pp. 3618–3628.

Bannon, Peter R. On the anelastic approximation for a compressible atmosphere. *Journal of the Atmospheric Sciences* 53.23 (1996), pp. 3618–3628.

Barge, P. and J. Sommeria. Did planet formation begin inside persistent gaseous vortices? *Astronomy & Astrophysics* 295.1 (1995), pp. L1–L4.

Barranco, J. A. and P. S. Marcus. A 3D spectral anelastic hydrodynamic code for shearing, stratified flows. *Journal of Computational Physics* 219 (Nov. 2006), pp. 21–46.

— Three-dimensional Vortices in Stratified Protoplanetary Disks. *The Astrophysical Journal* 623.2 (2005), p. 1157.

— "Vorticies in protoplanetary disks and the formation of planetesimals". In: *Center for Turbulence Research – Proceedings of the 2000 Summer Program*. 2000, pp. 97–108.

Barranco, J. A., P. S. Marcus, and M. Umurhan. "Scalings and asymptotics of coherent vortices in protoplanetary disks". In: *Center for Turbulence Research – Proceedings of the 2000 Summer Program*. 2000, pp. 85–96.

Boulanger, N., P. Meunier, and S. Le Dizés. Structure of a stratified tilted vortex. *Journal of Fluid Mechanics* 583 (July 2007), pp. 443–458.

Cabot, W. Numerical Simulations of Circumstellar Disk Convection. *The Astrophysical Journal* 465 (July 1996), p. 874.

Chagelishvili, G. D., J.-P. Zahn, A. G. Tevzadze, and J. G. Lominadze. On hydrodynamic shear turbulence in Keplerian disks: Via transient growth to bypass transition. *Astronomy & Astrophysics* 402 (May 2003), pp. 401–407.

Chandrasekhar, S. *Hydrodynamic and Hydromagnetic Stability*. New York: Dover Publications, 1981.

— The Stability of Non-Dissipative Couette Flow in Hydromagnetics. *Proceedings of the National Academy of Science* 46 (Feb. 1960), pp. 253–257.

Chiang, E. I. and P. Goldreich. Spectral energy distributions of T Tauri stars with passive circumstellar disks. *The Astrophysical Journal* 490.1 (1997), p. 368.

Drazin, P. G. and W. H. Reid. *Hydrodynamic Stability*. Cambridge: Cambridge University Press, 1981.

— *Hydrodynamic Stability*. Cambridge: Cambridge University Press, 1981.

Dubrulle, B. Differential rotation as a source of angular momentum transfer in the solar nebula. *Icarus* 106 (Nov. 1993), p. 59.

Dubrulle, B., L. Marié, Ch. Normand, D. Richard, F. Hersant, and J.-P. Zahn. A hydrodynamic shear instability in stratified disks. *Astronomy & Astrophysics* 429.1 (2005), pp. 1–13.

— A hydrodynamic shear instability in stratified disks. *Astronomy & Astrophysics* 429.1 (2005), pp. 1–13.

Fleming, T. and J. M. Stone. Local Magnetohydrodynamic Models of Layered Accretion Disks. *The Astrophysical Journal* 585 (Mar. 2003), pp. 908–920.

Fromang, S. and J. Papaloizou. Dust settling in local simulations of turbulent protoplanetary disks. *Astronomy & Astrophysics* 452 (June 2006), pp. 751–762.

Gammie, C. F. Layered Accretion in T Tauri Disks. *The Astrophysical Journal* 457 (1996), pp. 355–362.

Gardiner, T. A. and J. M. Stone. An unsplit Godunov method for ideal MHD via constrained transport in three dimensions. *Journal of Computational Physics* 227 (Apr. 2008), pp. 4123–4141.

Goldreich, P. and D. Lynden-Bell. II. Spiral arms as sheared gravitational instabilities. *Monthly Notices of the Royal Astronomical Society* 130 (1965), pp. 125–158.

Gough, DO. The anelastic approximation for thermal convection. *Journal of the Atmospheric Sciences* 26.3 (1969), pp. 448–456.

Hassanzadeh, P., P. S. Marcus, and P. Le Gal. The universal aspect ratio of vortices in rotating stratified flows: theory and simulation. *Journal of Fluid Mechanics* 706 (Sept. 2012), pp. 46–57.

Hawley, J. F., S. A. Balbus, and W. F. Winters. *Local Hydrodynamic Stability of Accretion Disks*. June 1999.

Hersant, F., B. Dubrulle, and J.-M. Huré. Turbulence in circumstellar disks. *Astronomy & Astrophysics* 429.2 (2005), pp. 531–542.

Hill, G. W. *Am J Math* 1 (1878), p. 5.

Ji, Hantao, Michael Burin, Ethan Schartman, and Jeremy Goodman. Hydrodynamic turbulence cannot transport angular momentum effectively in astrophysical disks. *Nature* 444.1 (2006), p. 343.

Johnson, B. M. and C. F. Gammie. Linear Theory of Thin, Radially Stratified Disks. *The Astrophysical Journal* 626 (June 2005), pp. 978–990.

— Nonlinear Stability of Thin, Radially Stratified Disks. *The Astrophysical Journal* 636 (Jan. 2006), pp. 63–74.

— Vortices in Thin, Compressible, Unmagnetized Disks. *The Astrophysical Journal* 635 (Dec. 2005), pp. 149–156.

King, A. R., J. E. Pringle, and M. Livio. Accretion disc viscosity: how big is alpha? *Monthly Notices of the Royal Astronomical Society* 376 (Apr. 2007), pp. 1740–1746.

Klahr, H. The Global Baroclinic Instability in Accretion Disks. II. Local Linear Analysis. *The Astrophysical Journal* 606 (May 2004), pp. 1070–1082.

Klahr, H. and P. Bodenheimer. Turbulence in Accretion Disks: Vorticity Generation and Angular Momentum Transport via the Global Baroclinic Instability. 582 (Jan. 2003), pp. 869–892.

Kritsuk, Alexei G., Michael L. Norman, Paolo Padoan, and Rick Wagner. The Statistics of Supersonic Isothermal Turbulence. *The Astrophysical Journal* 665.1 (2007), p. 416.

Kundu, P. K. *Fluid Mechanics*. San Diego, CA: Academic Press, 1990.

Le Bars, M. and P. Le Gal. Experimental Analysis of the Stratorotational Instability in a Cylindrical Couette Flow. *Physical Review Letters* 99 (6 Aug. 2007), pp. 64–502.

Le Dizés, S. and P. Billant. Radiative instability in stratified vortices. *Physics of Fluids* 21.9 (Sept. 2009), p. 096602.

Le Dizés, S. and X. Riedinger. The strato-rotational instability of Taylor-Couette and Keplerian flows. *Journal of Fluid Mechanics* 660 (2010), pp. 147–161.

Lemaster, M. N. and J. M. Stone. Dissipation and Heating in Supersonic Hydrodynamic and MHD Turbulence. *The Astrophysical Journal* 691.2 (2009), p. 1092.

Lesur, G. and P.-Y. Longaretti. On the relevance of subcritical hydrodynamic turbulence to accretion disk transport. *Astronomy & Astrophysics* 444 (Dec. 2005), pp. 25–44.

Lesur, G. and G. I. Ogilvie. On the angular momentum transport due to vertical convection in accretion discs. *Monthly Notices of the Royal Astronomical Society* 404 (May 2010), pp. L64–L68.

Lesur, G. and J. Papaloizou. On the stability of elliptical vortices in accretion discs. *Astronomy & Astrophysics* 498.1 (2009), pp. 1–12.

— The subcritical baroclinic instability in local accretion disc models*. *Astronomy & Astrophysics* 513 (2010), A60.

Li, H., S. A. Colgate, B. Wendroff, and R. Liska. Rossby Wave Instability of Thin Accretion Disks. III. Nonlinear Simulations. *The Astrophysical Journal* 551 (2001), pp. 874–896.

Li, H., J. M. Finn, R. V. E. Lovelace, and S. A. Colgate. Rossby Wave Instability of Thin Accretion Disks. II. Detailed Linear Theory. *The Astrophysical Journal* 533 (2000), pp. 1023–1034.

Lovelace, R. V. E., H. Li, S. A. Colgate, and A. F. Nelson. Rossby Wave Instability of Keplerian Accretion Disks. *The Astrophysical Journal* 513 (1999), pp. 805–810.

Lyra, W. and H. Klahr. The baroclinic instability in the context of layered accretion. *Astronomy & Astrophysics* 527 (2011).

Lyra, W. and M.-M. Mac Low. Rossby Wave Instability at Dead Zone Boundaries in Three-dimensional Resistive Magnetohydrodynamical Global Models of Protoplanetary Disks. *The Astrophysical Journal* 756, 62 (Sept. 2012), p. 62.

Marcus, P. S. Jupiter's Great Red Spot and Other Vortices. *Annual Review of Astronomy and Astrophysics* 31 (1993), pp. 523–569.

— Numerical simulations of the Great Red Spot of Jupiter. *nature* 331 (1988), pp. 693–696.

— Vortex dynamics in a shearing zonal flow. *Journal of Fluid Mechanics* 215 (1990), pp. 393–430.

Marcus, P. S., C.-H. Jiang, S. Pei, and P. Hassanzadeh. "The Dead Zones of Protoplanetary Disks are Not Dead". In: *European Physical Journal Web of Conferences*. Vol. 46. 2013, p. 03006.

Marcus, P. S., S. Pei, C.-H. Jiang, and P. Hassanzadeh. Three-Dimensional Vortices Generated by Self-Replication in Stably Stratified Rotating Shear Flows. *Physical Review Letters* 111 (8 Aug. 2013), p. 084501.

Marcus, P. S. and W. H. Press. On Green's functions for small disturbances of plane Couette flow. *Journal of Fluid Mechanics* 79.03 (1977), pp. 525–534.

Maslowe, S. A. Critical Layers in Shear Flows. *Annual Review of Fluid Mechanics* 18.1 (1986), pp. 405–432.

Mathews, Jon and Robert Lee Walker. *Mathematical methods of physics*. Vol. 271. WA Benjamin New York, 1970.

Meheut, H. "The Rossby wave instability in protoplanetary disks". In: *European Physical Journal Web of Conferences*. Vol. 46. European Physical Journal Web of Conferences. Apr. 2013, p. 3001.

Meheut, H., F. Casse, P. Varniere, and M. Tagger. Rossby wave instability and three-dimensional vortices in accretion disks. *Astronomy & Astrophysics* 516 (2010), A31.

— "The Rossby wave instability and planet formation: 3D numerical simulations". In: *SF2A-2008*. Ed. by C. Charbonnel, F. Combes, and R. Samadi. Nov. 2008, p. 417.

Meheut, H., Z. Meliani, P. Varniere, and W. Benz. Dust-trapping Rossby vortices in protoplanetary disks. *Astronomy & Astrophysics* 545, A134 (Sept. 2012), A134.

Meheut, H., C. Yu, and D. Lai. Rossby wave instability in 3D discs. *Monthly Notices of the Royal Astronomical Society* 422 (May 2012), pp. 2399–2406.

Molemaker, M. J., J. C. McWilliams, and I. Yavneh. Instability and Equilibration of Centrifugally Stable Stratified Taylor-Couette Flow. *Physical Review Letters* 86 (June 2001), pp. 5270–5273.

Moore, DW and PG Saffman. Structure of a line vortex in an imposed strain. In: *Aircraft wake turbulence and its detection*. Springer, 1971, pp. 339–354.

Ogura, Yoshimitsu and Norman A Phillips. Scale analysis of deep and shallow convection in the atmosphere. *Journal of the Atmospheric Sciences* 19.2 (1962), pp. 173–179.

Oishi, J. S. and M.-M. Mac Low. On Hydrodynamic Motions in Dead Zones. *The Astrophysical Journal* 704 (Oct. 2009), pp. 1239–1250.

Paoletti, M. S. and D. P. Lathrop. Angular Momentum Transport in Turbulent Flow between Independently Rotating Cylinders. *Physical Review Letters* 106.2, 024501 (Jan. 2011), p. 024501.

Paoletti, M. S., D. P. M. van Gils, B. Dubrulle, C. Sun, D. Lohse, and D. P. Lathrop. Angular momentum transport and turbulence in laboratory models of Keplerian flows. *Astronomy & Astrophysics* 547, A64 (Nov. 2012), A64.

Petersen, Mark R., Keith Julien, and Glen R. Stewart. Baroclinic Vorticity Production in Protoplanetary Disks. I. Vortex Formation. *The Astrophysical Journal* 658.2 (2007), p. 1236.

Petersen, Mark R., Glen R. Stewart, and Keith Julien. Baroclinic Vorticity Production in Protoplanetary Disks. II. Vortex Growth and Longevity. *The Astrophysical Journal* 658.2 (2007), p. 1252.

Raettig, Natalie, Wladimir Lyra, and Hubert Klahr. A Parameter Study for Baroclinic Vortex Amplification. *The Astrophysical Journal* 765.2 (2013), p. 115.

Rayleigh, Lord. On the dynamics of rotating fluid. *Proc. R. Soc. Lond. A* 93 (1916), pp. 148–154.

Richard, D. and J.-P. Zahn. Turbulence in differentially rotating flows. What can be learned from the Couette-Taylor experiment. *Astronomy & Astrophysics* 347 (July 1999), pp. 734–738.

Richard, S. and P. Barge. "Structure and evolution of 3D Rossby Vortices". In: *European Physical Journal Web of Conferences*. Vol. 46. European Physical Journal Web of Conferences. Apr. 2013, p. 3002.

Richard, S., P. Barge, and S. Le Dizès. Structure, stability, and evolution of 3D Rossby vortices in protoplanetary disks. *Astronomy & Astrophysics* 559, A30 (Nov. 2013), A30.

Rogallo, R.S. *Numerical experiments in homogeneous turbulence*. Technical Memorandum 81315. NASA, 1981.

Salhi, A. and C. Cambon. Stability of rotating stratified shear flow: An analytical study. 81.2, 026302 (Feb. 2010), p. 026302.

Salhi, A., T. Lehner, F. Godeferd, and C. Cambon. Wave-Vortex Mode Coupling in Astrophysical Accretion Disks under Combined Radial and Vertical Stratification. *The Astrophysical Journal* 771, 103 (July 2013), p. 103.

Schartman, E., Hantao Ji, M. J. Burin, and J. Goodman. Stability of quasi-Keplerian shear flow in a laboratory experiment. *Astronomy & Astrophysics* 543 (2012), A94.

Schwartzchild, M. *Structure and Evolution of Stars*. Princeton, NJ: Princeton University Press, 1958.

Shakura, N. I. and R. A. Sunyaev. Black holes in binary systems. Observational appearance. *Astronomy & Astrophysics* 24 (1973), pp. 337–355.

Shalybkov, D. and G. Rüdiger. Non-axisymmetric instability of density-stratified Taylor-Couette flow. *Journal of Physics Conference Series* 14 (Jan. 2005), pp. 128–137.

— Stability of density-stratified viscous Taylor-Couette flows. *Astronomy & Astrophysics* 438 (Aug. 2005), pp. 411–417.

Shen, Y., J. M. Stone, and T. A. Gardiner. Three-dimensional Compressible Hydrodynamic Simulations of Vortices in Disks. *The Astrophysical Journal* 653 (Dec. 2006), pp. 513–524.

Spiegel, Edward A. Convection in stars: I. Basic Boussinesq convection. *Annual review of astronomy and astrophysics* 9 (1971), p. 323.

Stone, J. M. and S. A. Balbus. Angular Momentum Transport in Accretion Disks via Convection. *The Astrophysical Journal* 464 (June 1996), p. 364.

Stone, J. M., T. A. Gardiner, P. Teuben, J. F. Hawley, and J. B. Simon. Athena: A New Code for Astrophysical MHD. *The Astrophysical Journal Supplement Series* 178 (Sept. 2008), pp. 137–177.

Tanga, P., A. Babiano, B. Dubrulle, and A. Provenzale. Forming Planetesimals in Vortices. *Icarus* 121.1 (1996), pp. 158–170.

Tevzadze, A. G., G. D. Chagelishvili, and J.-P. Zahn. Hydrodynamic stability and mode coupling in Keplerian flows: local strato-rotational analysis. *Astronomy & Astrophysics* 478 (Jan. 2008), pp. 9–15.

Tevzadze, A. G., G. D. Chagelishvili, J.-P. Zahn, R. G. Chanishvili, and J. G. Lominadze. On hydrodynamic shear turbulence in stratified Keplerian disks: Transient growth of small-scale 3D vortex mode perturbations. *Astronomy & Astrophysics* 407 (Sept. 2003), pp. 779–786.

Turner, N. J., A. Carballido, and T. Sano. Dust Transport in Protostellar Disks Through Turbulence and Settling. *The Astrophysical Journal* 708 (Jan. 2010), pp. 188–201.

Turner, N. J. and J. F. Drake. Energetic Protons, Radionuclides, and Magnetic Activity in Protostellar Disks. *The Astrophysical Journal* 703 (Oct. 2009), pp. 2152–2159.

van Gils, D. P. M., S. G. Huisman, G.-W. Bruggert, C. Sun, and D. Lohse. Torque Scaling in Turbulent Taylor-Couette Flow with Co- and Counterrotating Cylinders. *Physical Review Letters* 106.2, 024502 (Jan. 2011), p. 024502.

Varnière, P. and M. Tagger. Reviving Dead Zones in accretion disks by Rossby vortices at their boundaries. *Astronomy & Astrophysics* 446.2 (2006), pp. L13–L16.

Velikhov, E. P. *Sov. Phys. JETP* 36 (1959), p. 1398.

Volponi, F. Linear transport in fully stratified discs. *Monthly Notices of the Royal Astronomical Society* 406 (July 2010), pp. 551–557.

Yavneh, I., J. C. McWilliams, and M. Jeroen Molemaker. Non-axisymmetric instability of centrifugally stable stratified Taylor Couette flow. *Journal of Fluid Mechanics* 448 (Dec. 2001), pp. 1–21.